

# POLITECNICO DI TORINO

---

Department of Mechanical and Aerospace Engineering  
Master of Science-level in Biomedical Engineering

## Synthesis and Characterization of Ferrofluid Impregnated Magnetic Scaffolds for Hyperthermia



Supervisors:

Prof. Giuseppe VECCHI

Prof. Giuseppe MAZZARELLA

Dr. Alessandro FANTI

Candidate: Matteo Bruno LODI

---

a.a. 2017/2018 - October 2018

# Table of contents

<b>1</b>	<b>Introduction</b>	<b>1</b>
<b>2</b>	<b>Fundamentals of Electromagnetism</b>	<b>3</b>
2.1	Maxwell's Equations . . . . .	3
2.1.1	Frequency Domain . . . . .	4
2.2	Electromagnetic Properties of Materials . . . . .	5
2.2.1	Dielectric Properties . . . . .	6
2.2.2	Magnetic Properties . . . . .	7
	Diamagnetism . . . . .	8
	Paramagnetism . . . . .	8
	Ferromagnetism . . . . .	9
	Superparamagnetism . . . . .	11
<b>3</b>	<b>Magnetic Biomaterials for Biomedical Applications</b>	<b>20</b>
3.1	State-of-the-Art of Theranostic Magnetic Materials . . . . .	20
3.1.1	Magnetic Nanoparticles: Synthesis, Properties and Applications . . .	20
3.1.2	Magnetic Scaffolds for Tissue Engineering and Regenerative Medicine	22
<b>4</b>	<b>Materials and Methods</b>	<b>28</b>
4.1	Materials . . . . .	28
4.1.1	Magnetic Nanoparticles . . . . .	28
4.1.2	Scaffolds . . . . .	28
4.2	Magnetic Scaffolds Synthesis . . . . .	29
	Qualitative and Quantitative Analysis . . . . .	31
4.3	Design of the AC Susceptibility Measurement System . . . . .	32
4.3.1	State-of-the-Art of Magnetic Susceptibility Measurements . . . .	32
4.3.2	Design of Air-Core Coils . . . . .	38

Inductance Calculations . . . . .	38
Stray Capacitance Estimation . . . . .	41
Coil DC and AC Resistance . . . . .	43
Estimating the Coil Q-factor . . . . .	44
A Genetic Algorithm for the Non-linear Constrained Optimization of Sensing Coil . . . . .	45
FEM Simulation of the Designed Coil . . . . .	47
4.3.3 The Measurement System . . . . .	47
Thermographic Investigation: SAR Evaluation . . . . .	49
4.4 An <i>in Silico</i> Model for Bone Tumor Hyperthermia Treatment with Magnetic Scaffolds . . . . .	51
4.4.1 Problem Statement: Orthopedic Oncology . . . . .	52
4.4.2 Geometry . . . . .	53
4.4.3 The Non-Linear Fully Coupled Electromagneto-Thermal Model . . .	55
4.4.4 Simulations Overview and Parameters . . . . .	57
Dielectric Properties . . . . .	57
Thermal Properties . . . . .	58
<b>5 Results</b>	<b>60</b>
5.1 Characterization of Magnetic Scaffolds . . . . .	60
5.2 Coil Manufacturing: Geometry, Field, RLC Measurements . . . . .	64
5.3 Magnetic Scaffolds AC Susceptibility Spectra . . . . .	67
5.4 Simulations of the Hyperthermia Treatment on Deep Seated Bone Tumors .	68
<b>6 Conclusions</b>	<b>71</b>
<b>Bibliography</b>	<b>78</b>



# Chapter 1

## Introduction

This dissertation work aim to investigate and understand the dynamic magnetic properties of magnetic biomaterials for hyperthermia treatment. In Chapter 2 Electromagnetics principles and equations are briefly reported, explained and discussed for the purpose of investigating and modeling magnetic materials. Moreover, a comprehensive overview of dielectric and magnetic properties of material is provided, with particular attention to the physical understanding of ferromagnetic and superparamagnetic nanoparticles dynamics in the radiofrequency regime. In Chapter 3 are summarized and critically described the synthesis methods, characterization, relevant findings and applications of magnetic nanoparticles and magnetic scaffolds. The core of this dissertation work is Chapter 4. Therein, materials and methods chosen for the scaffold synthesis are reported. Following the manufacturing approach, a coherent discussion of the state-of-the-art of AC susceptometer is faced in order to determine the fundamentals design requirements to be pursued while designing a measurement device for the spectra of magnetic scaffolds. Finally, addressing the problem of the treatment of deep-seated bone tumors using the synthesized magnetic scaffolds, an enhanced non-linear and multiphysic model of magnetic induction hyperthermia is presented. In Chapter 5, the results from the morphological, qualitative and quantitative properties of magnetic scaffolds is given. The experimental findings are discussed and referred to literature surveys, allowing to extract the knowledge to interpret the numerical results from the *in silico* simulations of magnetic hyperthermia treatment of bone tumors.

This dissertation works challenges the accurate description of the manufacturing, morphological and functional characterization of a novel class of therapeutic magnetic biomaterials. To start bridging the gap between the research ambitions and clinical needs, the present text aims to retrieve the most important features for describing accurately the

hyperthermia treatment, while ensuring an experimental and quantitative basis to allow the initial clinical translation of these powerful theranostic biomaterials.

## Chapter 2

# Fundamentals of Electromagnetism

### 2.1 Maxwell's Equations

Every Electromagnetic (EM) phenomenon is described by the Maxwell's equations [1]:

$$\nabla \times \mathbf{H} = \frac{\partial(\epsilon_0 \mathbf{E})}{\partial t} + \mathbf{J} \quad (2.1)$$

$$\nabla \times \mathbf{E} = -\frac{\partial \mathbf{B}}{\partial t} \quad (2.2)$$

$$\nabla \cdot \mathbf{E} = \rho/\epsilon_0 \quad (2.3)$$

$$\nabla \cdot \mathbf{B} = 0 \quad (2.4)$$

where  $\mathbf{H}$  is the magnetic field vector, measured in  $Am^{-1}$ , whilst  $\mathbf{P}$  is the polarization vector (or the so-called electric displacement) and  $\mathbf{J}$  being the conduction current vector, in  $A \cdot m^2$ . The electric field vector is  $\mathbf{E}$ , in  $Vm^{-1}$ , which is related to the temporal variation of the magnetic induction vector or the magnetic flux density vector, *i.e.*  $\mathbf{B}$ , given in T. Spatially, the electric Gauss theorem (Eq. (2.3)) states that the electric field depend on the space charge density enclosed in the system, *i.e.*  $\rho_{ch}$  in  $Cm^{-3}$ .

All the physical quantities described from Eq. (2.1) to (2.4) are fields, hence they are both function of the position  $\mathbf{r}$  and time ( $t$ ) [1]. The two constant  $\epsilon_0$  and  $\mu_0$  are the vacuum

permittivity, i.e.  $8.85 \cdot 10^{-12} \text{ Fm}^{-1}$ , and permeability, i.e.  $4\pi \cdot 10^{-7} \text{ Hm}^{-1}$  [1], [2].

The physical quantity described by the two rotor and divergence equations are obviously subject to the fundamental energy conservation principle, so that, given a domain  $\Omega$ , the sum of the charge variation in time and the current flux passing through the domain boundary,  $\partial\Omega$ , should be equal to zero, *i.e.*:

$$\frac{\partial \rho_{ch}}{\partial t} + \nabla \cdot \mathbf{J} = 0 \quad (2.5)$$

This last Eq. (2.5) is called the continuity equation and is necessary to investigate the electrodynamic of continuous media [1].

### 2.1.1 Frequency Domain

To study and investigate the dynamic of electromagnetic field, assuming a sinusoidal or harmonic definition, the Maxwell's equations can be written as follows [1], [2]:

$$\begin{aligned} \nabla \times \mathbf{H} &= j\omega(\epsilon_0 \mathbf{E} + \mathbf{J}) \\ -\nabla \times \mathbf{E} &= -j\omega \mathbf{B} \end{aligned} \quad (2.6)$$

This very general form can be applied to quasi-static or high-frequency problems. Since Eq.s (2.3) and (2.4) can be derived from the Ampere's and Faraday's laws, and being always constrained to the continuity equation, henceforth the frequency domain equations are addressed as the Maxwell equations.

In the simplified case of free-space propagation, *i.e.* for a homogeneous, lossless, infinite medium, no boundary conditions applies to Eq.s (2.6), an irrotational vector potential  $\mathbf{A}$ , so that [1]:

$$\nabla \cdot (\nabla \times \mathbf{A}) = 0 \quad (2.7)$$

This vector, thanks to the Gauss magnetic law (Eq. (2.4)), allow to write the magnetic flux density as [1]:

$$\mathbf{B} = \nabla \times \mathbf{A} \quad (2.8)$$

The advantage of this formulation is that only a vector field is solved instead of three vector field ( $\mathbf{E}, \mathbf{B}$ ). The vector potential formulation is often employed when computing the numerical solution of Maxwell's equations [2].

In the time-harmonic regime the energy is supposed to be infinite. Moreover, if in free-space or vacuum, no dissipative phenomena occurs and hence, being the power constant, the source should be internal or the power may only enter in the system from the boundaries. The power averaged over one time period of the sinusoid,  $P$ , for time-harmonic vector, is defined as [2]:

$$P = \frac{1}{T_{cycle}} \int_0^{T_{cycle}} p(t) dt = \frac{1}{T_{cycle}} \int_0^{T_{cycle}} v(t) \cdot i(t) dt = \frac{1}{2} \operatorname{Re}\{VI^*\} \quad (2.9)$$

where the phasorial notation is employed. To compute the overall power inside the domain it is necessary to account for the dissipated and stored power, which can be written as, at the location  $\mathbf{r}$ :

$$\begin{aligned} & \frac{1}{2} \operatorname{Re}\{\mathbf{EJ}^*\} \\ & \frac{1}{2} \operatorname{Re}\{\mathbf{E}\epsilon_0\mathbf{E}^*\} \\ & \frac{1}{2} \operatorname{Re}\{\mathbf{H}\mu_0\mathbf{H}^*\} \end{aligned} \quad (2.10)$$

Then, exploiting the well-known relationship for the modulus of a complex vector ( $|W|^2 = \mathbf{W} \cdot \mathbf{W}^*$ ), and taking the sum of the stored electric and magnetic energy, as well as the dissipated energy, after the time-averaging, the Poynting vector is obtained [1], [2]:

$$\mathbf{S} = \frac{1}{2} \mathbf{E} \cdot \mathbf{H}^* \quad (2.11)$$

This fundamental physical quantity accounts for the active and reactive power in any EM systems. Therefore it can be exploited to describe EM propagation in biological media, but also systems as coil or even the behavior of magnetic materials under investigation in this dissertation work [3].

## 2.2 Electromagnetic Properties of Materials

Not every EM phenomena occurs in free-space, therefore, in Eq.s (2.6) the physical properties of the medium in which the EM phenomena is occurring [1] - [3]. Materials presents several various and nuanced type of response to an electromagnetic field [4]. The so-called constitutive relationship are employed to include the material contribute to the electrodynamic problem [1]:

$$\begin{aligned} \mathbf{P} &= \epsilon_0 \epsilon_r \mathbf{E} \\ \mathbf{B} &= \mu_0 \mu_r \mathbf{H} \end{aligned} \quad (2.12)$$

where  $\epsilon_0$  and  $\mu_0$  are the vacuum constants previously defined, whilst  $\epsilon_r$  and  $\mu_r$  are the relative dielectric permittivity and relative magnetic permeability of the medium. These physical quantities can be constants or depend on several parameters, such as the frequency and strength of the applied field, the temperature, the medium composition [4], [5], [6].

In the following further details of the EM properties of are provided, with a deep focus on biological and magnetic materials.

### 2.2.1 Dielectric Properties

Dielectrics are materials in which no free-charges (*e.g.* electrons) are present, this is way they are often considered as insulating materials. Beside conductor materials, which have a null electric field inside them and allows for a noticeable current flux, the dipoles which constitutes dielectric materials, under the action of an external electric field  $\mathbf{E}$ , tend to orient according to the direction of this field to reach an equilibrium condition [7], [8]. These materials can be classified as polar if the medium is composed of molecules with separated charges, *e.g.* water and ethanol mixtures, which are oriented randomly [5]. On the other hand, if in absence of the external electric field no dipoles exists, the dielectric is a polar medium, because, when the  $\mathbf{E}$  field is applied the symmetry between charges is broke and a torque moment establish, determining a non-zero polarization. These considerations hold for static electric field.

When a time-varying electric field of frequency  $f$  is applied to a dielectric medium its dipole interacts with the field tends to orient according to field direction to obtain an internal field opposed to the external forcing agent [7]. Anyway the dipoles inertia prevents these mechanism to be performed without energy expense, *i.e.* with increasing frequency the energy provided by the field is loss by the medium and hence dissipated (this cause the power flux to be imaginary as suggested by Eq. (2.11)). In EM problems the dielectric permittivity becomes a complex number if dissipative phenomena occurs [1]:

$$\epsilon(\omega) = \epsilon_0 \epsilon_r - j \frac{\sigma}{\omega} = \epsilon' - j \epsilon'' \quad (2.13)$$

where  $\epsilon'$  and  $\epsilon''$  are the real and imaginary part of the dielectric permittivity. It can be noticed that the conductivity  $\sigma$  (*i.e.* the free charge contribute) is mainly responsible for

the dielectric losses.

Biological material are very lossy and dispersive dielectric medium. The properties of biological tissues are usually described using the four-order Cole-Cole model with the parameters reported in the well-known work of Gabriel and Gabriel [9], [10]:

$$\epsilon(\omega) = \epsilon_{\infty} + \sum_{n=1}^4 \frac{\epsilon_s - \epsilon_{\infty}}{1 + (j\omega\tau_r)^{1-\alpha}} - j\frac{\sigma}{\epsilon_0\omega} \quad (2.14)$$

where  $\epsilon_s$ ,  $\epsilon_{\infty}$ ,  $\tau_r$ ,  $\alpha$  and  $\sigma$  are the static and optical dielectric permittivity, the characteristic relaxation time, the Cole-Cole shape parameter and the ionic conductivity of the biological medium, respectively. An example of the frequency response of blood, bone and muscle is provided in Fig. 2.1. As regards the temperature variation of the dielectric permittivity can be assumed proportional to the temperature rise, but the slope/rate of proportionality varies from tissue to tissue, as reported by [11].

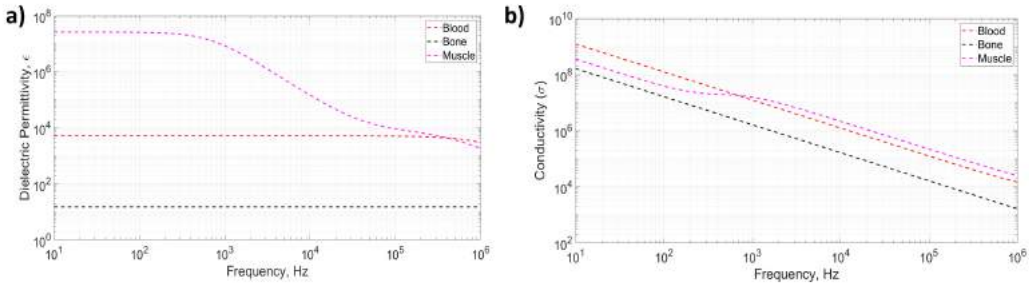


Figure 2.1. Cole-Cole model for blood, bone and muscle tissues from DC to 1 MHz [10]. The real part of dielectric permittivities and tissue conductivities are presented in logarithmic scales.

### 2.2.2 Magnetic Properties

Since the aim of this work is the synthesis and characterization of magnetic biomaterials for biomedical applications, it is necessary to detail and define the various types of magnetic materials that exist in nature. In fact all materials are magnetic [12], but the way they respond to an external magnetic field  $\mathbf{H}$  is very different and may be of interest in this dissertation work. In fact diamagnetic and paramagnetic materials have a negligible magnetic response in almost every engineering and practical applications [2], such as magnetic hyperthermia. However, in the case of magnetic susceptibility measurements, a paramagnetic or diamagnetic material can be employed as reference signal, however, if the magnetic signal source, with respect to the amount in the system under investigation,

is scarce, then the paramagnetism o diamagnetism act as noise and thus jeopardize the measurement. Therefore, in the following clarification about the possible behavior, values of  $\mu_r$  and response of magnetic materials is provided.

### Diamagnetism

Diamagnetic materials present coupled electronic spins, *i.e.* compensated, causing the orbital motion of the electron to determine their magnetic behavior [12], [13]. In other words, since electrons are charged particles, in presence of an applied magnetic field, a moment anti-parallel to the applied field, which indicates that these materials tend to repel the  $\mathbf{H}$  field, *i.e.* they present  $\mu_r < 0$ . The diamagnetic contribute tends to increase with the strength of the applied field [13]. Rather than using magnetic permeability, an analogue quantity is often employed to express the response of a material to a magnetic field, *i.e.* the magnetic susceptibility [12]:

$$\mu_0\mu_r \mathbf{H} = \mu_0(1 + \chi) \mathbf{H} \quad (2.15)$$

Examples of diamagnetic materials are water, which has a magnetic susceptibility equal to  $\chi = -9.1 \cdot 10^{-6}$ , the Bi element has  $\chi = -1.6 \cdot 10^{-6}$ , whilst the graphene present  $\chi = -4 \cdot 10^{-4}$  and the  $SiO_2$  which yield  $\chi = -16.3 \cdot 10^{-6}$ , whereas, finally, the  $Al_2O_3$  which presents  $\chi = -18.1 \cdot 10^{-6}$  [14].

As stated previously, this form of magnetism is often neglected as in the case of EM propagation, RF and MW engineering [2]. However, since the signal strength is strictly related to the amount or density of magnetic dipole in the material, for the purpose of this dissertation work the diamagnetism may act as disturbing agent in the magnetic susceptibility measurements, and therefore it must taken into due account [75].

### Paramagnetism

In the case of paramagnetic materials ( $\mu_r > 0$ ) their atoms, molecules, ions that possess uncompensated electronic spins, exhibit a net magnetic moment, which, in response to an applied magnetic field, can align with it, as depicted in Fig. 2.2.a. In equilibrium conditions, the magnetic dipole moments are randomly aligned (as in the case of dielectric materials), with a orientation and direction strictly dependent on the state of thermal agitation of the system, *i.e.* from temperature, then the probability of excite them with an amount of energy sufficient to allow the system to reach an ordered state can be defined by the Curie expression:

$$\frac{\mathbf{M}}{\mathbf{H}} = \chi = \frac{C}{T} \quad (2.16)$$

where  $\mathbf{M}$  is the magnetization vector ( $A \cdot m^{-1}$ ), *i.e.* the field inside the material, whereas  $C$  is the Curie's constant, specific to the material of interest [12]. The Curie's law establish a relationship between the magnetic susceptibility and temperature, which is linear. In fact, the phenomenon of paramagnetism is "individual": there is no interaction between the spins: by removing the field the spin alignment disappears, causing paramagnetism to be non-permanent and transient in nature [12].

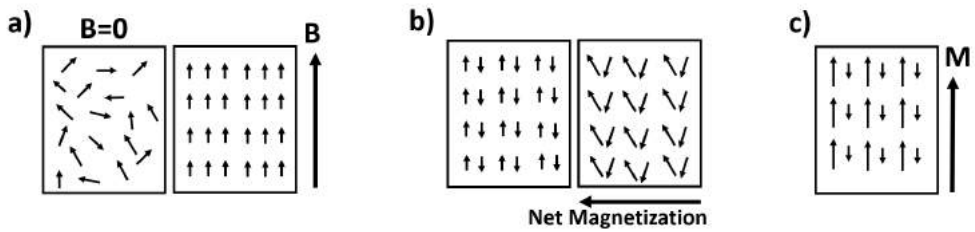


Figure 2.2. Schematic representation of: a) Paramagnetic materials: magnetic dipoles align according to the direction of the external  $\mathbf{B}$  field. b) Anti-ferromagnetic materials. c) Ferrimagnetic materials. Redrafted from [12].

As stated previously for the diamagnets, in absolute values, the paramagnetic materials is definitely not relevant if compared to the following type of magnetic materials. But, as will be discussed henceforth, keeping in mind the goal of measuring the AC susceptibility of magnetic biomaterials, their paramagnetic contribution per unit volume may overcome the magnetic signal, or actually act as an interference [75]. Therefore the planning and design of the susceptometer should be carried out considering this aspect. On the other hand, for the description of the biomedical applications, either the diamagnetism and paramagnetism can be neglected.

### Ferromagnetism

This spread typology of magnetic materials presents, at atomic level, several uncompensated spin (as shown in Fig. 2.2.b and .c), which, in turns, possess a preferred direction. The net dipole moment, in absence of an external applied field, is noticeable and causes a residual field inside the material, *i.e.* the residual magnetization or coercive field [13]. Moreover, when subject to the action of a magnetic field, the uncompensated spin interact non-linearly with each other according to a group phenomenon that allows to observe a

more significant and intense response, hence ( $\mu_r \gg 1$ ). If the external source is turned-off or removed, the material response does not vanish, but, however, part of the external energy is lost in re-organizing the magnetic domain inside the material. This is why ferromagnetic materials present hysteresis [12], [13].

Among ferromagnetic materials, it is possible to distinguish the anti-ferromagnetic subclass [12]. As the name suggests, this category of ferromagnetic materials present atoms with unbalanced spins and arranged in an anti-parallel configuration, as in Fig. 2.2.b. In this case, as previously described, the net magnetic moment inside the materials non-null and it give rise to a strong cooperative phenomena between dipoles under the action of an external field [13]. The description of this atomic configuration of a material is more appropriate in most real cases. In fact even no opposite spins are find in the lattice of a material, for sure imperfections, defects and incongruities in the lattice can be found, *i.e.* locally determine analogous situations [12], [13]. As regard the ferrimagnetic materials, an unequal number of uncompensated electrons see two moments of very different magnitude, as depicted in Fig. 2.2.c, as in the case of  $Fe_3O_4$  molecule, which consists of both  $Fe^{2+}$  and  $Fe^{3+}$  ions in its lattice structure. Similarly to the paramagnetic materials, also in ferrimagnetic systems the temperature plays a fundamental role in the behavior and response of the material to the applied external field [15]. If in the paramagnetic and non-interacting system case a linear dependence on temperature presents, in ferromagnets the probability of the dipole to be excited by the external soruce is more complex and then the magnetization phenomenon is a non-linear function of the system temperature [12], [13], [15], as shown in Fig. 2.3. By increasing the thermal energy the energy exchanged between the spins is not enough to impose a net magnetic moment to oppose to Brownian motion, therefore, a critical temperature at which the material behaves as a paramagnetic one exists and it is the Curie temperature.

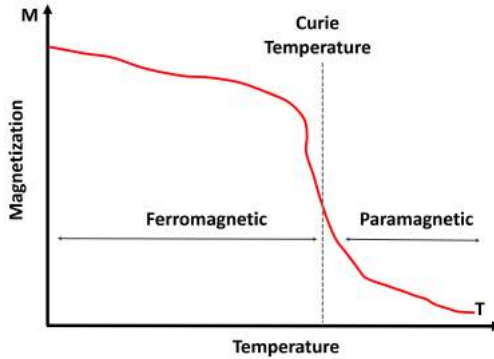


Figure 2.3. Temperature dependence of the magnetization for a generic ferromagnetic material. Redrafted from [12].

### Superparamagnetism

The considerations and discussion reported previously are took into due account the atomic structure of magnetic materials, but referred to the macroscopic and bulk behavior of a volume of such materials [15]. From the second half of the last century is of interest in many science fields the use of magnetic materials with increasingly reduced scales up to nanometer scale, *i.e.* 1-200 nm [16].

At these scale, materials such as  $Fe_3O_4$  present a peculiar molecular disorder, defined as heterogeneous with low energy regions for which, depending on the particle size (as shown in Fig. 2.4), the formation of magnetic domains is energetically unattractive [15], [16]. The magnetic domains and their walls are responsible for the material demagnetizing interactions, which are observable at the macroscopic scale. The domain walls determines a strong residual field for bulk materials, however, since in material with nanometric size the wall formation is prevented, therefore they can be classified as almost zero-coercive field material [16]. Under these conditions groups of spins oriented in the same direction presents, which, moreover, act cooperatively (this is the ferromagnetic side of this very special class of materials), and yet without permanent effects (therefore in a paramagnetic way). This mixture of magnetic behavior is addressed in the literature as superparamagnetism (SPM) [15] - [17].

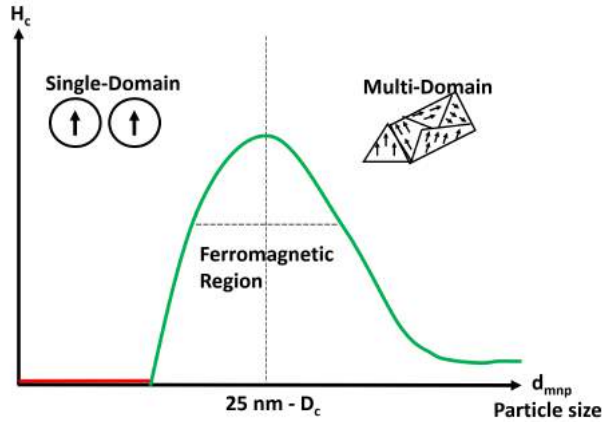


Figure 2.4. Particle size influence on magnetic response of materials. Redrafted from [16].

In these conditions if the system thermal energy or temperature is above a threshold value called the blocking temperature ( $T_b$ ), when an external magnetic field is applied, the spins and the magnetization vector associated with them, perform a flipping motion between the desired energy state, in order to orient with field direction [16]. This phenomena produces a very marked response for objects of this size [16].

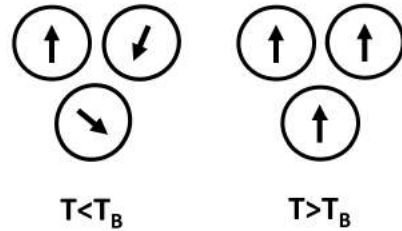


Figure 2.5. Thermal barrier mechanism of superparamagnetic nanoparticles below and above the blocking temperature. Redrafted from [16].

The magnetization vector is free to flip if system temperature is higher than the blocking temperature, which depends in turn on the intrinsic properties of the material, in particular the magnetic anisotropy energy per unit volume  $K_a$ , specific for each particle, which is a measure of the height of energy barrier to be overcome in order to observe the SPM response [15]:

$$T_b = \frac{K_a V_m}{25 k_B} \quad (2.17)$$

where  $V_m$  is the particle volume in  $m^3$ ,  $k_B$  is the Boltzmann constant, *i.e.*  $1.3806 \cdot 10^{-23}$ . Above this temperature the particles are free to align with the external static magnetic field and allow their magnetic moment to rotate, determining the superparamagnetic state in which the particle magnetization is defined as [16]:

$$\mathbf{M}(\mathbf{H}) = M_s \mathbf{L} \left( \frac{\mu_{mnp} \mu_0 \mathbf{H}}{k_B T} \right) = M_s \left( \coth \left( \frac{\mu_{mnp} \mu_0 \mathbf{H}}{k_B T} \right) - \frac{k_B T}{\mu_{mnp} \mu_0 \mathbf{H}} \right) \quad (2.18)$$

where  $M_s$  is the saturation magnetization, measured in  $\text{emu} \cdot g^{-1}$  or  $A \cdot m^{-1}$  and  $\mu_{mnp}$  is the magnetic moment of the nanoparticle (henceforth NP), in  $JT^{-1}$ . Depending on the scale chosen to observe the behavior of a magnetic nanoparticle (MNPs), it is worth noting that a preferred axis (called easy axis) exist, *i.e.* a direction along which the work done by the magnetization vector is minimum and then the magnetization is maximum [15]. As a matter of fact, to account for  $\mu_{mnp}$  the angle between the external field and the easy axis should be considered, however, in practice, this aspects is often neglected, since, for sufficiently high field ( $\mu_0 \mathbf{H} \gg k_B T$ ) all the particles are assumed oriented with the field and the angles tends to be equal to zero [16], [17].

This last discussion should be referred to a single nanoparticle, however, nowadays exists the technological possibility of producing objects, devices and nanocomposite materials which contains a great amount of MNPs, in the following the general problem of describing the overall, global, macroscopic behavior of nanostructured magnetic materials is addressed [15]. The following general classification can be performed according to [15]:

- *Isolated particles:* materials with unique magnetic properties, due to the elimination of the contributions due to the interaction between particles.
- *Core-Shell Morphology:* if oxide layer, polymer or metal coating are present onto NP surface. This configuration is supposed to increase the hysteresis effects and to decrease the overall magnetic response of the material. However, selecting properly the coating material, this type of nanostructured material enhances properties such as biocompatibility and suspension stability [18].
- *Monodisperse Nanostructured Material:* nanoparticles embedded in a matrix with dissimilar chemical properties. The behavior of these materials is determined by the

volume fraction of MNPs and by the characteristics of the matrix, which may or may not be interacting [15], [19].

Therefore, for a monodisperse nanostructured material, the overall magnetization follows the Eq. (2.18) but including the volume fraction of the magnetic phase in the system (*i.e.*  $\phi_m$ ).

These are few example of the possible categories of nanostructured materials. The Rieke metals should be mentioned: they are very reactive metals that reduce the use of metal salt in hydrocarbon solvents. As regards ferrofluids, *i.e.* viscous colloidal systems in which MNPs are dispersed, and magnetic nanocomposite for biomedical application, these particular systems are going to be treated with a deep focus and providing coherent discussion in the following.

For this dissertation work, the comprehension and description of magnetic nanostructured materials behavior is fundamental. In particular, a set of novel magnetic biomaterials are under investigation. Therefore, since the aim is to exploit the knowledge acquired about their composition and functionalities in order to develop relevant and effective hyperthermia applications for oncology purposes, the starting point and the ground-truth must be defined.

Therefore, relying on the valuable work of Rosensweig [20], the issue of the modeling of the magnetic nanoparticles dynamic when exposed to a radio-frequency (RF) electromagnetic field is faced. In fact, is a widely accepted fact that MNPs subject to a time-varying magnetic field are able to dissipate a power high enough to be employed for therapeutic scopes [16]. Assuming a ferrofluid (FF), *i.e.* a homogeneous monodispersion of MNPs in a viscous medium, with volume fraction  $\phi_m$ , if a sinusoidal EM field is applied, the temporal evolution of the magnetization vector obeys the following law [21], [22]:

$$\frac{\partial \mathbf{M}}{\partial t} = \frac{\mathbf{M} - M_{eq}}{\tau} \quad (2.19)$$

where  $M_{eq}$  is the equilibrium magnetization and  $\tau$  is the characteristic time to reach it, or, if preferred, the relaxation time of the MNPs ensemble. However, treating the magnetization problem at this scale and in the time domain is rather tricky, thus the molecular dynamic approach is often followed [22]. Nevertheless, moving into the time-harmonic notation (or Alternate Current representation, *i.e.* AC), writing the applied magnetic field as [20]:

$$\mathbf{H}(t) = H_0 \cos(2\pi f t) = Re\{H_0 e^{j2\pi f t}\} \quad (2.20)$$

being  $H_0$  the peak amplitude and  $f$  the frequency (and, of course,  $\omega$  is the angular

frequency), Eq. (2.19) is easily solved and, with the substitution  $\mu_0(\mathbf{H} + \mathbf{M}) = \mu_0(1 + \chi)\mathbf{H}$  while assuming  $\chi$  as a complex variable which account for dissipative phenomena, the magnetization is [20]:

$$\mathbf{M}(t) = H_0 [\chi' \cos(2\pi ft) + \chi'' \sin(2\pi ft)] \quad (2.21)$$

From this finding, the dissipated power in a cycle can be derived by multiplying the frequency with the infinitesimal work done by the magnetic field on the MNPs, in other words [20]:

$$P_m = f \cdot dU = f \cdot (\mathbf{H} d\mathbf{B}) = 2\pi\mu_0^2 H_0^2 \chi'' \int_0^{2\pi} \sin^2(2\pi ft) dt \quad (2.22)$$

which yields:

$$P_m = \pi\mu_0 f |\mathbf{H}|^2 \chi'' \quad (2.23)$$

The demonstration is straightforward, however, according to the general discussion about lossy material in 2.2.1, assuming that  $\chi = \chi' - j\chi''$  implies that  $\chi = \chi(\omega)$ . Nothing was said about the form of  $\chi(\omega)$ . Anyway, as done for other media such as water, protein dispersion or others [1], the easiest description of a material frequency response is the Debye model [20], as shown in Fig. 2.7. The basic assumption of the cited model are that the system elements, therein MNPs, are poorly interacting and that a resonance exists [12], [23], or in mathematical terms:

$$\chi(\omega) = \frac{\chi_0}{1 + 2\pi f\tau} \quad (2.24)$$

where the equilibrium magnetization of an ensemble of magnetic nanoparticles is defined as [20]:

$$\chi_0 = \frac{\mu_0 \phi_m V_m M_s^2}{k_B T} \quad (2.25)$$

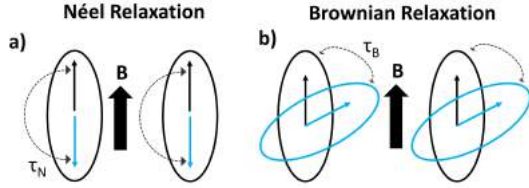


Figure 2.6. Figure representing the two relaxation mechanisms typical of a ferrofluid.

The characteristic time in Debye model Eq. (2.24) can depend on several factors, namely particle intrinsic properties (*e.g.* crystallinity ( $K_a$ ), particle size ( $V_m$ )) and extrinsic factors, *i.e.* system temperature and physical conditions. In particular, in the case of a ferrofluid, two mechanism took part to define the effective relaxation time. The most relevant and always present phenomenon, is the Néel process [16], depicted in Fig. 2.6. The Néel relaxation time  $\tau_N$  is the time interval required for the magnetic dipole moment to return to the equilibrium after being perturbed by an external energy source, as already explained previously in this Section. The expression for this characteristic time is [15] [20]:

$$\tau_N = \tau_0 e \frac{K_a V_m}{k_B T} \quad (2.26)$$

where  $\tau_0$  is a pre-exponential factor, supposed to vary from 1 ns to 0.1 ps. However, to be precise and include the full-dependence on system temperature, it can be defined as [24]:

$$\tau_0 = \frac{\sqrt{\pi}}{4} \frac{M_s(0)}{K_a \gamma_e} \left[ \frac{1}{\xi_f} + \xi_f \left( \frac{M_s(T)}{M_s(0)} \right)^2 \sqrt{\frac{k_B T}{K_a V_m}} \left( 1 + \frac{k_B T}{K_a V_m} \right) \right] \quad (2.27)$$

where  $M_s(0)$  is the magnetization extrapolated at 0 K from the Zero Field Cooled (ZFC) and Field Cooled (FC) curves, whilst  $M_s(T)$  is the magnetization at the desired temperature. The term  $\gamma_e$  is the electron gyromagnetic ratio, given in conventional units. Finally, the dimensional constant  $\xi_f$  can be written as [24]:

$$\xi_f = \xi \gamma_e M_s(0) \quad (2.28)$$

where  $\xi$  is the dimensionless damping constant equal to 0.45.

Despite the Néel mechanism, which is related to the magnetic dipole of the NP, when dispersed in a solution this nanostructured elements are subject to Brownian motion, shown in Fig. 2.6, in particular to rotational motion, which determines a secondary and slower dissipative mechanism [16], [20]. Therefore, the effective relaxation time can be evaluated

as the parallel of the Néel and Brownian mechanisms, which means that the resulting time is the harmonic sum of them [20]:

$$\frac{1}{\tau} = \frac{1}{\tau_N} + \frac{1}{\tau_B} \quad (2.29)$$

where the Brown relaxation time is given by the following equation [20]:

$$\tau_B = \frac{3\eta V_h}{k_B T} \quad (2.30)$$

being  $\eta$  the solution viscosity in  $Pa \cdot s$  and  $V_h$  the hydrodynamic radius of the particles in solution, which can be evaluated by Dynamic Light Scattering or Z-potential measurements [24]. An example of the frequency response for a 4 nm ferrite nanoparticles, with  $\tau_N$  and  $\tau_B$  is provided in Fig. 2.7.

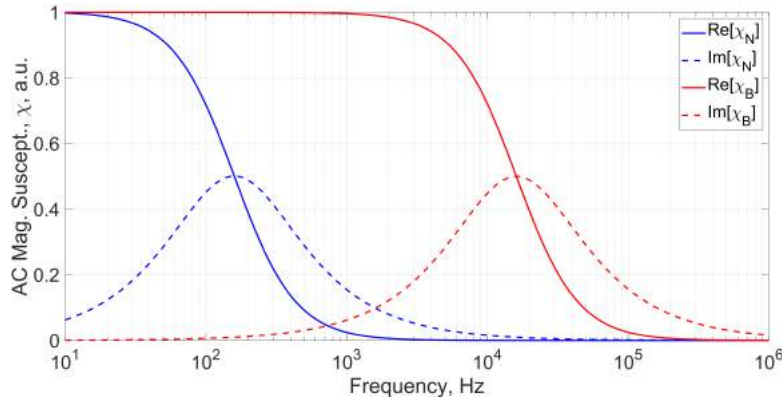


Figure 2.7. Example of the Debye frequency response for a water-based ferrofluid of 4 nm ferrite nanoparticles, with  $\tau_N = 1$  ms and  $\tau_B = 10$   $\mu$ s. The different relaxation time influence the resonant frequency.

The described model has been applied to MNPs systems in aqueous or organic solutions and the description of the heat loss agrees very well with the experimental findings [20]. However, the assumption of "parallel" occurrence of the two aforementioned phenomena does not rely on a theoretical basis, thus making the Eq. (2.29) to be founded on empirical basis [22]. Anyway, as will be discussed in the following, novel materials which embed magnetic nanoparticles are currently and increasingly developed to satisfy several biomedical and therapeutic needs, but just a few of these innovative devices possess magnetic properties which can be described by the well-established Debye model [19], [25], [26].

Recently, van Berkum *et al.* [27] synthesized a poly(acrylic-acid) (PAA) hydrogel in which magnetite and cobalt ferrite nanoparticles where embedded, fixed in the polymeric network.

This material was supposed to be used as a functional element in magneto-resistive sensors, anyway, since the MNPs were blocked and frozen in the cross-linkers of this ferrogel, the final result was a material with a non significant AC magnetic response, with respect to the particles free in solution [27]. A complete flat response of the ferrogel was observed from 100 Hz to 1 MHz, whilst the ferrofluid presented the marked resonance of  $\chi(\omega)$  [27]. This finding indicates that the manufacturing strategy of magnetic biomaterials is intrinsically related to their functional properties, in particular to the AC response. Related to chemical composition and the molecular configuration of the material, the dipolar interaction of the MNPs in the system must be considered and somehow quantified to estimate if the basic assumption from the Debye model might be valid or not [19], [23], [26], [27]. At a first glance, a measure of the level of interaction between particles is given by the following dimensionless number [27]:

$$\Upsilon = \frac{\mu_0 \mu_{mnp}^2}{4\pi k_B T d_{mnp}^3} \quad (2.31)$$

As can be inferred, the dimensionless number  $\Upsilon$  is the ratio between the dipole energy per unit volume and the thermal energy per unit volume. In fact, the cubic power of the particle diameter,  $d_{mnp}^3$ , is the lower limit of the volume packaging and steric hindrance in the system. Therefore, comparing the case of ferrofluid to the nanocomposite one, for the same type of MNPs and at a given fixed temperature, it can be easily found that  $\Upsilon_{solution} < \Upsilon_{solid}$ , since the hydrodynamic diameter of the particle in solution should be used. This simple and naive reasoning complies with the physic evidences shown in [20] and [27].

In the work of van Berkum *et al.* [27] the possibility of clusters formation is not taken into account. However, if magnetic nanocomposite or Fe-chemical-doped biomaterials are manufactured, the cluster formation may not be controlled and this event may not be avoided. As described by the model of Landi and fellow [26], in system composed of MNPs the long-range and dipolar interactions become relevant. Moreover, if clusters of nanoparticles forms, the packaging strongly modifies their anisotropy energy, implying that a distribution of  $K_a$  appear. Studying the AC magnetic susceptibility, or, to be precise, the temperature variation of the imaginary part, exploiting a mean-field approximation, they demonstrated that the strong particle-particle interactions influence the anisotropy energy distribution and affects the evaluation of  $\tau_0$  and then  $\tau_N$ , meaning that also the magnetic power dissipated in these systems can be considerably underestimated [26]. As a matter of fact, if the heat loss from a MNPs ensemble is intended to be transferred to a patient to

be used as therapeutic heat in hyperthermia treatment, then the treatment planning and the subject are in danger since the main operational parameter is a source of uncertainty. The mean-field model for the frequency response of magnetic susceptibility is quite complicated to be easily exploited for practical purposes [26]. This is why, in literature other solutions were studied [19]. Hergt *et al.* observed that for  $\chi(\omega)$  of MNPs dispersed in a medium with high viscosity the Debye response disappeared. According to Fanti *et al.* this modification of the  $Fe_3O_4$  nanoparticles response was due to the fact that  $\tau_B$  increases (see Eq. (2.30)) and then the effective relaxation time is the Néel one [19]. This situation is exactly the solid environment in which magnetic nanoparticles are embedded and can strongly interact [26], [27]. Fitting the data from Hergt *et al.*, they derived a Cole-Cole model to describe the AC magnetic susceptibility of the MNPs [19]:

$$\chi(\omega) = \frac{\chi_0}{1 + (2\pi f\tau)^{1-\alpha}} \quad (2.32)$$

where  $\alpha$  is the Cole-Cole shape parameter, which was found to be equal to 0.75. However, even if the authors did not stress it, from Eq. (2.32), the Néel relaxation time is modified by raising it of a quantity  $1 - \alpha$ , which can be considered equal to evaluate an effective characteristic time for the system. In other words, the Cole-Cole model from [19] can be regarded as a simplified and more approximate description of the frequency-dependence of strongly-interacting magnetic materials.

In the following are provided several examples of this last ferromagnetic and superparamagnetic nanostructured, highly packed and strongly interacting materials for biomedical applications.

## Chapter 3

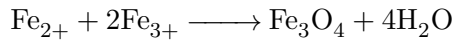
# Magnetic Biomaterials for Biomedical Applications

This chapter contains a comprehensive summary of the state-of-the-art of magnetic biomaterials employed for tissue engineering, regenerative medicine and for therapeutic purposes. An overview of manufacturing methods and synthesis procedure for magnetic nanoparticles is provided. Then the rationale and the genesis of the idea of magnetic scaffolds is analyzed, providing examples of production strategies as well as experimental findings. From the available technologies for the production of magnetic scaffolds, the easiest, more reliable and effective solution is critically selected to be used in this dissertation work.

### 3.1 State-of-the-Art of Theranostic Magnetic Materials

#### 3.1.1 Magnetic Nanoparticles: Synthesis, Properties and Applications

Magnetic nanoparticles are of relevant importance for biosensing devices, medical applications, namely magnetic drug delivery (MDD), immunoassays, contrast agent for magnetic resonance imaging (MRI), bone biophysical stimulation and magnetic induction hyperthermia [6], [24]. Ferromagnetic NPs and SPIONs for biomedical applications should have an adequate dimension and dispersity, demonstrate high magnetization values  $M_s$ , and be biocompatible and not induce cytotoxicity [16], [24]. As reviewed by Laurent *et al.*, magnetic nanoparticles can be synthesized by coprecipitation, *i.e.* by aging of ferrous or ferritic salts in aqueous solution according to stoichiometric ratios (2:1) at pH in the range 8 ÷ 14 [24]:



However magnetite is not stable and is subject to oxidation, this is why, as a byproduct maghemite,  $\gamma - \text{Fe}_2\text{O}_3$ , is obtained too. The co-precipitation technique allow to produce a large amount of MNPs, but the kinetic factors of the process does not permit to control the size distribution. A very important factor is the pH and the ionic strength of the reaction medium, but also temperature play a major role in determining the diameter of the particle: the larger the temperature, the smaller the MNP [24].

In order to produce particles with a narrow distribution of molecular size several method were investigated. The use of dendrimers, surfactant agents, micelles and water-in-oil (WO) emulsions are very popular [24]. In fact, The use of surfactant agents such as sodium dodecylsulfate (SDS), allows the formation of spontaneous nano-assemblies in form of drops, which acts as nano-bioreactors for the iron salts in the solution, preventing the assembly of the colloidal solution and confining the magnetite crystal growth. On the other hand, the WO techniques permits to control the final size of the nano-carrier by monitoring the size of the water droplet and temperature. More details about the water-in-oil emulsions can be found in [28].

A note: Recently the encapsulation of SPIONs in liposomes or solid lipid nanoparticles (SLNPs) are increasingly used for developing smart targeted Drug Delivery (DD) strategies [29].

In lieu of using the previous methods, high temperature reactions such as hydrothermal synthesis can be exploited for  $\text{Fe}_3\text{O}_4$  NPs production [24]. Typically, hydrolysis and oxidation of mixed hydroxides metals occurs in aqueous media in autoclave (200 °C, 2000 psi), however, recently, microwave (MW) are exploited to enhance and fasten reaction time for the hydrothermal route since the hot spots locally obtained by the EM heating would accelerate the synthesis [30].

Finally, a very in vogue and quite easy manufacturing technique is the sol-gel route, *i.e.* the condensation and hydroxylation of precursors in solution, which forms a sol system, which, in turn, if condensed again, produces a 3D network of metal oxide [24]. On the other hand polyols methods, flow injection synthesis, sonolysis, electrochemical methods and aerosol/vapor techniques can be employed, but the process variables to be controlled augment and they require costly instrumentation [24].

To produce a ferrofluid which does not aggregate in biological medium or when an external magnetic field is applied, the  $\text{Fe}_3\text{O}_4$  nanoparticles require a coating material able

to equilibrate electrostatic and steric force, balancing the van der Waals and the dipolar interactions [24], [29]. The most used stabilizing agents are monomers such as carboxylates and phosphates functional groups, which ensure high biocompatibility. Morevoer inorganic materials as silica and gold can be used, with the advantage that further vectorization and bioconjugation is simplified by the silane and thiol chemistry [24]. However, the employment of polymeric stabilizers is the most used strategy. In particular, bio-polymers such as the polysaccharide dextran, the stealth coating of PolyEthylene Glycole (PEG), or the biodegradable chitosan, but also Poly(Acrilic Acid) (PAA), Poly(Latcic Acid) (PLA) and Poly( $\epsilon$ -Caprolactone) (PCL) [24].

Among the most promising applications of the MNPs in biomedicine it is worth noting their use as MRI imaging agents; cellular labeling or imaging (*e.g.* C-MALISA tests, inflammation and apoptosis monitoring); *in vitro* magnetic bioseparation of taget molecules; magnetic controlled drug delivery, hyperthermia (HT) or tumor ablation [24]. As derived from the work of Hildebrandt *et al.*, the HT treatment is supposed to selectively rise tumor temperature above 42.5 °C for a time sufficient to impair transmembranal transport, cause cytotoxicity and then determine the cancer cells death, thus exciting the immune system response [31]. This treatment is a very promising tool for medicine and magnetic nanoparticles play a pivotal role in enhancing its effectiveness and its clinical translation [31], [32]. In brief, the MNPs are injected nearby the tumor site, then they direct to the tumor passively (if the radius is below 200 nm, the pathological structure of tumor capillaries allow easy extravasation) or actively, *i.e.* guided by an external magnetic field. At the pathologic tissue site, their AC response to RF magnetic field is the heat dissipation, which can be exploit as therapeutic heat to rise tumor cells temperature above the lethal threshold [31] - [33]. This application is of interest in this work, but different possibilities of providing the therapeutic heat to deep seated tumor are under investigation.

This is why in the following, a different, novel and oriented to tissue-engineering exploitation of the magnetite nanoparticles is addressed.

### 3.1.2 Magnetic Scaffolds for Tissue Engineering and Regenerative Medicine

Tissue engineering, or TE, has been defined as a multidisciplinary field which "integrates the principles of engineering and life sciences to develop biological substitutes to repair, maintain or improve the function of a tissue" [34]. More generally, TE can be seen as the application of engineering principles, methods and strategies in combination with life sciences towards a fundamental understanding of the function-structure relationship in healthy and pathological tissues, with the purpose of developing an optimal biological

substitute [34], [35].

Although TE is a relatively young scientific field, with a strict discipline and science, *i.e.* it has a set of concepts and structured paradigms that can be used in a systematic way, even if in continuous evolution; this bioengineering sector has existed for some time, but only today, thanks to the possibility of producing more and more technological and specific materials, it is possible to work on the nervous tissue: nerves, tissue brain; on the skin; on specific organs such as the pancreas, the liver, the intestine; but also on the bone tissue [34] - [36].

The basic principles of tissue engineering reflect the fundamental biological phenomena: cell growth and differentiation, cell adhesion, cell migration, aggregation and tissue formation [34]. In fact, working in this field means that the extension of the possibilities of contemporary medical and surgical therapies is to be pursued, as well as stimulate the cells growth and increase the proliferation rate in order to repopulate the tissue of a given organ without replacing it [34]. TE must guarantee methods and instruments capable of controlling the physiological processes involved in these phenomena: the basic strategy consists in trying to restore the continuity of a damaged tissue (which is the most recurring problem), by placing a synthetic object that acts as a structural and host support for the cells of the tissue of interest, this object is called scaffold [37]. Depending on the function and tissue site, the scaffold must be designed and constructed to tune with the physical-chemical characteristics ideal for repair and regeneration, thus creating the essential environment for the cells to differentiate, migrate, multiply and aggregate [34] - [37].

Rather than being a passive supporting structure, the scaffold design science has turned it into a functional device, an *in vivo* tool which can control and simulate directly the tissue thus eliciting the desired biological response [37]. Among the possible strategies for functionalization, the idea, from Bock *et al.*, of including magnetic nanoparticles inside scaffolds results in producing a theranostic and multi-functional implant [38]. Relying on the problems and concepts just discussed, these needinesses of biomedicine led to the realization of a therapeutic scaffold: a bioactive implant capable to be manipulated *in vivo* through magnetic forces, *i.e.* to create a multi-functional magnetic prosthetic implant exploiting MNPs which can [38]:

- control tissue regeneration process (*e.g.* osteogenesis and angiogenesis) serving as a fixed station (or internal magnet) to which magnetic carrier of Growth Factors (GFs) can be directed by means of an external static magnetic field [19]. Magnetic scaffolds can overcome the limitations of magnetic controlled drug delivery [39].

- stimulate the tissues acting as mechano-transducer, eliciting proliferation and differentiation, especially in bone tissue [38], [40].
- generate therapeutic heat and conduct it to surrounding tumor cells, rising their temperature above the lethal threshold value and then allowing the re-growth of healthy tissue at the injured site [19], [41].

In the following the main techniques and results of the magnetic scaffolds found in literature are provided and analyzed. Particular care is given to the prosthetic implants developed for hyperthermia applications.

Bock *et al.* employed 200 nm MNPs to functionalize hydroxyapatite (HA) and collagen scaffolds by letting the biomaterial matrix impregnating in 1 ml solution for 15 min, causing the magnetic phase to physisorb in the materials pore and defects, decreasing the overall porosity [38]. The process was reproduced by Riminucci *et al.*, observing that the magnetization of the sample decreases from the surface to the center, meaning that high concentration of ferrite can be loaded in the surface and subsurface of the scaffolds [42]. This technique is very simple in principle and exploits also commercial on-the-shelf scaffolds and nanoparticles, implying that it can be used to produce magnetic scaffolds easily and fast [38], [42], [43]. The dip-coated or ferrofluid impregnated scaffolds can reach magnetization value ranging from  $0.5 \text{ emu} \cdot g^{-1}$  to  $15 \div 20 \text{ emu} \cdot g^{-1}$ . Moreover, *in vitro*, these type of scaffolds demonstrated poor release of iron ions and were capable of stimulating the activity of ALP expression of mesenchymal stem cells without an external magnetic field applied [38].

Still employing sintered HA as matrix, solutions of  $\gamma - Fe_2O_3$  MNPs were used to impregnate the scaffolds and obtain a functional implant (with magnetization of maximum  $0.094 \text{ emu} \cdot g^{-1}$ ). Under the action of an external magnetic field, it was demonstrated, using an animal model, an increase of cell adhesion, proliferation, and differentiation (affecting ALP and BGP molecular paths) in a way dependent on the amount of magnetic phase [44]. It should be reported that these scaffolds release a  $Fe_3O_4$  amount retained dangerous for the body [44].

Exploring different technique to obtain a magnetic nanocomposite, a nanofibrous magnetic scaffold composed of SPM  $\gamma - Fe_2O_3$  MNPs, together with hydroxyapatite nanoparticles and PLA was manufactured using the electrospinning technique [45]. This nanofibrous scaffold exhibit a  $0.049 \text{ emu} \cdot g^{-1}$  saturation magnetization; and when implanted in a vertebral defect of a rabbit an increases in osteocalcin levels and in osteoblastic differentiation were observed [45].

As reported in Tab. 3.1, the impregnation process is widely spread and diffuse in the literature [38] - [46]. Of course, different types of magnetic nanoparticles, with diverse coatings, can be employed and, therefore, a wide range of possible magnetization can be obtained. Generally, if the scaffold is intended to be employed for magnetic DD applications, then its saturation magnetization should be the highest possible in order to exert a magnetic force of significant magnitude on MNPs to attract [19], [47]. On the other hand, if the scaffold is intended to generate therapeutic heat under the action of a RF magnetic field, therefore, the magnetization should be kept moderately low, or the synthesis process would permit to tune easily this important parameter: the power from Eq. (2.23) relates to  $\chi_0$  via the imaginary part of the Cole-Cole law, *i.e.* Eq. (2.32).

The employment of electrospinning or mixture techniques is due to the use of polymeric scaffolds or the scaffold synthesis from aqueous phase [44] - [48].

A valuable type of bioactive ceramic scaffolds is the intrinsic magnetic hydroxyapatite of Tampieri *et al.* who substituted in the HA lattice  $Fe^{2+}$  and  $Fe^{3+}$  ions in the positions of the calcium, thus allowing the growth of magnetite crystals directly *in situ*, finally producing a highly biocompatible superparamagnetic ceramic material [49]. This strategy was translated to material similar to HA, such as hardystonite, but leading to a ferrimagnetic scaffold [50].

About the possible applications of magnetic scaffolds, the boosting of the cellular response was already addressed. However, if static magnetic fields are applied to implanted functional scaffolds containing MNPs, the fixation and long-term stability of the prosthetic device is increased [40]. Moreover, it has been observed that the architecture of the new-formed bone reflect the magnetic flux density lines and that the integrin pathways, meaning that cells spreading and adhesion is enhanced, thus favoring the differentiation and bone maturation [51].

Table 3.1. Magnetic scaffolds divided by composition, production and MNPs embedded

Type of Scaffold	Synthesis technique	$M_s, emu \cdot g^{-1}$	Type of MNPs	$r_{mnp}$	Coating	Ref.
<i>Composite</i>						
HA/Collagen	Impregnation	0.34 - 15	$Fe_3O_4$	200	Phosphate-starch	[38]
HA/Collagen	Impregnation	0.50	$\gamma - Fe_2O_3, Fe_3O_4$	10-50	n.s.	[43]
HA/PLA	Electrospinning	0.049	$\gamma - Fe_2O_3$	5	M2-3DCS acid	[44]
$\beta$ -TCP	Impregnation	0.62 - 1.15	$Fe_3O_4$	250	Graphen Oxide	[53]
Chitosan/PVA membrane	Electrospinning	0.67 - 3.2	$Fe_3O_4$	280	Sodiumcitrate	[54]
Calcium Silicate/Chitosan	Mixture	6.10 - 10.36	$SrFe_{12}O_{19}$	500 nm	n.s.	[55]
PMMA	Mixture	n.s.	$Fe_3O_4$	10 nm	Anionic surfactant	[48]
Silicate	Mixture	n.s.	$Fe_2O_3$	n.s.	n.s.	[56]
<i>Bioactive ceramics</i>						
Fe-doped HA	Chemical substitution	4	$HA/Fe_3O_4$	10-14	Hydroxyapatite	[49]
HA	Impregnation	12-20	$Fe_3O_4$	200	Phosphate-starch	[42]
HA	Impregnation	0.94-2.5	$\gamma - Fe_2O_3$	8	Oleic acid	[45]
HA	Impregnation	n.s.	$\gamma - Fe_2O_3$	5	Carboxydextran	[57]
<i>Biological polymers</i>						
Chitosan	In situ precipitation	4	$\gamma - Fe_2O_3, Fe_3O_4$	n.s.	n.s.	[58]
<i>Synthetic polymers</i>						
$\epsilon$ -PCL	3D Bioplotting	0.18-0.3	$Fe_3O_4$	25-30	HA	[59]
PLGA	Electrospinning	2.3-10	$Fe_3O_4$	8.47	Oleic Acid	[46]

Also the application of quasi-static or extremely low frequency magnetic fields has been demonstrated to alter human mesenchymal stem cells behavior, altering in a positive way their response and allowing magnetic scaffolds to be used for tissue engineering applications related to bone tissue [52].

As regards the idea of using magnetic scaffolds to perform *in situ* hyperthermia treatment against deep-seated tumors, it must be addressed the attempt to use an antenna array operating at MW by Fan *et al.* [60] in order to treat 34 patients with OS and FS. The temperature was monitored to keep it above 45 °C. This very rough method was not effective, since an 8% recurrence rate, infections and six deaths were reported [60]. Moreover, and this is the point, this outcome stressed the orthopedic clinical need for an adequate management of the pathological fractures after surgery, such as grafts or the use of bone scaffolds to withstand tissue regeneration [60], [61]. This is one of the main reason which lead to the development novel magnetic biomaterials to be used both as scaffolds for tissue support after curettage, and as heat source for local magnetic induction HT treatment of bone tumor [38], [49], [61] - [62]. The principle is valid for different type of tumor tissues, requiring only different biomaterials.

This is why a ferromagnetic inter-medullary pin was proposed [63]. However, bulky and ferromagnetic implants are overlooked and different strategies were developed [41]. Even if recently a PCL scaffolds containing an aluminium disk was proposed for performing hyperthermia of infiltrating tumor cells which would eventually seed while migrating towards other tissues [64]. To perform an effective treatment, as noticed by Stauffer *et al.* in several works [65], [66], the frequency of the applied field should be around 1 MHz, which causes the power dissipated by the implant to be very similar to the dielectric losses of the tissues. However, the condition needed to generate a controlled heat by the implant with a minor risk for the surrounding healthy tissues is [65]:

$$P_m \gg P_e \quad (3.1)$$

Using magnetic scaffolds, as can be noticed by observing Tab. 3.2, the applied frequencies are comprises between tenth of kHz (*i.e.* maximum 750 kHz). This is why several different type of magnetic scaffolds for hyperthermia have been proposed [67]. In particular, composite materials such as bone cements were investigated [48]. In fact, the cement are often employed after osteotomies or bone tumors curettage, then obtaining a magnetic cement, heat can be generated to rise tissue temperature and kill residual cancer cells [48], [56]. Also bioglasses were modified to include ferrous and ferric salts in the classic Hench's 45S5 composition [68]. Even the combination of bone cements and magnetic bioglasses [69].

As reported recently, providing mild hyperthermia and moderate heat stimuli after surgery can enhance *in vivo* the bone growth in rat and rabbit tibial defect model [57].

Table 3.2. Magnetic scaffolds manufactured for hyperthermia treatment.

	<i>MHA</i>	<i>FeHa-PCL</i>	<i>β-TCP</i>	<i>β-TCP/Fe<sub>3</sub>O<sub>4</sub>/GO</i>	<i>Fe-Hardystonite</i>
<i>r<sub>mnp</sub> (nm)</i>	10-14	25-30	<b>n.s.</b>	250	20
<i>Magnetic phase (vol %)</i>	1.6	9.18	n.s.	1	n.s.
<i>Saturation magnetization (emu · g<sup>-1</sup>)</i>	4	0.18-0.3	0.15	0.062-1.15	0.08-1.2
<i>Peak temperature (°C)</i>	40	12	46	65	28
<i>Time (min)</i>	1	5	20	20	6
<i>Applied magnetic flux density (mT)</i>	30	30	17	18	1
<i>Working frequency</i>	293	293	335	409	750
<i>Reference</i>	[49], [41]	[59], [41]	[62]	[53]	[50]

## Chapter 4

# Materials and Methods

In the following details about materials employed in scaffolds synthesis are provided. Moreover, is provided an accurate description of the methodology followed for the design of the sensing coils and the proposed AC susceptometer.

### 4.1 Materials

#### 4.1.1 Magnetic Nanoparticles

The magnetic nanoparticles employed for the synthesis of magnetic scaffolds were purchased from Chemicell (Chemicell GmbH, Berlin, Ge). The fluidMAG-DP are an aqueous dispersion of magnetite nanoparticles surface-coated by a phosphate-starch layer. The fact that these MNPs are processed from the aqueous phase constitutes a noticeable contribute to the final biocompatibility of the device, in fact organic solvents should be avoided for such application [34]. The 16 samples were provided in a  $25 \text{ mg} \cdot \text{ml}^{-1}$ . Two molecular size were selected: 200 nm and 50 nm. The different characteristic dimension determines a different magnetization: the former MNPs type are ferromagnetic in nature (and hence posses a relevant remanent magnetization), whilst the latter are multi-domain superparamagnetic MNPs. By using these two type of MNPs we expect to obtain magnetic scaffolds with a very different magnetization behavior and then investigate the heat generation for therapeutic purposes.

#### 4.1.2 Scaffolds

As discussed previously in Sect. 3, among the various type of biomaterials which can be functionalized or magnetized employing MNPs, bio-ceramics and polymer constitutes a

very appealing choice [41]. In fact, considering the possible *in vivo* use of such innovative materials, ceramics surely constitutes the best matrix to be used in bone tissue engineering applications as well as in orthopedic oncology [70]. On the other hand, polymeric biomaterials are a more general-purpose scaffolds since they are often employed in both soft and hard-tissues [35], [71]. To investigate In this study the ceramic and polymeric scaffolds produced by 3D Bioteck (3D Bioteck LLC, NJ, USA) were purchased from Sigma-Aldrich (Merck KGaA, Darmstadt, Ge). From the analysis of the state of the art, see Tables 3.1 and 3.2, selected scaffolds ceramic material was  $\beta$ -TCP. Said that, 24 bioresorbable, non-cytotoxic, pre-sterilized by  $\gamma$ -irradiation and ready to Use  $\beta$ -TCP disks were acquired. The disks have a 5 mm diameter and are 1.5 mm in height. As polymeric reference material for the other cluster of scaffolds,  $\epsilon$ -PCL was selected because this material is widely employed in many different body sites and tissue [72], also being already investigated for hyperthermia applications but with a different set of MNPs and under diverse synthesis conditions [41]. A set of twenty-four 3D-Insert (with a diameter of 5 mm and 1.6 mm in height), constituted by fiber with a diameter of 300  $\mu$ m, spaced by 300  $\mu$ m, were acquired. These very porous and interconnected structure is supposed to facilitate cells penetration and hosting, but also ensuring a noticeable entrapping of the magnetic nanoparticles during the impregnation process. The MNPs loaded in the biomaterial matrix are supposed to be locally confined in pores and defects, which means that clusters or highly-interacting region exists. Therefore, their magnetic susceptibility is supposed to obey the Cole-Cole law and magnetization dynamic described in [19], [26].

## 4.2 Magnetic Scaffolds Synthesis

In the literature it is possible to find several different methods which describe how to synthesize a magnetic scaffold [41] and most of them are reviewed in Sect. 3.1. Since the aim of this dissertation work is to understand the magnetization dynamic and heat dissipation of nanoparticles embedded in solid matrix, the simple, cost-efficient method of dip-coating or ferrofluid impregnation was chosen [38], [42]. In brief, as described in Fig. 4.1, a magnetic nanocomposite can be obtained by soaking the desired ceramic or polymeric scaffold into a FF with the proper MNPs dilution (step (i) and (ii)). Then, after a 24 h freeze-drying step (iii) and the subsequent thaw to room temperature (iv), an ultrasound sonication bath (180 W, 30 min) has to be performed to remove the nanoparticles which did not stick to the biomaterial surface (v). The magnetic scaffold can be used only after repeating freeze-drying and thawing steps (vi - viii). The process can be repeated from five

#### 4.2. MAGNETIC SCAFFOLDS SYNTHESIS

---

to ten times to obtain higher magnetization of the sample [38], [42]. To be more specific, a scaffold magnetization from a minimum of 0.4 to a maximum of  $20 \text{ emu} \cdot \text{g}^{-1}$  can be obtained, depending on the concentration of MNPs entrapped in the biomaterial matrix.

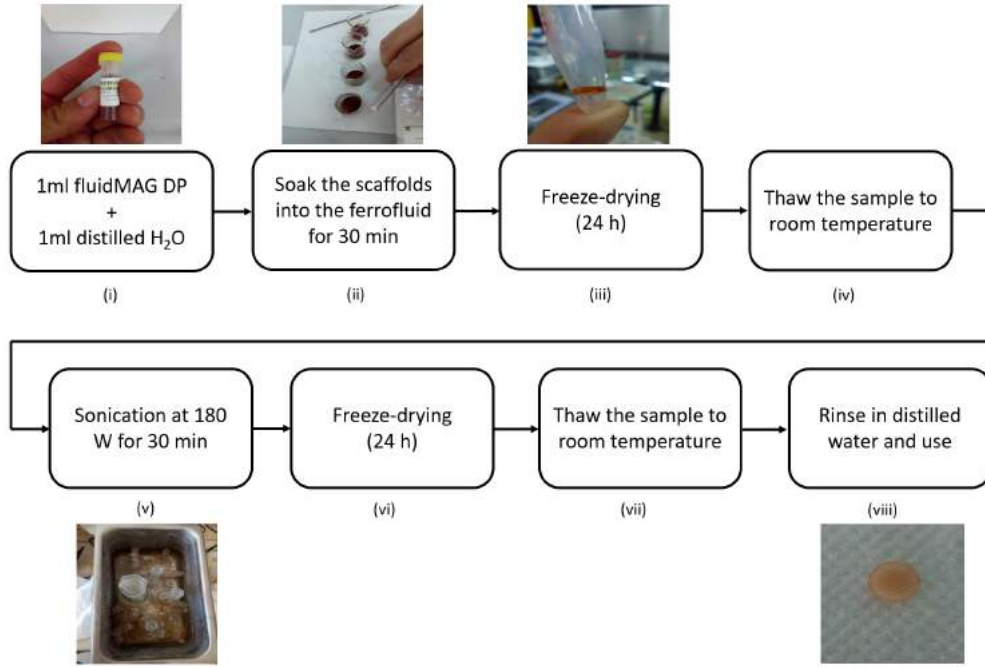


Figure 4.1. Dip-coated magnetic scaffolds: (i) Dilute the ferrofluid up to the desired concentration. In our case  $12.5 \text{ mg} \cdot \text{ml}^{-1}$  is used. (ii) Soak the ceramic or polymeric scaffold into the ferrofluid and let capillarity act for 30 min. (iii) Extract the impregnated scaffold and freeze-drying the sample at  $^{\circ}\text{C}$  for 24 h. (iv) Thaw the sample up to room temperature. (v) Perform the washout of the MNPs which did not impregnated scaffold using ultrasound at 180 W for 30 min. (vi) Repeat the freeze-drying step. Finally, defrost the magnetized scaffold (vii), then rinse and use (viii).

It can be easily noticed that this strategy is simple, fast and allows to employ commercial, on-the-shelf scaffolds and MNPs, implying that also non-specialized laboratories can obtain such magnetic biomaterial. Beside this very important practical aspect, the rationale of the dip-coating technique lies in the firm adhesion end entrapment of nanoparticles in the natural sub-micrometric or nanometric porosity of any material thanks to capillarity force [38]. It has been noted that electrostatic interactions would play a major role in the impregnation process [42].

The author report that the procedure described in [38] and [42] was followed, except for the initial concentration of the ferrofluid, which was  $12.5 \text{ mg} \cdot \text{ml}^{-1}$ ; for the impregnation time, which was doubled to 30 min and for the ultrasound power used during the sonication step,

which was augmented to 180 W due to the device employed.

The ferrofluid impregnation was carried out for twelve  $\beta$ -TCP and PCL scaffolds, using the 50 nm and 200 nm ferrofluid to obtain six samples for each molecular size. Two type of biomaterial can be distinguished and within them two sub-groups of scaffolds can be distinguished, each of them embedding different MNPs.

### Qualitative and Quantitative Analysis

- *Weight measurement:* During the impregnation process, scaffolds weight was carefully monitored employing a digital balance Gibertini ( $1 \text{ mg} \pm 0.5 \text{ mg}$ ). This naïve and simple measurement of the  $Fe_3O_4$  amount added to the scaffold is supposed to provide a first verification of the success of the process. It is worth noting that the balance employed has not a sufficient accuracy to ensure the precise and absolute determination of the amount of magnetic phase in each scaffolds, however these information stress the probability that a relevant quantity of MNPs was entrapped in the scaffold matrix. The weight for each process steps are analyzed using the ANOVA test in Matlab, in order to detect statistically significant variation of the scaffold weight. The findings from this semi-quantitative analysis are provided in Sect. 5.1.
- *SEM/EDS:* The presence of the MNPs in both the ceramic and polymeric matrix have been verified with Scanning Electron Microscopy (SEM) imaging. The JEOL JSM-7500FA (JEOL, Jap) microscope from Graphen Lab (iT, Genova, IT) was employed to assess the spatial distribution of the magnetite nanoparticles in the samples. The machinery was employed in the Energy Dispersive X-ray (EDX or EDS) modality. In fact, a SEM image originates from the backscattered electronic beam and the secondary electrons, but these particles carry other relevant informations, i.e. the characteristic X-ray emission due to the energy transition of the electron between two orbital levels [73]. The reflected particles are collected by silicon-drift detectors (SDDs) or by Si(Li) detectors [73]. In this way, in a single SEM session, with the image, it is acquired to the characteristic spectrum of the object under study. Hence, by analyzing the peaks of such spectrum, the presence of  $Fe_3O_4$  in  $\beta$ -TCP and  $\epsilon$ -PCL scaffolds can be easily detected.

The SEM images were analyzed using the open-source software Image Processing and Analysis in Java (ImageJ, NIH Gov.) [74]. The distributions of the pore size and radii of the magnetic nanoparticles in the scaffolds were assessed.

- *Static Magnetization:* Relevant information about the volume percentage of the magnetic phase embedded in the biomaterial, as well as the magnetization of the whole sample and the dipole moment of the single nanoparticle can be derived investigating the static M vs. H curves [41]. In other words, at a fixed temperature, applying a static magnetic field of increasing strength (from 1  $\mu\text{T}$  up to 7 T), the resulting average magnetization vector can be detected using Superconducting Interference Quantum Devices (SQUIDs) [75]. Static magnetization measurement were carried out employing the magnetic properties measurement system MPMS XL 5 (Quantum Design), applying a magnetic flux density increasing up to a maximum of 7 T, with a constant temperature of 310 K, in order to replicate the susceptibility of the particles in physiological conditions.

## 4.3 Design of the AC Susceptibility Measurement System

In this section is provided a resume of the main methods and techniques for the quantification of the magnetic susceptibility. Among the available strategies, the more accurate, reliable and the simplest to implement is selected, then redesigned to assess the magnetic spectra of the novel biomaterial under investigation. The optimized design and model of the pick-up coils for sensing the magnetic signal from the sample is presented and detailed. Finally, the information derived from the scaffolds morphological features and magnetic properties are exploited to study numerically, from a multiphysic and non-linear point of view the employment of the synthesized magnetic scaffolds in the case of bone tumor hyperthermia treatment.

### 4.3.1 State-of-the-Art of Magnetic Susceptibility Measurements

The most relevant methods and techniques present in literature used to measure the material magnetic susceptibility are summarized. The experimental setup and the measurement principles are reported for both static and frequency-dependent techniques. Thus, the most suitable, feasible and effective method can be selected. Of course, static measurement techniques can be adapted to the frequency domain and used for the purpose of assessing the AC susceptibility spectra of magnetic scaffolds. The chosen approach could hence be employed to study, simulate and implement the experimental setup to measure magnetic scaffolds properties.

The experimental techniques based on AC magnetic fields presents a very compact instrumentation, being also independent from the natural residual magnetization of the

Material Under Test (MUT) [76], [75]. As discussed in Sect. 2.2.2, the magnetic susceptibility ( $\chi$ ), or magnetic permeability, is a material property strictly related to the current induced in circuits with inductive elements such as coils [75]. In fact, the inductance of a coil can be defined as [76]:

$$L = \mu_r \mu_0 \frac{N^2 A}{l} \quad (4.1)$$

where  $N$  is the total number of turn,  $A$  is the cross-section area of the inductive element (in  $m^2$ ) and  $l$  is the coil length, given in m. This physical quantity, which is related to the capability of an alternate current carrying conductor to induce an electromotive force, is directly proportional to  $\mu_r$ , therefore, in a circuit with two identical coil elements: one air cored and the other completely filled with the sample (with permeability  $\mu_s$ ), their inductances can be written as:

$$\begin{aligned} L_a &= \mu_0 \frac{N^2 A}{l} \\ L_s &= \mu_s \mu_0 \frac{N^2 A}{l} \end{aligned} \quad (4.2)$$

Then, taking the difference between the two Eq.s (4.2), the inductance variation between the two element is linearly dependent on the unknown sample magnetic permeability [76]:

$$\Delta L = L_s - L_a = \mu_0 \frac{N^2 A}{l} (\mu_s - \mu_0) = k(\mu_s - \mu_0) \quad (4.3)$$

The proportionality constant account for geometric factors, e.g. filling factor, demagnetization contribution and mutual inductance [77]. It is worth noting that if  $\mu_s \gg \mu_0$ , then air contribute can be neglected, implying that measurable slowly overestimated inductance changes are related to the sample properties [76]. For most of the magnetic materials the  $\Delta L/L$  varies between  $10^{-5}$  and 0.1 [75], [76].

Having clarified the link between inductance and magnetic susceptibility are related, it is necessary to define how such physical quantity can be measured.

**AC bridge circuits** are often employed [78], [79]. Generally speaking, AC bridges are circuits of four inductances connected to a oscillator, as presented in Fig. 4.2.

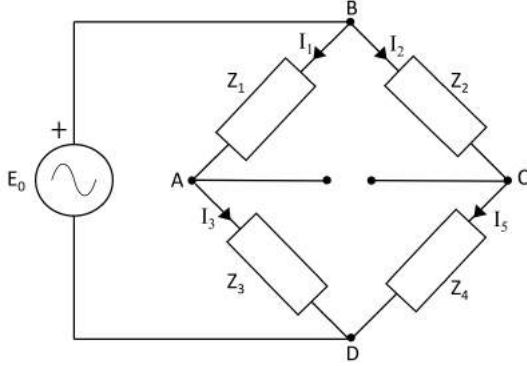


Figure 4.2. Generic AC bridge circuit for inductance measurements.

The bridge is balanced if the voltage drop between nodes A and B is equal to the tension on BC nodes, then if  $I_1Z_1 = I_2Z_2$ . Since  $I_1 = E_0/(Z_1 + Z_3)$  and similarly  $I_2$ , substituting hold that [79]:

$$Z_1Z_4 = I_2Z_3 \quad (4.4)$$

However, the impedance is a complex quantity [78], therefore, the bridge is balanced if the product of the modulus of the impedance of opposite arms is equal to the product between the other two; and if the phase of adjacent arms is adjusted. In mathematical terms [79]:

$$\begin{aligned} |Z_1| \cdot |Z_4| &= |I_2| \cdot |Z_3| \\ \theta_1 + \theta_2 &= \theta_3 + \theta_4 \end{aligned} \quad (4.5)$$

where  $\theta_i$  stands for the  $i$ -th phase angle of the bridge arm. The Maxwell bridge measures a unknown inductance, i.e.  $L_s$ , in terms of a known variable capacitance [78], [79]. The capacitance is connected in parallel to a resistance, while the opposite arm is a series of a resistor and the inductor. The other two arms have a resistive nature, but one of such element has a variable resistance, which is needed to report the system to null conditions. This type of system it is often employed coils with a good quality factor (between 1 and 10) and small phase angles. However, if the phase angle involved in the measurement are not negligible, using coils with a high-quality factor ( $Q \gg 1$ ), the **Hay bridge** is a suitable circuit for measuring inductances [79]. The latter measurement device differs from the former only by the type of inductance and the position of the capacitor: in this case a series of a variable resistor and a fixed value capacitance are

opposed to the  $RL_s$  arm. Another possible solution to the susceptibility measurement problem is the **Inductive Wheatstone bridge** designed by de Vries and Livius [80]. This four inductance non-resonant bridge can perform susceptibility measurement from 200 Hz to 1 MHz, for variable applied field strength (maximum 0.42 T) and for temperature from 1.2 K up to room temperature. Moreover it possess an accuracy of 1%, which is an acceptable value for most cases. However, the signal conditioning of these piece of instrumentation is very complicated and hard-working [80]. Since the bridge balancing procedure are long, cannot be always automatic, the use of **Balanced Transformers** was suggested [76], [81], [82]. In the method of Christie and Symons [82] two sensing coils are connected in series opposition, and each of them is surrounded by a coaxial exciting primary coil, which, in turns, carries an AC current at the working frequency of 1 kHz. The residual output of the sensing coils is balanced to zero by trimming resistors and capacitors. The rationale of this class of electronic circuits is that the change in the mutual inductance between two coupled coils, due to a susceptible sample placement, is strictly related to the altered flux linkage in one coil with respect to the initial value inducted by the currying current in the other coil [76], [82]. Actually, when the para- or ferromagnetic sample is inserted in one of the inner coil, the induced voltage in the secondary coil is monitored. Indeed, moving from the equilibrium condition of a null voltage drop across the coils, the flux linking the coils and then the net output voltage augment proportionally to sample susceptibility. By tuning to resonance the exciting coils, since they are fed by an oscillator of a commercial lock-in amplifier, whose phase-sensitive detector is used to process and display the out-of-balance signal, the real and imaginary part of the susceptibility can be computed [76], [82]. Performing a meta-analysis, this configuration is actually a complicated case of a RLC circuit, which can be used in its simplest form to measure the complex magnetic permeability of a sample [83]. However, this solution was recently employed, with the addition of a lock-in amplifier, for the measurement of the AC magnetic susceptibility of various MNPs samples [25].

Recently, a miniaturized AC susceptometer was proposed by Park *et al.* [84]. Moving from the claim that conventional susceptometers [76] are bulky, expensive and are designed for extreme conditions (e.g. low temperature or high DC magnetic field, a simple handheld prototype was designed. This system is consists of an alternate current source, a set of two differential sensing coils which are connected to an ultra-sensitive lock-in amplifier (LIA), which is exploited to extract the in-phase and out-of-phase component of the differential voltage signal from the sensing coil output [84]. The two identical coil pairs (1000 turns,  $\varnothing$  9.53 mm, 57.25 mm in length, with a wire of 0.2 mm, i.e. 32 AWG) are excited by

a primary coil and their position inside the latter has to be adjusted to compensate the offset voltage [84]. Such system was employed to measure the AC spectra of MNPs-based solutions, measuring susceptibilities of about  $1.2 \cdot 10^{-3} \div 0.2 \cdot 10^{-3}$ .

As result from this discussion, susceptibility measurements are non-contact and based on the comparison of inductances [76]. Precision sensing coils, AC sources are the major components of the system, but, to increase the sensitivity, low-noise lock-in amplifiers (LIA) are exploited in the quantification fo in- and out-of phase magnetic susceptibility [84]. However, the use of this bulky and high-cost instrumentation can be avoided using nominal analog circuitry present in normal laboratory use [85]. Das et al. [85], [86] proposed an automatic strategy to use simplified instrumentation in order to measure in- and out-of-phase complex magnetic susceptibility of magnetic samples at a maximum frequency of 400 kHz. Their system is composed by two matched coils, which are excited separately by a two-channel arbitrary voltage generator through an high-precision foil resistor, as in Fig. ??.

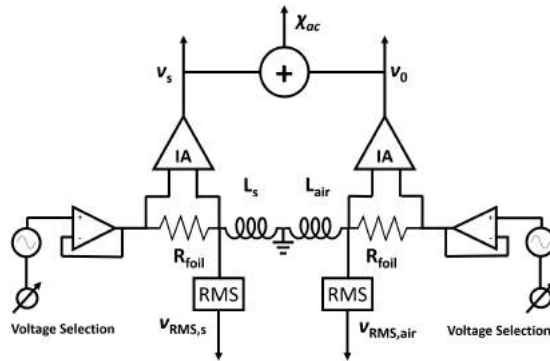


Figure 4.3. The AC Susceptometer designed by Das et al. [86]. The sensing coils are supplied with an identical current, adjusted by a software routine, the voltage across them is converted in RMS to evaluate the complex magnetic susceptibility of the sample under test.

The root mean squared (henceforth rms) currents inside the coil conductors ( $I_{RMS}$ ) should be equal to ensure a differential measure, therefore they are adjusted correcting the amplitude of the function generator and re-balancing the system. In this way it is possible to obtain the modulus of the complex impedance, which can be written as [86]:

$$\chi_{ac} = k\Delta L = \frac{k}{2\pi f} \left[ \sqrt{\frac{v_{RMS,s}^2}{I_{RMS}^2} - R_{coil}^2} - \sqrt{\frac{v_{RMS,air}^2}{I_{RMS}^2} - R_{coil}^2} \right] \quad (4.6)$$

where  $R_{coil}$  is coil resistance, whereas the voltage drops across the pick-up coils (i.e.  $v_{RMS,s}$

and  $v_{RMS,air}$ ) are measured and summed to derive, by a software routine, the phase between them [85], [86]. The real and imaginary part of the complex magnetic susceptibility can hence be obtained:

$$\chi(\omega) = \chi' + j\chi'' = \chi_{ac} \cos(\psi) + j\chi_{ac} \sin(\psi) \quad (4.7)$$

where angle  $\psi$  is defined as follow [86]:

$$\psi = 2\cos^{-1}\left(\frac{I_0 R_{foil}}{2V_0}\right) \quad (4.8)$$

being  $V_0$  and  $I_0$  the amplitude of voltage and current source, whereas  $R_{foil}$  is the foil resistance (see Fig. 4.3).

From the works presented and discussed the following design consideration for any AC susceptometer can be deduced [76], [86]:

- Moderate to high sensitivity is required, therefore special attention should be paid to the screening of leads and shielding of components, and to the prevention of temperature variations.
- The sensing coils are required to provide, from an input of a few volts, a field of about  $100 \mu\text{T}$  r.m.s. of reasonable uniformity ( $\pm 2\%$ ) over the sample, and to have a high quality factor.
- The pick-up coils must be designed to provide both a homogeneous magnetic field for a sample of given size and a ratio between sample and coil volume (i.e. a filling factor) reasonably high, meaning that the change of inductance due to the sample is maximized.
- The measure of the inductance variations are strictly related to a non-uniform sample exposure; the line capacitance; coil resistance and inter-turn capacitance. All of these quantities varies with temperature and frequency, therefore, as will be discussed in the next subsection, strongly affects the cut-off frequency of the instrument [75].
- The currently available digital electronic allow to reach a sufficient sensitivity for the great majority of susceptibility measurements [76].

The last measurement strategy of [86] is very appealing thanks to its ease of implementation and the use of low-cost commercial on-the-shelf components. However, further improvements can be made, e.g. the upper frequency limit can be improved to at least

700 ÷ 900 kHz. Not only, the software adjustment procedure may be avoided employing a different current source for the coil components. Moreover, the choice of operate with a fully analog signal is questionable and then, nowadays, the idea of acquiring a high-resolution digital signal (e.g. 14 bit,  $120 \text{ Msample}\cdot\text{s}^{-1}$ ). This is the starting point for the design of the measurement system for the properties of magnetic scaffolds of the present dissertation work. The main goal is to investigate this physical quantity to derive relevant information regarding the material (clustering, packaging and level of interaction of the particles in the sample [26]) to better define the heat dissipation mechanism in these novel implants, thus ensuring an effective HT treatment.

#### 4.3.2 Design of Air-Core Coils

The core element of any magnetic measurement system is the sensing coil [75]- [86]. As information note on terminology, the term *coil* is employed in the literature as the general expression for any real configuration. Anyway, it is possible to distinguish between a *solenoid*, i.e. a coil with length greater than its diameter, and a *thick coil*, i.e. a coil with a core radius comparable with the thickness of the wound [87]. In this section the model and equation used for the design of the pick-up coil for the AC susceptometer are presented and discussed.

##### Inductance Calculations

The principle of measuring the magnetic susceptibility by accounting for the inductance variation and looking at the voltage across the coil is the simplest expression of the well-known Faraday's law of induction [75]:

$$V = -\mu_r\mu_0 N A \frac{d\mathbf{H}}{dt} = \mu_r\mu_0 N A \cdot j\omega \mathbf{H} \quad (4.9)$$

The instrument sensitivity is therefore imputable to the value and order of magnitude of the induced voltage [75]. From the literature [84], [86], it can be noticed that values of circa 1 mH are employed. It is estimated that such a value would allow to acquire a significant signal, e.g. about 100  $\mu\text{V}$ , in the low-frequencies. Therefore, the voltage signal must be maximized. From Eq. (4.9) it is evident that the coil cross-section area ( $A$ ) should be increased, as well as the field inside the inductive element. Since the area is proportional to the squared power of the inner diameter [75] and the magnetic field inside the coil is subject to both the second and third design requirements (see 4.3.1), a trade-off should be reached. Taking into due account these evidences, the design of the coil to reach a desired

inductance is a trivial task.

It is possible to fully describe any generic coil from its geometry, as shown in Fig. 4.4. Typically, a magnet wire of enameled or insulated copper wire with diameter  $d$  is wound around a paper support with dimension  $D$ , i.e. the coil inner diameter. The wire is wound tight (or with a pitch,  $p$ ) until the total number of turns  $N$  is obtained. The winding thickness is  $c$ , which is also the length given by  $D_e - D$ . The height of the windings or coil length is  $l$ .

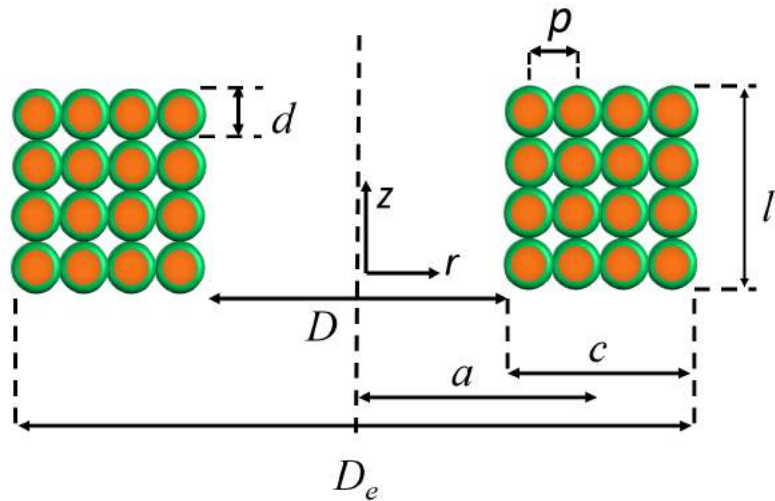


Figure 4.4. Cross-section of a coil. The coordinate system is cylindrical (rz-plane) and it is set in the coil center. The copper wire diameter is  $d$ ,  $D$  indicates the coil inner diameter, whereas  $D_e$  is the external diameter. The symbol  $a$  is the mean radius of the turns. Finally,  $c$  is winding thickness and  $l$  is the coil length.

As previously stated, the inductance is a function of coil shape [75], [88]. A thick coil have a large  $c/2a$  and  $l/c$  ratio, whereas a thin coil present a small value of  $c/2a$  with a large length to turn thickness ratio [88]. With this arrangements, the well-known formula and working table provided by Grover [88] can be exploited to size the coil.

If the coil have a cross-square section ( $l=c$ ), assuming a homogeneous current distribution in the conductors, and the inductance, given in  $\mu\text{H}$ , can be computed by the following formula [88]:

$$L = 0.001 \cdot aN^2 P'_0 \quad (4.10)$$

where  $P'_0(c/2a)$ . The case of a squared coil has been shown to be somehow limiting, therefore, in order to maximize the inductance value, for a given length of a chosen wire, a Brook's coil can be built. The inner and outer diameter of the coil are equal to  $2c$  and  $4c$  respectively. The inductance of this class of bobbin present a maximum for  $2a/c = 2.97 \approx 3$ , in other words [88]:

$$L = 0.0005 \cdot \frac{l^{5/3} \left(\frac{c}{2a}\right)^{3/2}}{(\pi)^{5/3} d^{2/3}} \cdot P'_0 \approx 0.016994 \cdot aN^2 \quad (4.11)$$

Finally, the most general and adjustable configuration is the circular coil with rectangular cross section of any desired proportions. In such a case the assumption on the homogeneous current distribution is revised and the consequence of neglecting the space occupied by insulating material is no longer respected, therefore a correction of inductance value due to the reduction of coil capacitance is required [88]. This considerations reflects on the inductance expression for the thin coil:

$$L = 0.019739 \cdot \left(\frac{2a}{b}\right) aN^2 \cdot K' \quad (4.12)$$

where  $K' = K - k_0$ , being  $K(2a/b)$  and  $k_0(c/2a)$  [88]. On the other hand for the thick coil the equation is very similar to Eq. (4.10), but the factor  $P'_0$  is a rather complicated function of  $c/2a$  ratio and the inductance reduction on the axial direction [88].

The formulas from [88] do not account directly for the mutual inductance contribution (depicted in Fig. 4.5) to the overall inductance. The term  $M_{(i,j)(h,q)}$  can be very significant in multi-layer coils [89] and the calculation of the total inductance employing its definition can result to be more accurate [88]. Addressing the  $i$ -th layer, the  $j$ -th turn and the  $q$ -th turn of the  $h$ -th layer, the mutual inductance can be evaluated as:

$$M_{(i,j)(h,q)} \approx \frac{\mu_0}{2} \int_0^{2\pi} \frac{R_i R_h \cos(\theta)}{\sqrt{d_{i,j}^2 + R_i^2 + R_h^2 - 2R_i R_h \cos(\theta)}} \quad (4.13)$$

where  $R_i$  and  $R_j$  are the turn radii of the  $i$ -th and the  $j$ -th layer, while  $\theta$  stands for the angular coordinate of the turn. It was shown by Massarini *et al.* that this integral can be reduced to the following form [89]:

$$M_{(i,j)(h,q)} = \mu_0 \sqrt{R_i R_h} \left[ \left( \frac{2}{w} - c \right) \cdot I_1(w) - \frac{2}{w} \cdot I_2(w) \right] \quad (4.14)$$

where  $I_1$  and  $I_2$  being the Legendre's function of the first and second kind, respectively, and with:

$$w^2 = \frac{4R_i R_h}{d_{i,j}^2 + (R_i + R_h)^2} \quad (4.15)$$

Hence, the overall inductance can be finally found as the sum of every contribution [89], [90]:

$$L = \sum_{i=1}^N \sum_{j=1}^N \sum_{h=1}^N \sum_{q=1}^N M_{(i,j)(h,q)} \quad (4.16)$$

The inductance calculation can be carried out with one of the proposed coil configurations [75], [88], [89]. Anyway, to meet the design criteria and requirements from Sect. 4.3.1, the coil inner diameter ( $D$ ) should be as close as possible to the scaffolds diameter, i.e. 5 mm. Moreover, the coil height lower limit must be fixed to the height of the biomaterial disks, so that the sample under test would be completely buried inside the sensing element, causing a noticeable inductance change [76].

### Stray Capacitance Estimation

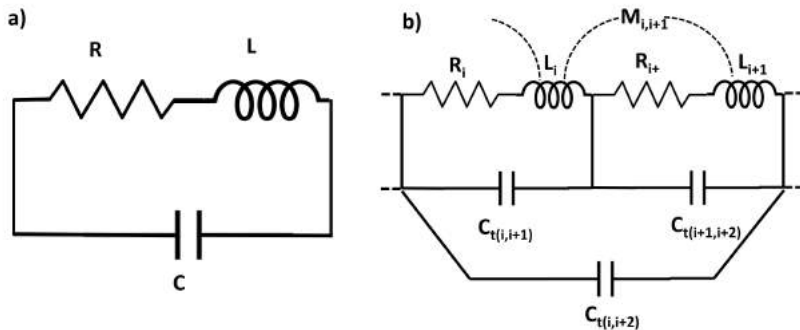


Figure 4.5. RLC circuital lumped parameter representation of an unshielded coil: a) simplest model, b) high frequency equivalent circuit of a single-layer solenoid air-core inductors. Redrafted from [91].

A coil can be represented in a far complex way than a simple inductor. The simplest model is the basic lumped parameter circuit shown in Fig. 4.5.a [88], [91]. The device is represented as a RLC circuit because it have a resonant behavior, characteristic for a second-order system [77]. The issue addressed in this section is to define clearly the methodology to define the capacitance of a coil. Such information is needed to avoid the fabrication of a device whose cut-off frequency felt within the band of interest (remember the discussion about Sect. 4.3.1). Furthermore, by evaluating the expected capacitance of

the coil it is possible to assess the order of magnitude of the quality factor, which is an important parameter for the measures [75], [76].

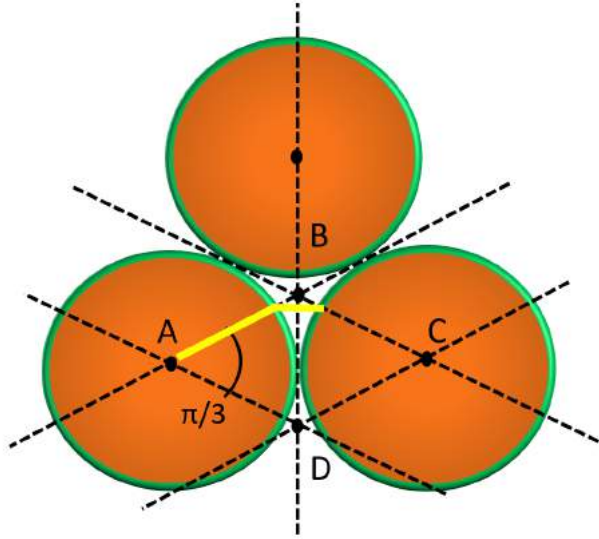


Figure 4.6. Physic-based model of the single-cell used for the evaluation of stray capacitance in multi-turn coil. The main path considered for the electric field line is highlighted in yellow. Redrafted from [91].

In high frequency applications (from several tens of kHz up to tens of MHz) parasitic or stray capacitance are crucial for the coil design and their effect must be minimized [91]. The capacitance establish between two conductors surface, i.e. turn-to-turn capacitance or  $C_{tt}$ ; between turns of different layers and the turn-to-core contribute. Assuming no shield, which is exactly our case, considering the fringe effects negligible, for an air-core coil the electric field line can be retain to be shared only to adjacent conductors [90], [91], such as in the basic-cell shown in Fig. 4.6. With this model, the turn-to-turn capacitance can be computed by integrating the electric field lines orthogonal to the conductor surface including the capacitance of the insulating coating for an arc of  $\pi/3$  and the capacitance of the air gap [90], so that, under the hypothesis of that the coating is much lower than the difference between the pitch and the wire diameter and  $p \geq d$ , the final expression for  $C_{tt}$  is [91]:

$$C_{tt} = \frac{\pi^2 D \epsilon_0}{\ln \left( \frac{p}{d} + \sqrt{\left( \frac{p}{d} \right)^2 - 1} \right)} \quad (4.17)$$

It is evident from Eq. (4.17) that  $p \geq d$  is a necessary condition, although, if the wire are tightly bound, i.e. for  $p = d$ , the  $C_{tt}$  is equal to zero. Finally, the overall stray capacitance can be easily computed as [89], [90], [91]:

$$C_s = \frac{C_{tt}}{N - 1} \quad (4.18)$$

These equation were employed to design the coil to avoid the first self-resonant frequency to present in the measurement band [76], [92].

### Coil DC and AC Resistance

To assess the overall efficiency of the pick-up coil inductor, the calculation and measurement of the winding AC resistance,  $R_{ac}$ , must be performed. Moreover, as explained in detail in Sect. 4.3.1, the coil resistance is an important physical quantity which enters in the evaluation of the modulus of the complex magnetic susceptibility (see Eq. (4.6)). This means that knowing the response of  $R_{ac}$  with frequency, the magnitude of its variations can be quantified and allow to operate some corrections if needed.

The static resistance value, called  $R_{dc}$ , can be easily evaluated considering the copper resistivity ( $\rho_{Cu}=0.018 \text{ } \Omega \cdot \text{mm}^{-1}$ ), the cable length ( $l_c$ ) and the cross-sectional area of the wire ( $A_{wire}$ ), in mathematical terms [75]:

$$R_{dc} = \frac{\rho_{cl} l_c}{A_{wire}} \quad (4.19)$$

The DC value of the resistance is supposed to affect the measurement and this value cannot be too high, therefore, the diameter of the copper wire employed for the coil windings was selected higher than 0.5 mm, because tenth or few  $\Omega$  of resistance can be obtained for winding of lengths from 20 m to 50 m.

The intrinsic nature of the measurement of the AC magnetic susceptibility of a material necessary prescribes that the source has a variable frequency [76]. Therefore, as for the interesting strategy adopted by Das et al. [86], the influences of resistance variations in the frequency range of interest must be considered and quantified.  $R_{ac}$  is known to increase in a way proportional to  $\sqrt{f}$  [88]. Anyway this is a very approximate result which works better in the MHz range, but, at lower frequencies, the winding AC resistance should be computed after solving the equation for the magnetic flux in a coil portion [87], including the skin depth and proximity effects [88]. Employing a multi-dimensional approach which relied on the assumption of non-uniform magnetic field across the conductor cross-sectional area, the **Reatti & Kazimierczuk method** allow to accurately predict the frequency-dependent

response of winding resistance [93]:

$$R_{ac} = R_{dc} \frac{\gamma}{2} \left\{ \frac{ber(\gamma)bei(\gamma) - bei(\gamma)ber'(\gamma)}{ber^2(\gamma) + bei^2(\gamma)} - 2\pi\eta^2 \left[ \frac{4(N_t^2 - 1)}{3} + 1 \right] \frac{ber_2(\gamma)bei(\gamma) - bei_2(\gamma)bei(\gamma)}{ber^2(\gamma) + bei^2(\gamma)} \right\} \quad (4.20)$$

where the term  $\gamma$  is defined as the ratio between the conductor diameter and  $\sqrt{2}$  times the skin depth, which is obviously  $\delta = (\pi\mu_0\mu_r\sigma f)^{-1/2}$  [1], [88], [93]. The porosity factor is defined as  $\eta = dN_t/l$  [93]. About the notation, the Kelvin function are employed in Eq. (4.20):  $ber$  and  $bei$  are the real and imaginary part of the Bessel function of the first-kind, respectively, whereas the functions with the subscripts are the special case of the series expansion stopped at the desired order [94].

### Estimating the Coil Q-factor

Employing the ac winding resistance calculated using (4.20), together with the overall stray capacitance given by Eq.s (4.17) and (4.18); and the total inductance (e.g. derived from (4.14)), the coil impedance is easily obtained [93]:

$$Z_{coil} = R_{coil} + jX_{coil} = \frac{R_{ac} + j\omega L \left( 1 - \omega^2 LC - \frac{CR_{ac}^2}{L} \right)}{\left( 1 - \omega^2 LC \right)^2 \left( \omega L R_{ac} \right)^2} \quad (4.21)$$

For frequencies much lower than the first resonant frequency [92], the equivalent series reactance  $X_{coil}$  of the circuit in Fig. 4.5.a can be written as  $X_{coil} = \omega L$ , thus by inverting and taking the ratio of the reactance modulus with respect to the reactive part of the complex impedance, the coil Q-factor is [93]:

$$Q = \frac{|X_{coil}|}{R_{coil}} = \frac{\left| \omega L \left( 1 - \omega^2 LC - \frac{CR_{ac}^2}{L} \right) \right|}{\left( 1 - \omega^2 LC \right)^2 + \left( \frac{\omega L}{R_{ac}} \right)^2} \quad (4.22)$$

The cited equations were implemented in Matlab (The MathWorks Inc., US) to evaluate the inductance, capacitance and resonance of the coil, as well as the resistance, impedance and Q-factor of the coil. These theoretical basis are exploited to verify the constructed coils using the data of the Agilent 4842A LCR meter (Agilent Technologies, US).

### A Genetic Algorithm for the Non-linear Constrained Optimization of Sensing Coil

The design of a coil for high-frequencies applications, i.e. the sizing of diameter, height, total number of layer and the wire dimension, is considered a non-linear programming problem subject to strict complex constraint [95]. Defining a set of constant parameters  $\mathbf{k}$ , given the variable vector, a suitable objective function  $F(\mathbf{k}, \mathbf{x})$  should be minimized finding the set of solution for which the condition on the real-valued scalar function  $u(\mathbf{k}, \mathbf{x})=0$ ,  $v(\mathbf{k}, \mathbf{x})\leq 0$  are satisfied in the range  $\mathbf{x}_l \leq \mathbf{x} < \mathbf{x}_u$ . To formulate this non-linear constrained ill-posed problem, as a first step, the design of a single-layer coil was investigated. As suggested by the work of Grandi et al. [95], the variables chosen variable are  $\mathbf{x}=(N,D,d,p)$ . The coil volume was selected as objective function:

$$F(\mathbf{k}, \mathbf{x}) = V_c(N, D, d, p) = (N - 1) \cdot p \frac{\pi}{4} D^2 \quad (4.23)$$

The desired first resonant frequency ( $f_r$ ) and a target inductance ( $L_{fix}$ ) value are the fixed parameter inserted by the user. From the formula of  $f_r$  the capacitance  $C_{fix}$  is evaluated [95]. These two lumped parameter force the algorithm to identify a set of variable that allow the fitness function to respect the following constraints:

$$\begin{aligned} t(\mathbf{x}) &= L(N, D, d, p) - L_{fix} = 0 \\ u(\mathbf{x}) &= C(N, D, d, p) - C_{fix} \leq 0 \end{aligned} \quad (4.24)$$

and the following obvious geometrical identity derived from Fig. 4.4 and from physical limitations:

$$\begin{aligned} v(\mathbf{x}) &= N \geq 1 \\ w(\mathbf{x}) &= p \geq d \\ z(\mathbf{x}) &= D \geq d \end{aligned} \quad (4.25)$$

Grandi et al. [95] chose a sequential quadratic programming algorithm to solve this problem. Anyway, since this problem is essentially a non-linear multi-objective optimization issue, there are several strategy which can be used to solve it, namely Particle Swarm Optimization [96], the target field approach [97], Genetic Algorithms (GA) [98], [99]. GA algorithms, as defined by Holland [100], are randomic programming strategies, often called

evolutionary computation techniques, which try to reproduce the mechanisms of natural evolution, i.e. reproduction (the entering of new individuals in a population); mutation or crossover (the mixture of parents' information content) and selection. In particular, the selection process is allowed to respect the Darwin's principle of the survival of the fittest individual [98],- [100] or, from the point of view of our optimization problem, the best solution vector  $\mathbf{x}$ .

Therefore, the preliminary step of sizing and design the coil was performed employing the GA toolbox in Matlab, following the resolution scheme presented in Fig. 4.7. A 300'000 individuals are the initial population, which are subject to 200 iterations, with a migration step of 5 iteration.

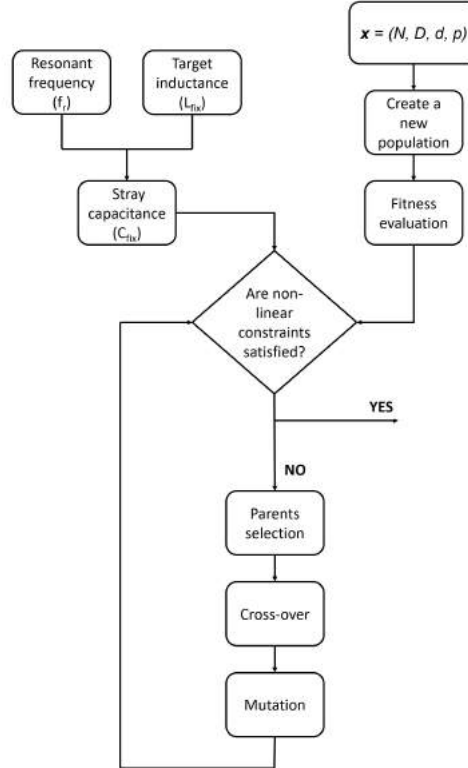


Figure 4.7. Meta-heuristic Genetic Algorithm (GA) for the optimal design of a coil with desired inductance and first-resonant frequency.

The search for a solution of a non-discrete variable in a wide range of multiple possible solution is fastened exploiting the evolutionary programming strategy, also allowing for a sub-optimal solution. The proposed computational approach was also modified to account

for multi-layer parameter by simply adjusting the constraints [88]. However, the final result should be further tests in order to verify if the design requirements are matched (see Sect. 4.3.1).

### FEM Simulation of the Designed Coil

The magnetic field distribution inside the device and the corroborative calculation of the coil inductance are performed with the open-source Finite Element Method (FEM) solver for magnetic problems FEMM v.4.2 (FEMM, Waltham, MA). This particular software, despite being less elaborate and user-friendly than the well known high frequency full-wave commercial products Ansys Electromagnetic Desktop (ANSYS, Inc., US) or CST (CST Computer Simulation Technology GmbH, Ge), is a reliable tool for the coil modeling and simulation in 2D. In fact, the wire diameter (tenths of mm or few millimeters) is order of magnitude lower than the wavelength of the problem (in vacuum, at 1 MHz,  $\lambda \approx 300m$ ), hence using FEM the meshing and solving is a trivial task. Therefore, an *ad hoc* approach for the solution of Maxwell equations (Eq.s (2.1)) was developed in FEMM [101].

#### 4.3.3 The Measurement System

After having designed properly the two sensing coils for the measurement of the magnetic susceptibility of biomaterials as a function of frequency, the choice of the instrumentation and the scheme are presented and discussed.

From the discussion of Sect. 4.3.1 does not require a circuit of the transformer type, as the one employed for investigating the Brownian relaxation dynamic of MNPs suspension in [102]. In fact, from the previously discussed state-of-the-art, the very fast, simple, intuitive and cost-effective approach of Das *et al.* [86] was selected. However, the measurement system was completely analogic and required a feedback strategy to adjust the current flowing in the coil wires, because, to find the real and immaginary part of the magnetic susceptibility, the field source in the two pick-up elements would be as equal as possible. Then, the first contribution of this thesis work is a major improvement and a valuable solution in the design of AC susceptometer. In fact, rather than using a foil resistance, which has a very low tolerance, the use of current mirrors integrated circuits [103] would allow to drive an almost identical current in coil conductors. Briefly, a current mirror is the mainly employed as a constant current source of integrated circuits and consists of two identical transistors (MOSFET or BJT ( $Q_1, Q_2$ ) whose gate and source are set to the same voltage, determining the  $I_{ref}$  for the  $Q_1$  element to be equal (i.e. with

the same channel width and length) to the output current from  $Q_2$  [103]. In mathematical terms, if the transistors are identical and works in saturation regime:

$$\begin{aligned} I_{ref} &= \frac{V_{dd} - V_{gs}}{R} \\ \frac{I_o}{I_{ref}} &= \frac{(W_{ch}/L_{ch})_2}{(W_{ch}/L_{ch})_1} \end{aligned} \quad (4.26)$$

With respect to the MOS current mirror, the BJT-based one have a non-zero base current, which cause a slight error in the transferred current, and the ratio  $I_o/I_{ref}$  is proportional to the emitter-base area ratio of the junctions [103]. Therefore, as current source for our circuit the Infineon BCV61CE6327HTSA1 Dual NPN Transistor (Infineon Technologies AG) was chosen. It allows to control a current of maximum 100 mA (which can produce a noticeable magnetic field flux inside the coil), and work with voltages up to 30 V.

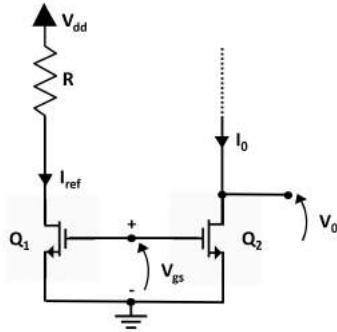


Figure 4.8. Current mirror: it is implemented using two identical transistors, working in saturation regime, polarized by the same gate-source voltage, which determines an output current equal to the reference one. Redrafted from [103].

The final scheme of the measurement system is presented in Fig. 4.9. The RF voltage supply ( $I_{ref}$ ,  $I_o$ ) produce the chosen nominal tension at the desired frequency, the current mirror receive this signal as input, producing the two feeding current for the two coil with inductances. At this point, two induced voltages appears across the sensing elements, as stated by Eq. (4.9): in absence of the sample these signals would then be equal, however, the flux linked to the magnetic scaffolds inside the sensing coil causes the inductance to increase significantly ( $\Delta L/L \geq 0$ ). To quantify these differences due to the sample under test, the coils signal is acquired by the RedPitaya STEMLAB 125-14 board [104].

This low-cost measurement electronics is a 14-bit data acquisition board, whose sampling

rate is 125 Msample/s. Moreover, it has a Dual Core ARM Cortex processor, a DDS3 RAM with 512 MB capability, a FPGA module, also 4 slow ADC elements and, finally, 32 GP/IO unit [104], [105].

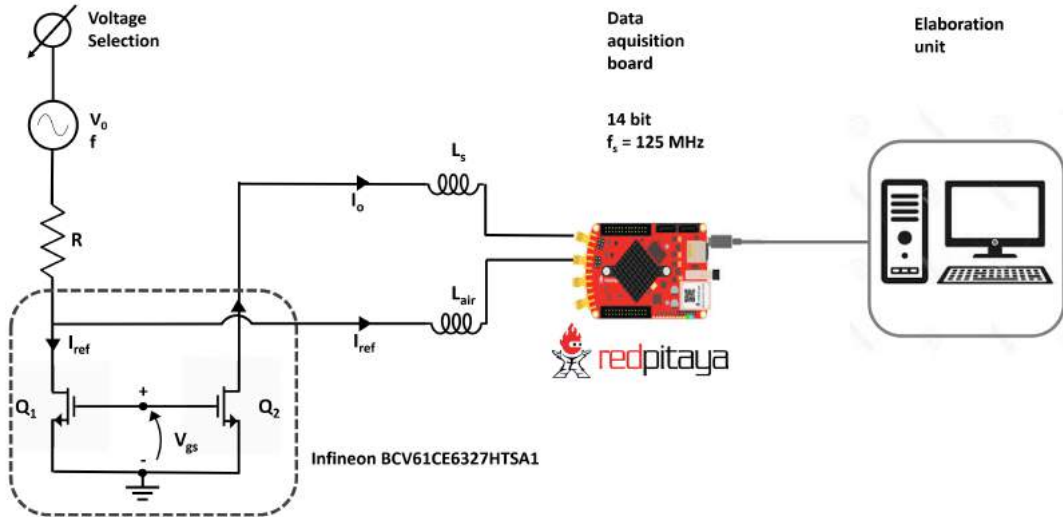


Figure 4.9. Scheme of the designed AC Susceptometer for measuring the magnetic susceptibility of the synthesized ferrofluid-impregnated scaffolds. A sinusoidal voltage at a given frequency is driven to the Infineon BCV61CE6327HTSA1 current mirror, then, the two equal currents feeds the designed pick-up coils. The difference between the induced voltages across the coils is acquired and digitalized by the RedPitaya acquisition board (14 bit, sampling rate of 120 MHz), and, finally, processed using a Matlab routine. This measurement system allows to derive the real and imaginary part of the magnetic susceptibility of the sample.

The digitalized high-resolution data acquired by the RedPitaya unit are sent to a PC module for further elaboration. The data acquisition board is controlled using Matlab. Therefore, the extraction of the real and imaginary part of the magnetic susceptibility via Eq.s (4.6) and (4.8) is performed using a suitable Matlab script.

The measurement of  $\chi_{ac}$  are performed for the  $\beta$ -TCP ceramic and the  $\epsilon$ -PCL polymeric scaffolds loaded with 50 nm and 200 nm MNPs from 10 Hz to 1 MHz.

### Thermographic Investigation: SAR Evaluation

As discussed in the Sect. 3.1, the power dissipation of a system of magnetic nanoparticles can be quantified in four ways [106]. The **magnetic methods** are:

- *Hysteresis Loop*: the heat losses can be estimated from the product of the applied frequency and the spread of the area underlying the hysteresis curve. Anyway, only

the lower limit of the experimentally observed SAR values is found [25], [106].

- *AC Magnetic Susceptibility:* the power dissipated by the system scaffolds plus MNPs can be easily evaluated using Eq. (2.23) by knowing the imaginary part of the magnetic susceptibility at the desired working frequency [20], thus allowing to easily derive the SAR. This methodology is more accurate than the hysteresis one and can be performed for magnetic scaffolds after our measurements [107].

In this dissertation work, the AC Magnetic Susceptibility method is employed, but, to clearly define the behavior of magnetic scaffolds under a RF field, this is compared to another literature standard. Therefore, the so-called **thermal methods** are:

- *Calorimetric Measurements:* the SAR values are derived quantifying the heat exchanged by a given sample under very strict adiabatic conditions [87]. Anyway, the benchmark for these tests requires complex isolating systems and vacuum-pumps, as well as an accurate thermal model for estimate the heat losses.
- *Infrared Thermography:* is a reliable, accurate, non-invasive and contact-less measurement of the sample temperature rise, from which the SAR can be easily derived [108], [107], as explained in the following. Although this method permits to monitor only the surface temperature, it has the noticeable advantages of avoiding the use of RF immune optic-fiber [108], also allows to track the temperature of several samples simultaneously and real-time [107].

Among thermal methods, the thermopgraphic assessment of the SAR is selected and used for the case of magnetic scaffolds. The Fluke TiS45 thermocamera (Fluke Sys.,  $\pm 2$  °C o 2%, FR = 30 Hz) is employed to monitor the temperature rise in the sample, which is immersed in de-ionized water, and exposed to a time-varying magnetic field of various amplitude for 5 min. The camera was held orthogonal to the sample, as shown in Fig. 4.10, at a distance of 20 cm from the sample. The emissivity and convection correction of [108] was performed.

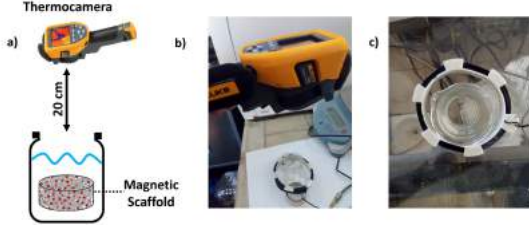


Figure 4.10. Schematic representation of the thermographic measurement for the evaluation of the heat losses due to the RF-exposure of magnetic scaffolds.

The infrared (IR) images are then processed with Matlab in order to isolate the set of pixels which belong to the scaffold and then average the temperature for every time-step. In this way a  $\Delta T$  vs. time curve is obtained. This curve is fitted using the phenomenological Box-Lucas equation [106], [108], [109]:

$$T(t) = a \left( 1 - e^{-bt} \right) \quad (4.27)$$

which is subject to the following condition:

$$\frac{dT}{dt} \Big|_{t=0} = a \cdot b \quad (4.28)$$

where  $a$  and  $b$  are fitting constants. Then, as suggested by [109], given the specific heat of the solution ( $C_{sol}$ , in  $J \cdot m^{-3} K^{-1}$ ), the SAR can be easily derived as follow:

$$SAR_{\Delta t} = C_{sol} \frac{T(0 + \Delta t) - T(0)}{\Delta t} \quad (4.29)$$

Of course, the  $\Delta t$  is not known, but the best value can be determined by identifying the plateau of the SAR variations with respect to the time interval [109].

## 4.4 An *in Silico* Model for Bone Tumor Hyperthermia Treatment with Magnetic Scaffolds

The knowledge acquired about the composition, morphology, as well as static and dynamic properties of magnetic scaffolds can be exploited for simulate and investigate their use in interesting and appealing biomedical applications. In particular, moving from a recently published numerical model [70], the hyperthermia treatment on deep-seated bone

tumors by means of implanted magnetic scaffold to perform was investigated *in silico*.

In this dissertation work the model by Fanti *et al.* [70] is employed for simulating the treatment of Osteosarcomas tumor employing the features of synthesized magnetic scaffolds, but the model is enhanced further refining the biological details, i.e. trying to include the muscle, fat and skin; and refining the description of the magnetic RF source.

#### 4.4.1 Problem Statement: Orthopedic Oncology

The bone cancers are a wide class of rare neoplasms (3 on 100'000 person per year) [110]. They afflicting patients with ages of  $10 \pm 20$  years, mostly [111]. These neoplasms can be benign, intermediate or malignant in nature. Another way of classifying them is the tissue of origin, i.e. bone-forming cancers (Osteosarcomas, OS), cartilage-forming (Chondrosarcomas), bone-marrow (Ewing sarcoma), and soft-tissue ones (Fibrosarcoma, FS) can present [112].

The OS and FS are of interest in this thesis work. This two type of tumor can be distinguished considering their architectural characteristics and physio-pathological expression [110]- [111]. In fact, the OS are very aggressive and malignant bone tumors, characterized by bone matrix or osteoid production [111]. Moreover, osteosarcomas may reach 5 cm of dimensions, while growing radially around big vessels, *i.e.* in an angiocentric fashion, meaning they are tumors with a noticeable vascularization [110]. Prognostic factors depend on treatments, though survival rate ranges from 30% to 40% [1]. As regards the fibrosarcomas, they are malignant neoplasm which arrange in interlaced trabecular bundles, due to their nature [113], and often extend to soft tissues [110]. FS present 28% 10-year survival rate [113].

The OS and FS are reported to often affect long bones, such as the distal femur, tibia, and humerus [114]. Anyway, since these neoplasms have different clinical characteristics, which, combined with their histology and pathology, implies a diverse staging, hence the available and required treatments can be different. In particular, nowadays, the accepted clinical treatment are chemotherapy, radiotherapy, osteotomies, ablative surgery and/or intralesional excision, *i.e.* bone curettage [110] - [114]. Anyway, it is reported that about the 15% of the cited surgical intervention surely results in tumor recurrence [112]. In order to prevent the occurrence of this clinical issue, clinicians and biomedical engineer worked to study, test and propose novel therapeutic strategies to eliminate the tumorous cells. This is why several work on combined radiotherapy and chemotherapy protocols [115], hyperthermia [31], [116], immunotherapy [117] and smart drug nanocarriers [118].

Among the cited innovative strategies, Hyperthermia (henceforth HT) is thought to

soon became a clinical reality [109], [119], [32].

Hyperthermia can be induced by submitting the patient to EM fields [31]. Fan *et al.* [60] treated 34 patients with OS and FS with a MW antenna array directly *in situ*, while monitoring tissue temperature to keep it above 45 °C. This very rough method was not effective, since an 8% recurrence rate, infections and six deaths were reported [60]. Moreover, and this is the point, this outcome stressed the orthopedic clinical need for an adequate management of the pathological fractures after surgery, such as grafts or the use of bone scaffolds to withstand tissue regeneration [60], [61]. This is one of the main reason which lead to the development novel magnetic biomaterials to be used both as scaffolds for tissue support after curettage, and as heat source for local magnetic induction HT treatment of bone tumor [41], [55].

The rationale, as explained in [70], is to implant the magnetic scaffold with a surgical procedure, the, after the placement in the scraped bone tissue, applying remotely a RF magnetic field through an external coil or a coil-yoke system, the therapeutic heat is generated by the MNPs embedded in the biomaterial is conducted to surrounding tissues, rising the temperature of the tumor region above 43 °C, thus killing residual cancer cells and allowing healthy tissue to grow sustained by the implant [38], [42], [70]. The literature surveys reported in Sect. 3.1 focused mainly on the manufacturing, characterization and proof-of-concept of magnetic scaffolds, but did not use this information to accurately define and model the *in situ* hyperthermia treatment [70]. As final goal of this dissertation work, the use of the knowledge acquired from the morphologic and functional characterization of magnetic scaffolds is exploited to derive an enhanced multiphysic model which can help clinicians to describe the hyperthermia treatment, while defining the sub-optimal set of the operative parameter for the magnetic field (i.e. strength, frequency and waveform).

#### 4.4.2 Geometry

Since the OS and FS affect mainly the epiphysis and diaphysis of long bones [110]- [112], in the reference model [70] a magnetic scaffold implanted in distal femur was investigated. The scaffold was assumed to be spherical, with radius of 5 mm (as in [63], [19]) and surrounded by the surgical fracture gap, i.e. the peri-implant space or the cavity in which new bone is supposed to form [120], [121], the bone tumor region and, finally, bone [70].

The scaffold was assumed to be spherical, with radius of 5 mm (as in [19], [63]) and surrounded by the surgical fracture gap, *i.e.* the peri-implant space or the cavity in which new bone is supposed to form [120], [121], the bone tumor region and, finally, bone [122]. The volume investigated is very narrow ( $\approx 3.14 \text{ cm}^3$ ) and the problem geometry was

simplified considering a circular 2D axial-symmetric system [70], [19].

Moving from this simplified geometry of the problem a goal of this work is to employ the knowledge acquired about the MNPs distribution inside the magnetic scaffolds, together with the AC susceptibility measurements to improve the study and planning of magnetic induction hyperthermia for deep-seated bone tumors. The mathematical framework of Fanti *et al.* is beyond reproach, since highly non-linear phenomena are considered, however, the physiological and physical details need and adjustment.

Under the assumption of a homogeneous and isotropic biological load, with a field penetration complete in the dielectric tissue media, but with no axial electric field inside the coil, and considering the scaffold as the only perturbation of the applied magnetic field [66], the following improvements are suggested, studied and discussed.

Firstly, the muscle, fat and skin are not considered. However, as reported by Bellizzi *et al.* [33], the induced electric field inside the induction system is not negligible at coil edge (where it is maximum), and therefore, if strong magnetic field are used, e.g. up to 30 mT, the power dissipated by dielectric heating in muscle tissue may not be neglected at thousand of kHz. Therefore, to study, investigate and assess if potential risks for the subject exists, a layer of muscle tissue nearby bone is included. As regards the fat and skin layers, it is worth consider this tissues to be negligible at the frequency of interest. This assumption is frequent in the literature and it is supported by experimental findings, causing an error of circa 3 % on the electric field evaluation [123]. Therefore, the magnetic field is no longer considered as homogeneous and therefore the RF coil employed as source for the heat generation should be modeled using the radial and/or axial field expression to represent the actual field distribution inside tissues and scaffold [33], [65], [66], [124].

Secondly, beside considering a 2D axial-symmetric system, since the synthesized magnetic scaffolds are disks of 1.5 mm x 5 mm, and since the scaffold is simulated with respect to its large surface, *i.e.* the circular cross section, a spherical coordinate system was selected [70]. For our purpose, since the volume of tissue affected by the thermal variation is kept equal to few cubic centimeters, the system geometry implemented is shown in Fig.4.11. Therefore, as shown in Fig.4.11, the origin of the  $rz$  axes coincides with the scaffold center and the layered phantom for the simulation was composed of a 0.2 mm fracture gap ( $r_g$ ) [121], a uniform region where the target tumor tissue is present ( $r_t = 0.3 \div 0.5$  mm), then a thick bone-marrow ( $r_b$ ) stratum and hence muscle ( $r_m = 3$  mm). The dimension of the cited tissue layer were taken from the reference man report [125]. The HT treatment of a long bone is investigated.

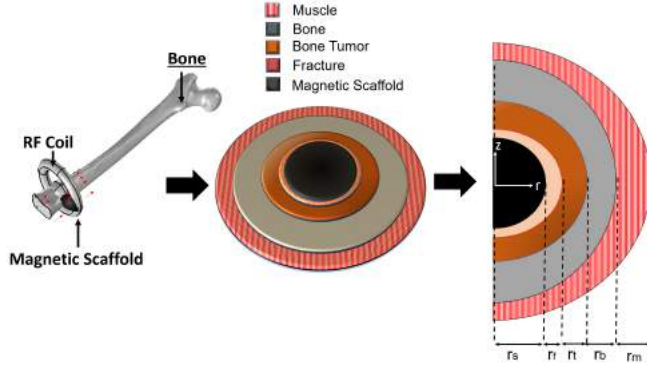


Figure 4.11. Similarly to [70], a 2D-axialsymmetric system was chosen. The axes origin of the cylindrical coordinate system is set in the scaffold center and the layered phantom employed in the simulation was composed of the scaffold, fracture gap ( $r_g$ ), tumor tissue ( $r_t$ ), bone ( $r_b$ ) and muscle ( $r_m$ ).

#### 4.4.3 The Non-Linear Fully Coupled Electromagneto-Thermal Model

The magnetic induction hyperthermia treatment consist of several relevant physic phenomena. The application of an external time-varying magnetic field elicits the  $Fe_3O_4$  nanoparticles in the scaffolds, implying that the flux density is modified and increases at the implant site, and, since the magnetic moment of the MNPs are not able to follow the field dynamic, they dissipate heat according to the Néel mechanism [19], [22], [20], [25], [70], [126]. Meanwhile, the induced electric field (due to Faraday Eq. (2.2)) determines dielectric heat losses in both the scaffold and surrounding tissues. The total EM power, i.e. the sum of the magnetic and dielectric losses, represent a source term in the Heat equation, implying that, moving from an equilibrium condition, the system temperature begins to rise [124]. The temperature inside the scaffold at the magnetic nanoparticles location increases too, determining a variation in their magnetic properties and altering their magnetization dynamic [15], [70], [127]. From the tissue point of view, both the dielectric and thermal properties modifies according to the new temperature field [11], [128]. Therefore, the condition for the EM problem slightly changes and then the Maxwell's Eq.s (2.6) have to be solved again to find the temperature distribution at the given time step, these steps are repeated until the final exposure time is reached. This solution scheme is explained and summarized in Fig. 4.12.

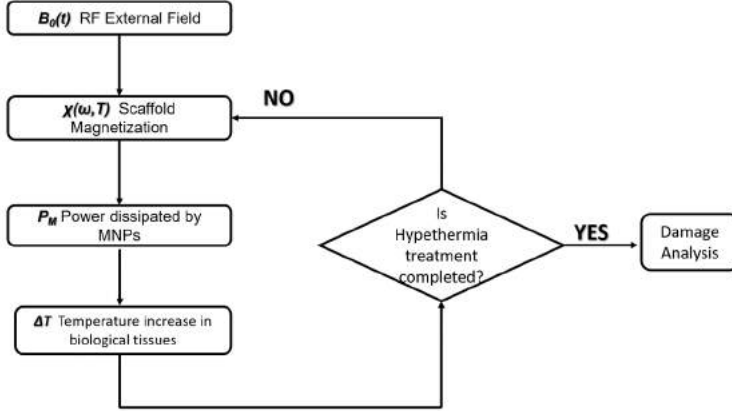


Figure 4.12. Resolution scheme of the Non-Linear Fully Coupled Electromagneto-Thermal Model as found in [70]. This approximation is legitimate by the order-of-magnitude dynamic of the EM and thermal field.

The use of this chopped time-frequency method exploits the different dynamic of the electromagnetic and thermal fields. In fact, the EM field has a characteristic time which is order of magnitude higher than the thermal one (hundreds of ms vs. tenth of ms), thus the assumption of considering the solution to Maxwell's Eq.s as stationary is justified [122].

In detail, the Maxwell's Eq.s (2.6) are solved in the frequency domain via the definition of the magnetic vector potential  $\mathbf{A}$ . Assuming the Cole-Cole model, *i.e.* Eq. (2.32) for the magnetic scaffolds susceptibility, (2.25), considering directly the temperature dependence in the static magnetic susceptibility,  $\chi_0$ , and in the Néel relaxation time expression, via the pre-exponential factor  $\tau_0$  and energy barrier, the magnetic power losses (2.23) for the given time step are computed [70], [19]. Contemporary, the dielectric power is evaluated as [122]:

$$P_{el} = \pi\epsilon_0 f |\mathbf{E}|^2 \epsilon'' = \pi\epsilon_0 f |\mathbf{E}|^2 \frac{\sigma}{j\omega\epsilon_0} \quad (4.30)$$

The total power, according to the Poynting theorem [1], is given by  $P_{el} + P_m = Q_{em}$ . This term is inserted into the Pennes' Bioheat Equation [129], [130]:

$$\rho C_p \frac{\partial T(r,z,t)}{\partial t} = \nabla \cdot (k \nabla T(r,z,t)) + \rho_b C_{p,b} \omega_b (T(r,z,t) - T_a) + Q_{met} + Q_{EM} \quad (4.31)$$

where  $\rho$  is tissue density in  $kg \cdot m^{-3}$ ,  $C_p$  is the specific heat capacity at constant pressure in  $J kg^{-1} K^{-1}$ . The terms in bracket parentheses with the superscript "b" indicates blood

properties, with  $\omega_b$  being the tissue perfusion, which acts as a temperature sink and tends to report the system temperature the arterial temperature ( $T_a$ ), and  $Q_m$  stands for the metabolic heat rate in  $W \cdot m^{-3}$  [129]. The use of this equation is justified if no large vessels are included in the physical system, which is exactly the case investigated in this dissertation work [70], [129] [130]. For all tissue the initial temperature was set to 37°C, except for the inflamed surgical gap which require 35 °C. Eq. (4.31) is subject to an open boundary Neumann's condition at the outer muscle boundary [129]:

$$\mathbf{n} \cdot \frac{\partial T}{\partial r} = 0 \quad (4.32)$$

Moreover, the temperature flux across tissues is obviously considered continuous.

#### 4.4.4 Simulations Overview and Parameters

To solve the Maxwell's Equations (Eq.s (2.6)) in the FD, coupled to the Bio-Heat tranfer equation, according to the resolution scheme presented in Fig. 4.12, the commercial FEM software Comsol Multiphysics (COMSOL inc., Burlington, MA) was used, in particular *Magnetic Fields* and *Heat Transfer Modules*. The EM problem is solved in the frequency domain, whereas the thermal Eq. (4.31) is computed in the time domain.

#### Dielectric Properties

The dielectric properties of the scaffold and tissue are reported in Tab. 4.1 below.

Table 4.1. Electromagnetic properties of scaffold and tissues at 293 kHz. Derived from [70]

	$\epsilon$	$\sigma, S \cdot m^{-1}$	Ref.
$\epsilon$ -PCL	2.20 - j · 0.125	$10^{-4}$	[131], [132]
<b>Fracture gap: Inflamed</b>	3580 - j · 33451	0.545	[133]
<b>Bone Tumor: OS</b>	192 - j · 1313.5	0.196	[134]
<b>Bone</b>	8000 - j · 17186.2	0.280	[9], [10]
<b>Muscle</b>	5300	0.40	[9], [10]

The frequency response of PCL dielectric permittivity was taken from [131], [132]. As regards the fracture gap, it must be remembered to the reader that bone healing process initiate with blood infiltration in the surgical cavity generating the hematoma, which, in turns, causes a local ischemia stage (within the first 7 days), and then results in the inflammatory phase (around 14 days) which elicits bone cells to produce and form the callus [120], [121]. Therefore, as suggested by [133], the fracture dielectric properties can

be assumed to be a volume averaged mixture of the bone and blood ones, depending on the healing stage, or in mathematical terms:

$$\epsilon(\omega, T)_{fracture} = \theta_{bone}\epsilon(\omega, T)_{bone} + \theta_{blood}\epsilon(\omega, T)_{blood} \quad (4.33)$$

where  $\theta_i$  is the volume fraction of blood and bone respectively. Since, from the recent analysis performed by Fanti *et al.* the hyperthermia treatment using magnetic scaffolds increases its efficacy if performed during the inflamed state, in this work only such physiological status is considered [70].

For the bone tumor EM properties the *in vivo* data from mouse fibrosarcoma of Swarup *et al.* are considered assuming a similar behaviour for the osteosarcoma cancer [134]. Finally, as described in Sect. 2.2.1, the properties of healthy tissues were implemented using the four-order Cole-Cole model with the parameters reported in the well-known work of Gabriel and Garbriel [9], [10].

For both healthy and pathologic tissue type, as derived by the excellent review of Rossman and Haemmerich [11], the dielectric properties are assumed to vary linearly with temperature (with a variation of 3 %°C<sup>-1</sup>) [11], [70].

### Thermal Properties

The thermal properties of the scaffold and tissues at the initial temperature of 37 °C are reported in Tab. 4.2 below.

Table 4.2. Thermal properties of scaffold and tissues. Redrafted from [122]

	k (Wm <sup>-1</sup> K <sup>-1</sup> )	C <sub>p</sub> (Jkg <sup>-1</sup> K <sup>-1</sup> )	Q <sub>m</sub> (Wm <sup>-3</sup> )	$\omega_b$
<b>ε-PCL</b>	0.49	1300	n.n.	n.n
<b>Fracture gap: Inflamed</b>	0.558	2450	5262.5	$6.95 \cdot 10^{-3}$
<b>Bone Tumors</b>	0.32	1313	57240	$2.42 \cdot 10^{-3} \div 0.595$
<b>Bone</b>	0.32	1313	286.2	$0.262 \cdot 10^{-3}$
<b>Muscle</b>	0.49	3421	0.91	$1.09 \cdot 10^{-3}$

The PCL properties are taken from [64]. In this work the ex-vivo properties of a mixture of PCL scaffolds plus infiltrated cells is measured for different temperatures (in °C), and the resulting thermal conductivity and heat capacity are [64]:

$$\begin{aligned} k(T)_{PCL} &= -5 \cdot 10^4 \cdot T + 0.5077 \\ C(T)_{p,PCL} &= 0.0232 + 2.5008 \end{aligned} \quad (4.34)$$

For the fracture gap the data of Bhargava *et al.* were employed [?]. Assuming the bone tumor cells homogeneously dispersed in the bone matrix, as can be observed from histological images [110] - [114] and as done in [70], the tumors thermal properties can be considered equal to the bone one, which are taken from the IT'IS Database [135]. The muscle thermal conductivity and heat capacity are derived from [136]. For both healthy and pathologic tissue type, remembering the discussion from Sect. 2.2.1, as demonstrated by Rossman and Haemmerich [11], the thermal conductivity and heat capacity are supposed to linearly vary with temperature according to the following general law:

$$\frac{\Delta\Lambda(T)_i}{\Lambda(T_0)_i} = 1 + \Gamma\Delta T \quad (4.35)$$

Therefore, a coefficient  $\Gamma$  of circa  $0.33\text{ }^{\circ}\text{C}^{-1}$  is used for the heat capacity of the fracture gap, bone, tumors and muscle, whereas a  $0.5\text{ }^{\circ}\text{C}^{-1}$  variation was imposed for the thermal conductivity of all tissues, except for blood, whose  $C_p$  which decreases with a  $0.1\text{ }^{\circ}\text{C}^{-1}$  [70].

As regards the tissue perfusion rate, which acts as a limiting agent in hyperthermia treatment [65], it must be noticed that it varies with tissue type and temperature [137], [138]. Therefore, to include in the simulation of the magnetic induction hyperthermia the effects of the doubling of bone tumor hyperthermia, the curve from [138] were implemented in Comsol using a piecewise function for both healthy and normal tissue.

The damage analysis was performed assuming the integral definition given by Seperato *et al.* and used by Fanti *et al.*. For tumor tissues the lethal temperature threshold was imposed  $42.5\text{ }^{\circ}\text{C}$  for 60 min [31], [70], whilst for bone tissue the necrosis is supposed to occur at  $47\text{ }^{\circ}\text{C}$  after 1 min [139].

Simulations are run varying the OS and FS tumor size from 0.1 mm to 0.5 mm, considering different different magnetic field strength and frequencies, which are chosen as optimum to achieve the complete elimination of cancer cells without allowing restoration. The simulation were run considering a treatment time which varies from 85 min to 120 min. In this realistic scenario, the magnetic induction hyperthermia treatment against deep-seated bone tumors is investigated in order to gain valuable insight in the physics of the oncology procedure, to define a reference scheme for optimization and then allow therapy planning and clinical translation.

# Chapter 5

## Results

### 5.1 Characterization of Magnetic Scaffolds

The first parameter monitored during the manufacturing process of dip-coated magnetic scaffolds, discussed in Sect. 4.2, is the scaffold weight. This quantity cannot be retained reliable, but it can help in understanding if during any of the processing steps problems arise. The plastic sample holders were weighted, then the scaffolds were inserted and a mass measurement was performed to find the weight of the biomaterial by difference. The process was monitored taken measurement for each scaffolds of the sub-groups (A-D samples) after impregnation and sonication (see Sect. 4.2 and Fig. 4.1). If the amount of magnetite entrapped in the scaffold is on the order of magnitude of few mg, with this very simple measurement it is possible to assess if magnetic nanoparticles can be embedded in the biomaterial matrix. The results from the ANOVA test performed between the six scaffolds and the three manufacturing phases are reported in below. It can be noticed that for A samples, *i.e.* the ceramic scaffolds impregnated with the 200 nm ferrofluid, no statistically significant variation was found. However, for the other three samples the weight varied during the process. The most relevant value is obtained for the polymeric samples loaded with 200 nm MNPs.

Table 5.1. Results from the One-Way ANOVA Test on the magnetic scaffolds weight during the impregnation process

	P value	T value
$\beta$ -TCP + 200 nm	0.7985	0.23
$\beta$ -TCP + 50 nm	0.0311	4.41
$\epsilon$ -PCL + 200 nm	$6.54 \cdot 10^{-9}$	85.05
$\epsilon$ -PCL + 50 nm	0.0001	17.65

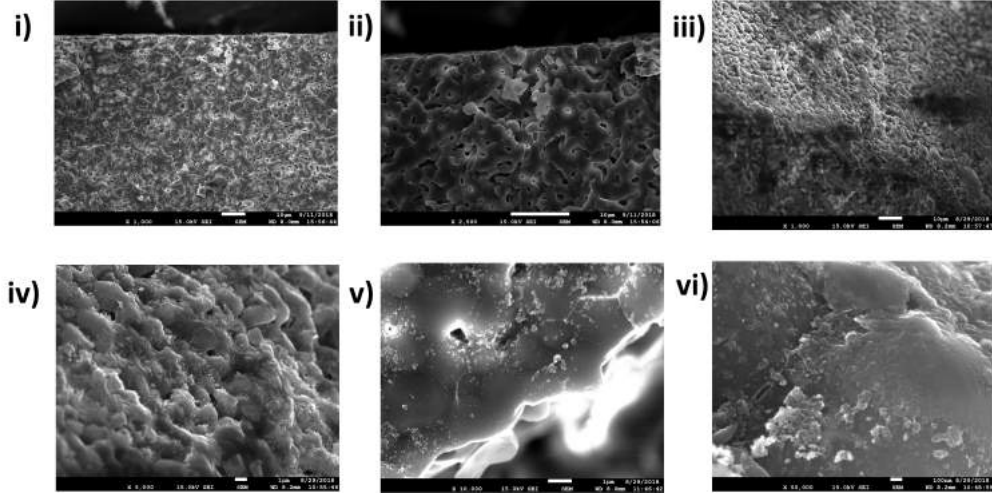


Figure 5.1. SEM images of the TCP ceramic scaffolds. i. Top view of the bare ceramic: it appears compact and present pores of variable dimensions. ii. Zoom of the ceramic surface: the porosity of the biomaterial is evident. iii. Side view of the ceramic scaffold. iv. Ferrofluid impregnated TCP scaffold, magnified five times. v. Magnification of the magnetized scaffold: the different granularity of the MNPs and the embedding matrix is evident. vi. Surface image of 200 nm magnetic nanoparticles on the biomaterial surface.

Despite being very promising, these results should be treated and interpreted carefully. Firstly, the dip-coating process is performed in aqueous medium, which means that huge amount of water are surely entrapped in the pores of the biomaterials. This is obvious since water is the medium which carries nanoparticles to material surface. However, the measurement were performed on the wet samples, hence the statistic analysis, which is affected by several outliers, should be considered as a hint of the synthesis outcomes. Therefore, in the following more accurate qualitative and quantitative methods are employed to assess the validity of the ferrofluid impregnation technique for magnetic scaffolds production.

From the SEM images of the ceramic scaffold sections, in Fig. 5.1, it can be seen that the pore sizes distribution is spread. Analyzing Figures 5.1.i and .ii with ImageJ [74], the pore have a mean diameter of  $1.25\mu\text{m}$  and a standard deviation of  $\pm 0.5 \mu\text{m}$ . The dimension of the pore is orders of magnitude higher than the radius of the nanoparticles. From the acquired images, the nanoparticles dispersed in sample A4 have radii of about  $151.92 \text{ nm} \pm 44.6 \text{ nm}$ , implying that the ferrofluid was a polydispersion. However, it should be reported that this last measurement was difficult since noticeable aggregates of MNPs can be observed. The magnetic phase was observed to be entrapped in the lateral and top surface of the tri-calcium phosphate scaffold. Only isolated and small particles can be

found inside the biomaterial core.

These results allow to infer, in principle, that the ceramic scaffolds are capable of loading MNPs by including them via the action of capillarity forces, as suggested by [38], [42], at least onto their surface. These results are anomalous considering the wide variety of impregnated scaffolds found in literature 3.1. In the following, the amount of magnetite is verified and the results is compared to the morphological evaluation obtained from the SEM.

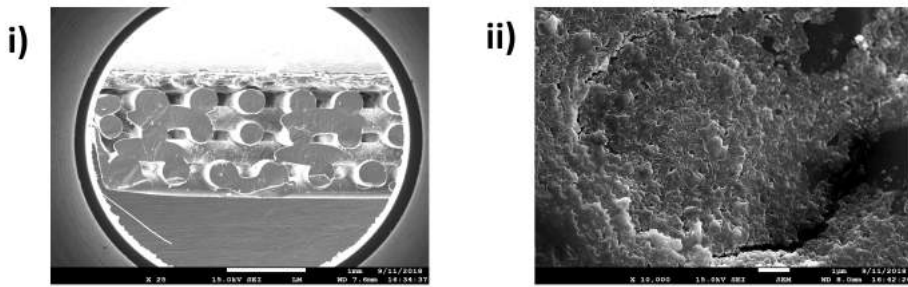


Figure 5.2. SEM images of the  $\epsilon$ -PCL polymeric scaffolds. i. Cross section of the biomaterial interconnected mesh architecture. ii. Inside view of the polymeric scaffold with magnification 10x: a fiber-like structure is observed.

From the SEM images of the PCL scaffold sections, using the measuring tool from ImageJ [74], the diameter of the fiber was estimated to be  $31.8 \mu\text{m} \pm 3.34 \mu\text{m}$ , which agrees with the declared value. The SEM scansion of the scaffolds impregnated with the 200 nm ferrofluid were deeply loaded. To verify if the sample was correctly magnetized, a simple proof was performed sing a NdFeB magnet (0.8 T, 15 kg, 2cm x 2cm): the scaffold did not stick to the magnet, but slowly moving it, the scaffold was able to be attracted for short times (data not shown). Unfortunately, the 50 nm nanoparticles were not seeded correctly in the polymeric matrix. As for the ceramic scaffolds counterpart, the MNPs with smaller molecular size did not fixed in the supporting material.

Regarding the static magnetization measurement, for the  $\beta$ -TCP ceramic scaffolds doped with 50 nm  $Fe_3O_4$  nanoparticles, a very low signal was acquired from the SQUID. In fact, removing the diamagnetic contribution from the ceramic (about  $2.5 \cdot 10^{-3}$  emu in modulus), neglecting the very low hysteresis loop, a saturation magnetization of  $3 \cdot 10^{-3}$  emu is found, as shown in Fig. 5.3. Considering the particle volume and the value of  $92 \text{ emu} \cdot g^{-1}$  for the  $Fe_3O_4$ , a concentration of  $2.7 \mu\text{g}$  of magnetite is derived. The same results holds for the 200 nm samples, but also for the polymeric samples loaded with MNPs of the same molecular size and therefore the data are not shown.

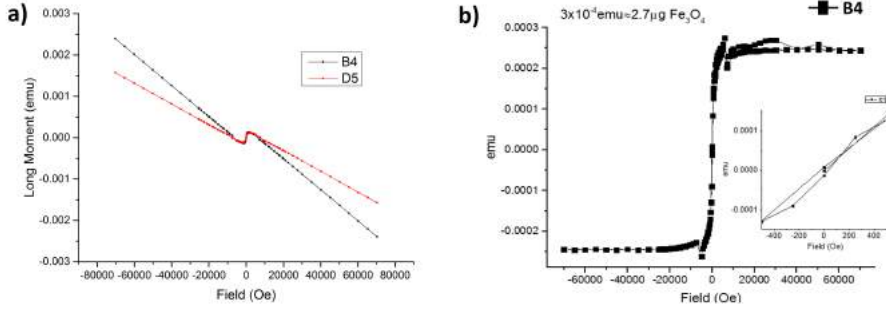


Figure 5.3. Static magnetization measurement of the synthesized magnetic scaffolds. a) Complete magnetic signal (Diamagnetism + Superparamagnetism) for the  $\beta$ -TCP ceramic (B4) and the  $\epsilon$ -PCL polymeric (D5) scaffolds doped with 50 nm  $Fe_3O_4$  nanoparticles. b) The diamagnetic contribute of the ceramic was subtracted to the magnetic signal of the ceramic scaffold. The hysteresis is not significant. From the saturation magnetization a concentration of 2.7  $\mu g$  of  $Fe_3O_4$  is found.

This finding clearly indicates that, even if the SEM/EDS measurement have verified the presence of MNPs onto the surface and sub-surface of the ceramic matrix, the scaffold pore geometry and distribution is not suitable for the ferrofluid impregnation technique [38]. In fact, no ceramic scaffolds was able to load more than 5  $\mu g$  of magnetic phase. Moreover, since the dip-coating process is strictly related to the particle-surface interaction, it is possible to assume that the capillarity and stick force at the  $\beta$ -TCP surface is lower than the electrostatic repulsive force due to the net negative charge of the phosphate-starch coating. However, it should be considered that  $\beta$ -TCP surface is mainly constituted by Ca, P and O, which, as results from molecular dynamic simulations, determines a relatively high effective positive charge due to the  $Ca^{2+}$  atoms exposed in aqueous solution [140]. Therefore, further analysis are required to understand the failure of the dip-coating process on the 3D Bioteck  $\beta$ -TCP disks.

The data presented in Fig.5.3.a allows to infer that also for the polymeric scaffolds impregnated with the ferrofluid of MNPs with  $\varnothing$  25 nm the process failed. Anyway, the aforementioned considerations do not apply in the case of the  $\epsilon$ -PCL. In fact, the polymer has a completely different surface-chemistry [141], which let think that the lack of success is due to the size of the magnetic nanoparticles. To support this claim it is better note that in our case the US power applied to magnetic scaffolds during the sonication step (see Fig.4.1) was 180 W, against the value of 100 W employed in [38], [42], i.e. 0.8 time higher. Said that, given that both Bock *et al.* [38] and Riminucci *et al.* [42] used MNPs with a

radius of 200 nm, provided that the force due to the US exposure is surely higher in our case, the smaller nanoparticles have a much lower weight force which can keep them stick to the surface. Assuming a density of  $4500 \text{ kg}\cdot\text{m}^{-3}$ , for the 50 nm MNPs, the weight force is 0.023 fN, which is two order of magnitude lower than the 200 nm ones, i.e.  $\approx 1.5 \text{ fN}$ . Therefore, pound for the same electrostatic, capillarity and ultrasound force, for the larger  $\text{Fe}_3\text{O}_4$  NPs the weight force is higher, causing, with respect to the 50 nm case, a lower removal of magnetic phase from the scaffold. Therefore, this simple argumentation could explain why the PCL scaffolds impregnated with the ferrofluid of 200 nm were capable of retaining a sufficiently high quantity of MNPs.

## 5.2 Coil Manufacturing: Geometry, Field, RLC Measurements

Using the GA algorithm for the design of a single-layer coil lead to a diameter of 8.9 mm, with 802 winding using a 0.99 mm magnet wire with a pitch equal to 1.09 mm. Despite matching the resistance criterion ( $R_{dc} = 0.479 \Omega$ ) and presenting a 2.34 mH inductance and resonate around tenth of GHz, the coil axial length is 1.67 m, which makes this solution to be impractical.

From the optimization program, assuming a coil diameter ( $D$ ) of 1 cm, a maximum length  $l = 2 \text{ cm}$ , a 287 number of turns for 16 layer with a 18 AWG magnet wire is found. This thick coil  $c = 1.74 \text{ cm}$  satisfies the requirement on the inductance ( $L = 1 \text{ mH}$ ). The total winding length is about 25 m. The geometry is very fit to the sample size and would allow a maximum coupling between the magnetic field flux density and the MNPs in the scaffold. Moreover, considering that the overall capacitance is of the order of 1.92 pF, the resonance is around 7 MHz, which allow to perform the desired AC susceptibility measurement.

Finally, using FEMM v.4.2, the coil designed using the GA code was simulated. The result is presented in Fig. 5.4, where it is shown the norm of the magnetic flux density vector  $\mathbf{B}$  in the  $rz$ -plane when the coil is excited by a 0.1 mA current. It can be observed a uniform field distribution inside the coil, with an average value of  $40.132 \mu\text{T}$  or circa  $32 \text{ A}\cdot\text{m}^{-1}$ . This field strength falls in the range employed for the AC susceptibility measurements [75] - [86] (see Sect. 4.3.1).

By evaluating the ratio between the magnetic flux density within the coil and the current density inside the coil, it is verified that the coil inductance is overestimated with respect to the target one ( $\approx 8.6 \%$ ), as shown in Tab. 5.2. Moreover, the static resistance of the coil windings is below  $1 \Omega$ , which was a requirement specified in Sect. 4.3.1. With these

information, an induced voltage of circa 2.711 mV across the thick coil is found.

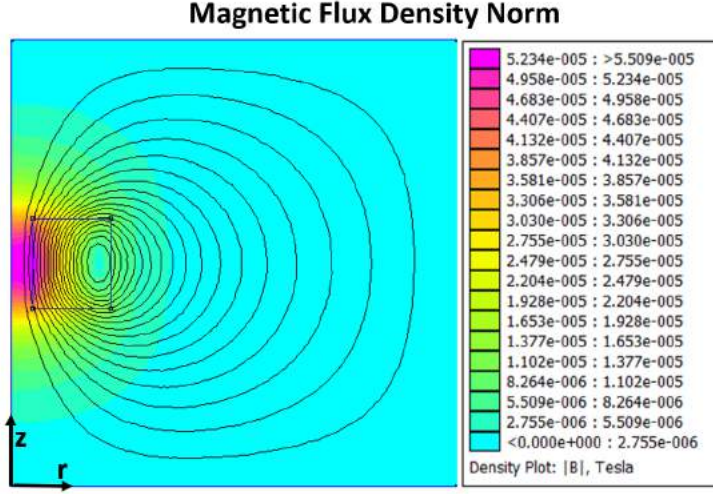


Figure 5.4. 2D distribution of the norm of the magnetic flux density vector  $\mathbf{B}$  for the designed sensing coil fed by a 5 mA.

Considering that the thermal noise ( $V_t$ ) can be defined as [75]:

$$V_t = 2\sqrt{k_B T \Delta f R} \quad (5.1)$$

where  $k_B$  is the Boltzmann constant, i.e.  $1.3806 \cdot 10^{-23} \text{ J K}^{-1}$ ; considering a bandwidth of 1 MHz, for a temperature of 37 °C (to overestimate the noise), with the calculated resistance, a noise voltage of about 0.1  $\mu\text{V}$  is derived. Hence, a relatively high signal-to-noise ratio is expected employing the designed coil for AC susceptibility measurement.

Table 5.2. Results of the designed coil from the FEMM simulation.

Physical quantity	Value
Induced Voltage Drop	2.711 mV
Inductance: Flux/Current	1.086 mH
Resistance: Voltage/Current	0.542 $\Omega$

The designed coils were realized and then characterized using the Agilent 4842A LCR meter (Agilent Technologies, US). The value or resistance, inductance and capacitance for any measurement frequency were used to evaluate the coil impedance,  $Z$ , using Eq. (4.21). The value obtained allow to connect the coils via BNC to the RedPitaya, which have a

dynamic impedance of  $1 \text{ M}\Omega$  in input [104], [105]. Then, since, recalling the discussion from Sect. 4.3.1, the Q-factor is an important parameter for the measurement performance, it has been evaluated using Eq. (4.22) with the real data and compared to the one estimated one exploiting Eq. (4.20). Results are shown in Fig. 5.5. A maximum value of 58 is found, which permits to define the designed coil as an high-quality one. Moreover, despite the previous approximate evaluation from the analytic values of  $L$  and  $C$ , the resonant frequency of the coil is around 700 kHz, which limits the bandwidth of our measurements. This can be seen as a limitation, but, with respect to the literature surveys presented in Sect. 3.1, in particular Table 3.2, the value of 700 kHz is used only in a very special case and the frequencies employed to perform hyperthermia treatment using magnetic scaffolds are very lower.

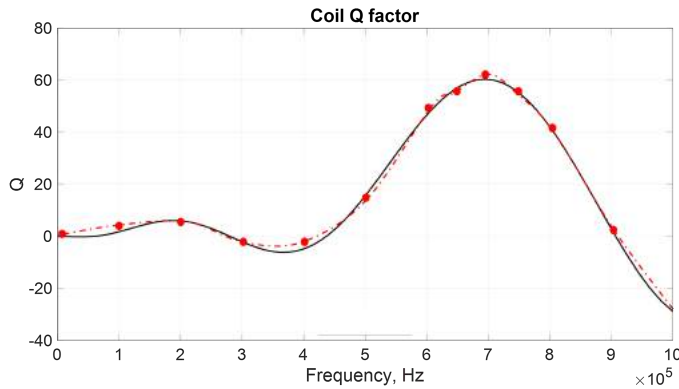


Figure 5.5. Comparison between the Q factor evaluated using Eq. (4.22) and the measured one for the designed thick sensing coil.

### 5.3 Magnetic Scaffolds AC Susceptibility Spectra

The polymeric and ceramic scaffolds doped with the 50 nm MNPs, as demonstrated by the qualitative SEM results and the quantitative SQUID tests, are filled with a small concentration of ferrite. Therefore, with the setup described in Sect. ref, when trying to evaluate their SAR when exposed to a power of 0.1 W of 500 kHz, 1 MHz and even 2.45 GHz for 5 min, no significant temperature increase was observed, as reported in the Fig. 5.6 below.

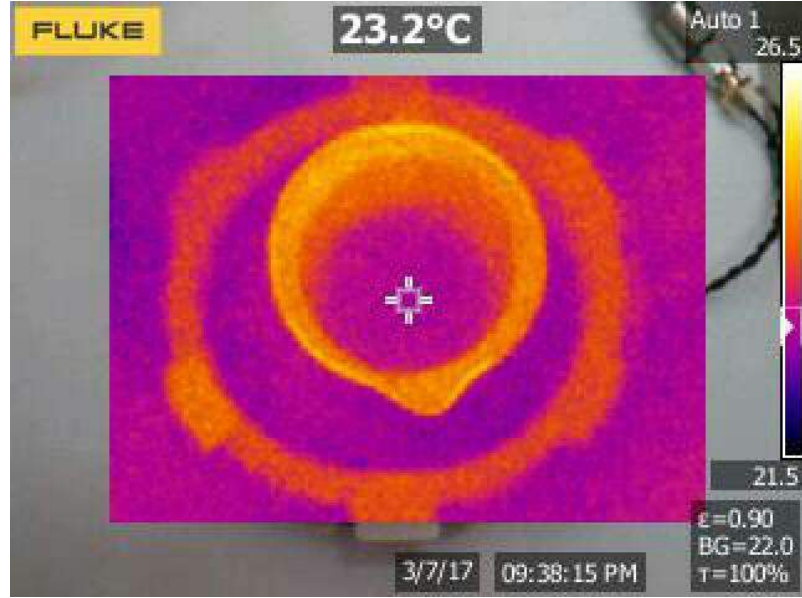


Figure 5.6. Thermographic image acquired with the Fulke TiS45 thermocamera. The magnetic scaffold, which is immersed in deionized water, is exposed to the magnetic field produced by the coil.

## 5.4 Simulations of the Hyperthermia Treatment on Deep Seated Bone Tumors

Moving from the non-linear electromagnetic and thermal model of Fanti *et al.*, the influence of temperature on the AC susceptibility of magnetic scaffolds was assessed evaluating the relaxation times Eq. (2.26) and (2.27) together with the equilibrium and complex susceptibilities via Eq. (2.15) and (2.32).

It can be noticed from Fig. 5.7.a that in the temperature range of hyperthermia and ablation treatment, *i.e.* from 35 °C to 60 °C, the pre-exponential factor  $\tau_0$  has a linear trend, whereas the Néel characteristic time  $\tau_N$  has a rather hyperbolic behavior. It should be remembered that the Brownian relaxation, depicted in Fig. 2.6, does not occurs or can be neglected in MNPs embedded in systems such as magnetic scaffolds [19], [26], [70].

The initial susceptibility of the magnetic scaffolds with MNPs of 50 nm and  $\phi=0.9\%$  can be estimated to decrease linearly in the temperature range of interest, as shown in Fig. 5.7.b. On the other hand, including the non-linearity of  $\tau_0$  and  $\tau_N$ , it can be noticed that the imaginary part of the material slowly increases, varying of about 1.5 %. The variation may appear to be negligible, but the matching conditions during hyperthermia

treatment and the estimation of the exposure time must be accurate in order to avoid hurting the patient [65]. Of course, the modulus of the susceptibility increases as the content of magnetic nanoparticles increases. However, from the formula this trend is supposed to be linear, but, as already discussed in Sect. 2.2.2, non-linear phenomena due to particle-particle interaction would present in ferrofluid impregnated magnetic scaffolds.

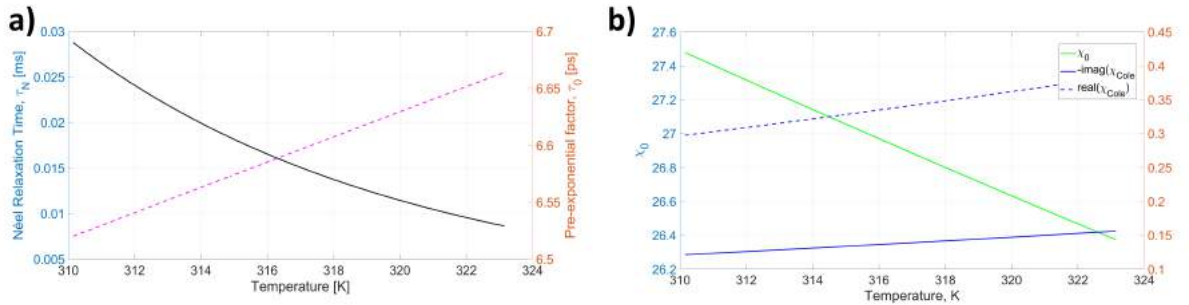


Figure 5.7. MNPs of 50 nm with  $\phi=0.9\%$ : a. Temperature dependence of pre-exponential factor  $\tau_0$  and Néel characteristic time  $\tau_N$ . b. Initial susceptibility  $\chi_0$  and complex susceptibility  $\chi(\omega)$  in its real and imaginary part.

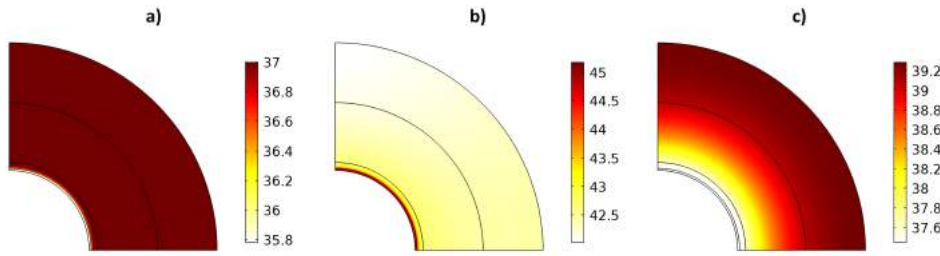


Figure 5.8. Spatio-temporal evolution of the temperature field within the tissues: a) Initial time: the thermal gradient at  $t=0$  is due to the different initial temperature of the inflamed fracture gap. b) Temperature pattern at  $t = 60$  min. The heating is homogeneous and radial, causing the OS tumor to reach  $43^\circ\text{C}$ . c) Final time 100 min. The field is turned off and the system cool down.

From the FEM simulation run in COMSOL, the spatio-temporal evolution of the temperature presents as homogeneous in Fig. 5.8 and qualitatively similar for all the cases analyzed. Therefore, in the following, as done in [70], relevant attention is paid to the average temperature in the tumor tissue and in the quantification of damaged and necrotic tissues.

As regards the Osteosarcoma, evaluating the surface average of  $T(\mathbf{r},t)$  in the tumor

region, presented in Fig. 5.9.a, it can be noticed that, for a 40 mT and 409 kHz field [70], [50], the temperature increases follow the dynamic of the external field, whose envelope is modeled as a rectangular port signal. From Fig. 5.9.a it is possible to infer that the smaller the tumor, the higher is the maximum temperature rise, and then, coherently with the definition of integral damage [70], the fraction of tumor tissue exposed to the lethal temperature for the damage time of 60 min augments as the volume of tumor to treat decrease. As noticed by Fanti *et al.*, the case of a 0.5 mm OS is a very critical one since, even for very high strength magnetic field and noticeable frequencies (which violate the so-called safety product  $f \cdot H$  [16]) only about the 38 % of tumor cells can be damaged. A reader with a biomedical background should address the possible problem of inflammation due to the necrosis, which would act as a disturbing event in the tissue healing after the therapy. The *in vivo* necrosis due to hyperthermia treatment potentially can produce inflammation, but only histological analysis can resolve the matter, as demonstrated in [?], where, even with a marked necrotic core, the treated tissue did not present any sign of inflammation.

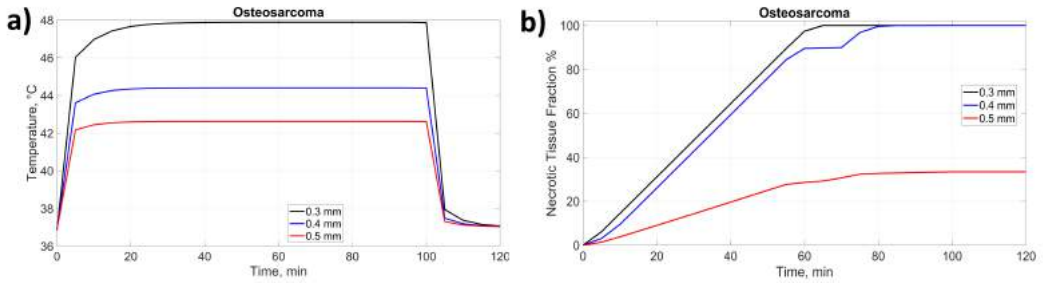


Figure 5.9. a. Average temperature in the OS. The temporal envelope reflects the external field one. b. Percentage of necrotic tissue in the tumor region. The two information are complementary and demonstrate that highly perfused tumors can be treated with a constant power for a time sufficient to kill the residual cancer cells.

# Chapter 6

## Conclusions

This dissertation works faced the description of the manufacturing, the morphological characterization and functional description of a novel class of therapeutic magnetic biomaterials.

Relying on electromagnetism fundamentals, exploiting and trying to improve the established belief system about the magnetization dynamic of magnetic nanoparticles ensembles, the available literature sources on novel magnetic biomaterials are critically analyzed in order to identify a suitable, fast, reliable and cost/effective method for the synthesis of magnetic scaffolds. Among all, the ferrofluid impregnation or dip-coating was chosen. Magnetic scaffolds of  $\beta$ -TCP and  $\epsilon$ -PCL were functionalized using 50 nm and 200 nm ferrite nanoparticles. The magnetic composite biomaterials were characterized from a morphological point of view via SEM/EDS imaging. Furthermore, a simple, room-temperature AC susceptometer was designed in order to measure the frequency response of the manufactured magnetic scaffolds. By quantifying the magnetic susceptibility spectra, and also measuring the SAR of magnetic scaffolds with IR thermography, valuable and significant information regarding the level of interactions of particles in the system, as well as deep insight about the heat dissipation of magnetic scaffolds is derived. Finally, since one potential application of these magnetic scaffolds is their use as *in situ* source of therapeutic heat to perform hyperthermia treatment against deep seated tumors, especially bone tumors, the knowledge and information gained from the morphological and functional features and properties of magnetic scaffolds were employed to simulate the magnetic hyperthermia treatment via a non-linear fully coupled electromagnetic-thermal model.

This dissertation work aims to start bridging the gap between the research ambitions and clinical needs related to magnetic scaffolds for hyperthermia. The scope of this text is to

retrieve the most important features for accurately describing the hyperthermia treatment, while ensuring an experimental and quantitative basis to allow the initial clinical translation of these powerful theranostic biomaterials.

# List of figures

2.1	Cole-Cole model for blood, bone and muscle tissues from DC to 1 MHz [10]. The real part of dielectric permittivities and tissue conductivities are presented in logarithmic scales. . . . .	7
2.2	Schematic representation of: a) Paramagnetic materials: magnetic dipoles align according to the direction of the external $\mathbf{B}$ field. b) Anti-ferromagnetic materials. c) Ferrimagnetic materials. Redrafted from [12]. . . . .	9
2.3	Temperature dependence of the magnetization for a generic ferromagnetic material. Redrafted from [12]. . . . .	11
2.4	Particle size influence on magnetic response of materials. Redrafted from [16]. . .	12
2.5	Thermal barrier mechanism of superparamagnetic nanoparticles below and above the blocking temperature. Redrafted from [16]. . . . .	12
2.6	Figure representing the two relaxation mechanisms typical of a ferrofluid. . . . .	16
2.7	Example of the Debye frequency response for a water-based ferrofluid of 4 nm ferrite nanoparticles, with $\tau_N = 1 \text{ ms}$ and $\tau_B = 10 \mu\text{s}$ . The different relaxation time influence the resonant frequency. . . . .	17
4.1	Dip-coated magnetic scaffolds: (i) Dilute the ferrofluid up to the desired concentration. In our case $12.5 \text{ mg} \cdot \text{ml}^{-1}$ is used. (ii) Soak the ceramic or polymeric scaffold into the ferrofluid and let capillarity act for 30 min. (iii) Extract the impregnated scaffold and freeze-drying the sample at $^{\circ}\text{C}$ for 24 h. (iv) Thaw the sample up to room temperature. (v) Perform the washout of the MNPs which did not impregnated scaffold using ultrasound at 180 W for 30 min. (vi) Repeat the freeze-drying step. Finally, defrost the magnetized scaffold (vii), then rinse and use (viii). . . . .	30
4.2	Generic AC bridge circuit for inductance measurements. . . . .	34

4.3	The AC Susceptometer designed by Das et al. [86]. The sensing coils are supplied with an identical current, adjusted by a software routine, the voltage across them is converted in RMS to evaluate the complex magnetic susceptibility of the sample under test. . . . .	36
4.4	Cross-section of a coil. The coordinate system is cylindrical (rz-plane) and it is set in the coil center. The copper wire diameter is $d$ , $D$ indicates the coil inner diameter, whereas $D_e$ is the external diameter. The symbol $a$ is the mean radius of the turns. Finally, $c$ is winding thickness and $l$ is the coil length. . . . .	39
4.5	RLC circuital lumped parameter representation of an unshielded coil: a) simplest model, b) high frequency equivalent circuit of a single-layer solenoid air-core inductors. Redrafted from [91]. . . . .	41
4.6	Physic-based model of the single-cell used for the evaluation of stray capacitance in multi-turn coil. The main path considered for the electric field line is highlighted in yellow. Redrafted from [91]. . . . .	42
4.7	Meta-heuristic Genetic Algorithm (GA) for the optimal design of a coil with desired inductance and first-resonant frequency. . . . .	46
4.8	Current mirror: it is implemented using two identical transistors, working in saturation regime, polarized by the same gate-source voltage, which determines an output current equal to the reference one. Redrafted from [103]. . . . .	48
4.9	Scheme of the designed AC Susceptometer for measuring the magnetic susceptibility of the synthesized ferrofluid-impregnated scaffolds. A sinusoidal voltage at a given frequency is driven to the Infineon BCV61CE6327HTSA1 current mirror, then, the two equal currents feeds the designed pick-up coils. The difference between the induced voltages across the coils is acquired and digitalized by the RedPitaya acquisition board (14 bit, sampling rate of 120 MHz), and, finally, processed using a Matlab routine. This measurement system allows to derive the real and imaginary part of the magnetic susceptibility of the sample. . . . .	49
4.10	Schematic representation of the thermographic measurement for the evaluation of the heat losses due to the RF-exposure of magnetic scaffolds. . . . .	51
4.11	Similarly to [70], a 2D-axialsymmetric system was chosen. The axes origin of the cylindrical coordinate system is set in the scaffold center and the layered phantom employed in the simulation was composed of the scaffold, fracture gap ( $r_g$ ), tumor tissue ( $r_t$ ), bone ( $r_b$ ) and muscle ( $r_m$ ). . . . .	55

4.12 Resolution scheme of the Non-Linear Fully Coupled Electromagneto-Thermal Model as found in [70]. This approximation is legitimate by the order-of-magnitude dynamic of the EM and thermal field. . . . .	56
5.1 SEM images of the TCP ceramic scaffolds. i. Top view of the bare ceramic: it appears compact and present pores of variable dimensions. ii. Zoom of the ceramic surface: the porosity of the biomaterial is evident. iii. Side view of the ceramic scaffold. iv. Ferrofluid impregnated TCP scaffold, magnified five times. v. Magnification of the magnetized scaffold: the different granularity of the MNPs and the embedding matrix is evident. vi. Surface image of 200 nm magnetic nanoparticles on the biomaterial surface. . . . .	62
5.2 SEM images of the $\epsilon$ -PCL polymeric scaffolds. i. Cross section of the biomaterial interconnected mesh architecture. ii. Inside view of the polymeric scaffold with magnification 10x: a fiber-like structure is observed. . . . .	62
5.3 Static magnetization measurement of the synthesized magnetic scaffolds. a) Complete magnetic signal (Diamagnetism + Superparamagnetism) for the $\beta$ -TCP ceramic (B4) and the $\epsilon$ -PCL polymeric (D5) scaffolds doped with 50 nm $Fe_3O_4$ nanoparticles. b) The diamagnetic contribute of the ceramic was subtracted to the magnetic signal of the ceramic scaffold. The hysteresis is not significant. From the saturation magnetization a concentration of 2.7 $\mu g$ of $Fe_3O_4$ is found. . . . .	63
5.4 2D distribution of the norm of the magnetic flux density vector $\mathbf{B}$ for the designed sensing coil fed by a 5 mA. . . . .	65
5.5 Comparison between the Q factor evaluated using Eq. (4.22) and the measured one for the designed thick sensing coil. . . . .	67
5.6 Thermographic image acquired with the Fulke TiS45 thermocamera. The magnetic scaffold, which is immersed in deionized water, is exposed to the magnetic field produced by the coil. . . . .	68
5.7 MNPs of 50 nm with $\phi=0.9\%$ : a. Temperature dependence of pre-exponential factor $\tau_0$ and Néel characteristic time $\tau_N$ . b. Initial susceptibility $\chi_0$ and complex susceptibility $\chi(\omega)$ in its real and imaginary part. . . . .	69
5.8 Spatio-temporal evolution of the temperature field within the tissues: a) Initial time: the thermal gradient at $t=0$ is due to the different initial temperature of the inflamed fracture gap. b) Temperature pattern at $t = 60$ min. The heating is homogeneous and radial, causing the OS tumor to reach 43 °C. c) Final time 100 min. The field is turned off and the system cool down. . . . .	69

- 5.9 a. Average temperature in the OS. The temporal envelope reflects the external field  
one. b. Percentage of necrotic tissue in the tumor region. The two information are  
complementary and demonstrate that highly perfused tumors can be treated with  
a constant power for a time sufficient to kill the residual cancer cells. . . . . 70

# List of tables

3.1	Magnetic scaffolds divided by composition, production and MNPs embedded	25
3.2	Magnetic scaffolds manufactured for hyperthermia treatment. . . . .	27
4.1	Electromagnetic properties of scaffold and tissues at 293 kHz. Derived from [70] . . . . .	57
4.2	Thermal properties of scaffold and tissues. Redrafted from [122] . . . . .	58
5.1	Results from the One-Way ANOVA Test on the magnetic scaffolds weight during the impregnation process . . . . .	60
5.2	Results of the designed coil from the FEMM simulation. . . . .	66

# Bibliography

- [1] J. D. Jackson, *Classical electrodynamics*. John Wiley & Sons, 2012.
- [2] G. Franceschetti, *Electromagnetics: theory, techniques, and engineering paradigms*. Springer Science & Business Media, 2013.
- [3] R. Plonsey, “Bioelectric phenomena,” *Wiley Encyclopedia of Electrical and Electronics Engineering*, 2001.
- [4] P. S. Neelakanta, *Handbook of electromagnetic materials: monolithic and composite versions and their applications*. CRC press, 1995.
- [5] A. H. Sihvola, *Electromagnetic mixing formulas and applications*. Iet, 1999, no. 47.
- [6] J. Behari, *Biophysical bone behaviour: Principles and applications*. John Wiley & Sons, 2009.
- [7] R. Hernandez and A. V. Popov, “Molecular dynamics out of equilibrium: mechanics and measurables,” *Wiley Interdisciplinary Reviews: Computational Molecular Science*, vol. 4, no. 6, pp. 541–561, 2014.
- [8] G. Lamoureux and B. Roux, “Modeling induced polarization with classical drude oscillators: Theory and molecular dynamics simulation algorithm,” *The Journal of chemical physics*, vol. 119, no. 6, pp. 3025–3039, 2003.
- [9] S. Gabriel, R. Lau, and C. Gabriel, “The dielectric properties of biological tissues: Ii. measurements in the frequency range 10 hz to 20 ghz,” *Physics in medicine & biology*, vol. 41, no. 11, p. 2251, 1996.
- [10] ——, “The dielectric properties of biological tissues: Iii. parametric models for the dielectric spectrum of tissues,” *Physics in Medicine & Biology*, vol. 41, no. 11, p. 2271, 1996.
- [11] C. Rossmann and D. Haemmerich, “Review of temperature dependence of thermal properties, dielectric properties, and perfusion of biological tissues at hyperthermic and ablation temperatures,” *Critical Reviews™ in Biomedical Engineering*, vol. 42, no. 6, 2014.

- [12] F. Barnes and B. Greenebaum, “Handbook of biological effects of electromagnetic fields. bioengineering and biophysical aspects of electromagnetic fields, ; crc,” *CRC/Taylor & Francis*, pp. 115–152, 2007.
- [13] E. Della Torre, *Magnetic hysteresis*. Wiley, 2000.
- [14] Y. Gao, K. Muramatsu, A. Kushibe, K. Yamazaki, A. Chiba, and T. Yamamoto, “Reduction of artifact of metallic implant in magnetic resonance imaging by combining paramagnetic and diamagnetic materials,” *Journal of Applied Physics*, vol. 107, no. 9, p. 09B323, 2010.
- [15] D. L. Leslie-Pelecky and R. D. Rieke, “Magnetic properties of nanostructured materials,” *Chemistry of materials*, vol. 8, no. 8, pp. 1770–1783, 1996.
- [16] Q. A. Pankhurst, J. Connolly, S. Jones, and J. Dobson, “Applications of magnetic nanoparticles in biomedicine,” *Journal of physics D: Applied physics*, vol. 36, no. 13, p. R167, 2003.
- [17] C. Bean and u. D. Livingston, “Superparamagnetism,” *Journal of Applied Physics*, vol. 30, no. 4, pp. S120–S129, 1959.
- [18] F. G. Aliev, M. A. Correa-Duarte, A. Mamedov, J. W. Ostrander, M. Giersig, L. M. Liz-Marzán, and N. A. Kotov, “Layer-by-layer assembly of core-shell magnetite nanoparticles: Effect of silica coating on interparticle interactions and magnetic properties,” *Advanced materials*, vol. 11, no. 12, pp. 1006–1010, 1999.
- [19] A. Fanti, M. B. Lodi, and G. Mazzarella, “Enhancement of cell migration rate toward a superparamagnetic scaffold using lf magnetic fields,” *IEEE Transactions on Magnetics*, vol. 52, no. 10, pp. 1–8, 2016.
- [20] R. E. Rosensweig, “Heating magnetic fluid with alternating magnetic field,” *Journal of magnetism and magnetic materials*, vol. 252, pp. 370–374, 2002.
- [21] J. Dormann, L. Bessais, and D. Fiorani, “A dynamic study of small interacting particles: superparamagnetic model and spin-glass laws,” *Journal of Physics C: Solid State Physics*, vol. 21, no. 10, p. 2015, 1988.
- [22] D. B. Reeves and J. B. Weaver, “Approaches for modeling magnetic nanoparticle dynamics,” *Critical Reviews™ in Biomedical Engineering*, vol. 42, no. 1, 2014.
- [23] P. Debye and F. Bueche, “Electric moments of polar polymers in relation to their structure,” *The Journal of Chemical Physics*, vol. 19, no. 5, pp. 589–594, 1951.
- [24] S. Laurent, D. Forge, M. Port, A. Roch, C. Robic, L. Vander Elst, and R. N. Muller, “Magnetic iron oxide nanoparticles: synthesis, stabilization, vectorization, physicochemical characterizations, and biological applications,” *Chemical reviews*, vol. 108, no. 6, pp. 2064–2110, 2008.

- [25] R. Hergt, R. Hiergeist, M. Zeisberger, G. Glöckl, W. Weitschies, L. Ramirez, I. Hilger, Kaiser, and WA, “Enhancement of ac-losses of magnetic nanoparticles for heating applications,” *Journal of Magnetism and Magnetic Materials*, vol. 280, no. 2-3, pp. 358–368, 2004.
- [26] G. T. Landi, F. R. Arantes, D. R. Cornejo, A. F. Bakuzis, I. Andreu, and E. Natividad, “Ac susceptibility as a tool to probe the dipolar interaction in magnetic nanoparticles,” *Journal of Magnetism and Magnetic Materials*, vol. 421, pp. 138–151, 2017.
- [27] S. van Berkum, J. T. Dee, A. P. Philipse, and B. H. Erné, “frequency-dependent magnetic susceptibility of magnetite and cobalt ferrite nanoparticles embedded in paa hydrogel,” *International journal of molecular sciences*, vol. 14, no. 5, pp. 10 162–10 177, 2013.
- [28] V. Pillai, P. Kumar, M. Hou, P. Ayyub, and D. Shah, “Preparation of nanoparticles of silver halides, superconductors and magnetic materials using water-in-oil microemulsions as nano-reactors,” *Advances in Colloid and Interface Science*, vol. 55, pp. 241–269, 1995.
- [29] A. Grillone, E. R. Riva, A. Mondini, C. Forte, L. Calucci, C. Innocenti, C. de Julian Fernandez, V. Cappello, M. Gemmi, S. Moscato *et al.*, “Active targeting of sorafenib: Preparation, characterization, and in vitro testing of drug-loaded magnetic solid lipid nanoparticles,” *Advanced healthcare materials*, vol. 4, no. 11, pp. 1681–1690, 2015.
- [30] Z. Liu, F. Miao, W. Hua, and F. Zhao, “Fe<sub>3</sub>O<sub>4</sub> nanoparticles: Microwave-assisted synthesis and mechanism,” *Materials Letters*, vol. 67, no. 1, pp. 358–361, 2012.
- [31] B. Hildebrandt, P. Wust, O. Ahlers, A. Dieing, G. Sreenivasa, T. Kerner, R. Felix, and H. Riess, “The cellular and molecular basis of hyperthermia,” *Critical reviews in oncology/hematology*, vol. 43, no. 1, pp. 33–56, 2002.
- [32] I. Hilger, *Smart Nanoparticles and the Effects in Magnetic Hyperthermia In Vivo*. CRC Press, 2018.
- [33] G. Bellizzi and O. M. Bucci, “On the optimal choice of the exposure conditions and the nanoparticle features in magnetic nanoparticle hyperthermia,” *International Journal of Hyperthermia*, vol. 26, no. 4, pp. 389–403, 2010.
- [34] L. Moroni, J. Schrooten, R. Truckenmüller, J. Rouwkema, J. Sohier, and C. A. van Blitterswijk, “Chapter 1 - tissue engineering: An introduction,” in *Tissue Engineering (Second Edition)*, second edition ed., C. A. V. Blitterswijk and J. D. Boer, Eds. Oxford: Academic Press, 2014, pp. 1 – 21. [Online]. Available: <http://www.sciencedirect.com/science/article/pii/B9780124201453000018>

- [35] A. Lindahl, M. Brittberg, D. Gibbs, J. I. Dawson, J. Kanczler, C. Black, R. Tare, and R. O. Oreffo, “Chapter 16 - cartilage and bone regeneration,” in *Tissue Engineering (Second Edition)*, second edition ed., C. A. V. Blitterswijk and J. D. Boer, Eds. Oxford: Academic Press, 2015, pp. 529 – 582. [Online]. Available: <http://www.sciencedirect.com/science/article/pii/B978012420145300016X>
- [36] J. Joly, J. Vanlauwe, D. V. Assche, I. Reischl, and F. P. Luyten, “Chapter 22 - clinical translation,” in *Tissue Engineering (Second Edition)*, second edition ed., C. A. V. Blitterswijk and J. D. Boer, Eds. Oxford: Academic Press, 2014, pp. 783 – 807. [Online]. Available: <http://www.sciencedirect.com/science/article/pii/B9780124201453000225>
- [37] R. A. Perez, S.-J. Seo, J.-E. Won, E.-J. Lee, J.-H. Jang, J. C. Knowles, and H.-W. Kim, “Therapeutically relevant aspects in bone repair and regeneration,” *Materials Today*, vol. 18, no. 10, pp. 573–589, 2015.
- [38] N. Bock, A. Riminucci, C. Dionigi, A. Russo, A. Tampieri, S. Nanoparticles, E. the Effects in Magnetic Hyperthermia In Vivo, V. A. Goranov, M. Marcacci, and V. Dediu, “A novel route in bone tissue engineering: magnetic biomimetic scaffolds,” *Acta Biomaterialia*, vol. 6, no. 3, pp. 786–796, 2010.
- [39] A. D. Grief and G. Richardson, “Mathematical modelling of magnetically targeted drug delivery,” *Journal of Magnetism and Magnetic Materials*, vol. 293, no. 1, pp. 455–463, 2005.
- [40] S. Panzeri, A. Russo, M. Sartori, G. Giavaresi, M. Sandri, M. Fini, M. Maltarello, T. Shelyakova, A. Ortolani, A. Visani *et al.*, “Modifying bone scaffold architecture in vivo with permanent magnets to facilitate fixation of magnetic scaffolds,” *Bone*, vol. 56, no. 2, pp. 432–439, 2013.
- [41] M. Bañobre-López, Y. Pineiro-Redondo, M. Sandri, A. Tampieri, R. De Santis, V. A. Dediu, and J. Rivas, “Hyperthermia induced in magnetic scaffolds for bone tissue engineering,” *IEEE Transactions on Magnetics*, vol. 50, no. 11, pp. 1–7, 2014.
- [42] A. Riminucci, C. Dionigi, C. Pernechele, G. De Pasquale, T. De Caro, G. M. Ingo, F. Mezzadri, N. Bock, M. Solzi, G. Padeletti *et al.*, “Magnetic and morphological properties of ferrofluid-impregnated hydroxyapatite/collagen scaffolds,” *Science of Advanced Materials*, vol. 6, no. 12, pp. 2679–2687, 2014.
- [43] A. Tampieri, E. Landi, F. Valentini, M. Sandri, T. D'alessandro, V. Dediu, and M. Marcacci, “A conceptually new type of bio-hybrid scaffold for bone regeneration,” *Nanotechnology*, vol. 22, no. 1, p. 015104, 2010.
- [44] J. Meng, B. Xiao, Y. Zhang, J. Liu, H. Xue, J. Lei, H. Kong, Y. Huang, Z. Jin, N. Gu

- et al.*, “Super-paramagnetic responsive nanofibrous scaffolds under static magnetic field enhance osteogenesis for bone repair *in vivo*,” *Scientific reports*, vol. 3, p. 2655, 2013.
- [45] X. B. Zeng, H. Hu, L. Q. Xie, F. Lan, W. Jiang, Y. Wu, and Z. W. Gu, “Magnetic responsive hydroxyapatite composite scaffolds construction for bone defect reparation,” *International journal of nanomedicine*, vol. 7, p. 3365, 2012.
- [46] K. Lai, W. Jiang, J. Z. Tang, Y. Wu, B. He, G. Wang, and Z. Gu, “Superparamagnetic nano-composite scaffolds for promoting bone cell proliferation and defect reparation without a magnetic field,” *RSC Advances*, vol. 2, no. 33, pp. 13 007–13 017, 2012.
- [47] S. K. Samal, V. Goranov, M. Dash, A. Russo, T. Shelyakova, P. Graziosi, L. Lungaro, A. Riminiucci, M. Uhlarz, M. Ban~obre-Lo’pez *et al.*, “Multilayered magnetic gelatin membrane scaffolds,” *ACS applied materials & interfaces*, vol. 7, no. 41, pp. 23 098–23 109, 2015.
- [48] M. Harabech, N. R. Kiselovs, W. Maenhoudt, G. Crevecoeur, D. Van Roost, and L. Dupré, “Experimental ex-vivo validation of pmma-based bone cements loaded with magnetic nanoparticles enabling hyperthermia of metastatic bone tumors,” *AIP advances*, vol. 7, no. 5, p. 056704, 2017.
- [49] A. Tampieri, T. D’Alessandro, M. Sandri, S. Sprio, E. Landi, L. Bertinetti, S. Panseri, G. Pepponi, J. Goettlicher, M. Bañobre-López *et al.*, “Intrinsic magnetism and hyperthermia in bioactive fe-doped hydroxyapatite,” *Acta biomaterialia*, vol. 8, no. 2, pp. 843–851, 2012.
- [50] A. Farzin, M. Fathi, and R. Emadi, “Multifunctional magnetic nanostructured hardystonite scaffold for hyperthermia, drug delivery and tissue engineering applications,” *Materials Science and Engineering: C*, vol. 70, pp. 21–31, 2017.
- [51] I. A. Paun, R. C. Popescu, B. S. Calin, C. C. Mustaciosu, M. Dinescu, and C. R. Luculescu, “3d biomimetic magnetic structures for static magnetic field stimulation of osteogenesis,” *International journal of molecular sciences*, vol. 19, no. 2, p. 495, 2018.
- [52] U. D’Amora, T. Russo, A. Gloria, V. Rivieccio, V. D’Antò, G. Negri, L. Ambrosio, and R. De Santis, “3d additive-manufactured nanocomposite magnetic scaffolds: Effect of the application mode of a time-dependent magnetic field on hmscs behavior,” *Bioactive materials*, vol. 2, no. 3, pp. 138–145, 2017.
- [53] Y. Zhang, D. Zhai, M. Xu, Q. Yao, J. Chang, and C. Wu, “3d-printed bioceramic scaffolds with a fe 3 o 4/graphene oxide nanocomposite interface for hyperthermia therapy of bone tumor cells,” *Journal of Materials Chemistry B*, vol. 4, no. 17, pp.

- 2874–2886, 2016.
- [54] Y. Wei, X. Zhang, Y. Song, B. Han, X. Hu, X. Wang, Y. Lin, and X. Deng, “Magnetic biodegradable fe<sub>3</sub>o<sub>4</sub>/cs/pva nanofibrous membranes for bone regeneration,” *Biomedical Materials*, vol. 6, no. 5, p. 055008, 2011.
  - [55] F. Yang, J. Lu, Q. Ke, X. Peng, Y. Guo, and X. Xie, “Magnetic mesoporous calcium silicate/chitosan porous scaffolds for enhanced bone regeneration and photothermal-chemotherapy of osteosarcoma,” *Scientific reports*, vol. 8, no. 1, p. 7345, 2018.
  - [56] A. Portela, M. Vasconcelos, M. H. Fernandes, M. Garcia, A. Silva, J. Gabriel, F. Gartner, I. Amorim, and J. Cavalheiro, “Highly focalised thermotherapy using a ferrimagnetic cement in the treatment of a melanoma mouse model by low temperature hyperthermia,” *International Journal of Hyperthermia*, vol. 29, no. 2, pp. 121–132, 2013.
  - [57] T. Ota, Y. Nishida, K. Ikuta, R. Kato, E. Kozawa, S. Hamada, T. Sakai, and N. Ishiguro, “Heat-stimuli-enhanced osteogenesis using clinically available biomaterials,” *PloS one*, vol. 12, no. 7, p. e0181404, 2017.
  - [58] J.-h. Ke, Z.-k. Wang, Y.-z. Li, Q.-l. Hu, and J. Feng, “Ferroferric oxide/chitosan scaffolds with three-dimensional oriented structure,” *Chinese Journal of Polymer Science*, vol. 30, no. 3, pp. 436–442, 2012.
  - [59] M. Bañobre-López, Y. Pineiro-Redondo, R. De Santis, A. Gloria, L. Ambrosio, A. Tampieri, V. Dediú, and J. Rivas, “Poly (caprolactone) based magnetic scaffolds for bone tissue engineering,” *Journal of applied physics*, vol. 109, no. 7, p. 07B313, 2011.
  - [60] Q.-Y. Fan, B.-A. Ma, X.-C. Qiu, Y.-L. Li, J. Ye, and Y. Zhou, “Preliminary report on treatment of bone tumors with microwave-induced hyperthermia,” *Bioelectromagnetics*, vol. 17, no. 3, pp. 218–222, 1996.
  - [61] Y. Li, R. Han, C. Geng, Y. Wang, and L. Wei, “A new osteonecrosis animal model of the femoral head induced by microwave heating and repaired with tissue engineered bone,” *International orthopaedics*, vol. 33, no. 2, pp. 573–580, 2009.
  - [62] R. K. Singh, M. Srivastava, N. Prasad, S. Awasthi, A. Dhayalan, and S. Kannan, “Iron doped  $\beta$ -tricalcium phosphate: Synthesis, characterization, hyperthermia effect, biocompatibility and mechanical evaluation,” *Materials Science and Engineering: C*, vol. 78, pp. 715–726, 2017.
  - [63] M. Ikenaga, K. Ohura, T. Yamamuro, Y. Kotoura, M. Oka, and T. Kokubo, “Localized hyperthermic treatment of experimental bone tumors with ferromagnetic ceramics,” *Journal of orthopaedic research*, vol. 11, no. 6, pp. 849–855, 1993.

- [64] F. Pelaez, N. Manuchehrabadi, P. Roy, H. Natesan, Y. Wang, E. Racila, H. Fong, K. Zeng, A. M. Silbaugh, J. C. Bischof *et al.*, “Biomaterial scaffolds for non-invasive focal hyperthermia as a potential tool to ablate metastatic cancer cells,” *Biomaterials*, vol. 166, pp. 27–37, 2018.
- [65] P. R. Stauffer, T. C. Cetas, A. M. Fletcher, D. W. Deyoung, M. W. Dewhirst, J. R. Oleson, and R. B. Roemer, “Observations on the use of ferromagnetic implants for inducing hyperthermia,” *IEEE Transactions on biomedical engineering*, no. 1, pp. 76–90, 1984.
- [66] P. R. Stauffer, T. C. Cetas, and R. C. Jones, “Magnetic induction heating of ferromagnetic implants for inducing localized hyperthermia in deep-seated tumors,” *IEEE Transactions on Biomedical Engineering*, no. 2, pp. 235–251, 1984.
- [67] A. Uchida, H. Wakabayashi, N. Okuyama, A. Okamura, A. Matsumine, and K. Kusuzaki, “Metastatic bone disease: pathogenesis and new strategies for treatment,” *Journal of Orthopaedic Science*, vol. 9, no. 4, pp. 415–420, 2004.
- [68] F. Baino, E. Fiume, M. Miola, F. Leone, B. Onida, F. Laviano, R. Gerbaldo, and E. Verné, “Fe-doped sol-gel glasses and glass-ceramics for magnetic hyperthermia,” *Materials*, vol. 11, no. 1, p. 173, 2018.
- [69] E. Verné, M. Bruno, M. Miola, G. Maina, C. Bianco, A. Cochis, and L. Rimondini, “Composite bone cements loaded with a bioactive and ferrimagnetic glass-ceramic: Leaching, bioactivity and cytocompatibility,” *Materials Science and Engineering: C*, vol. 53, pp. 95–103, 2015.
- [70] A. Fanti, M. B. B. Lodi, G. Vacca, and G. Mazzarella, “Numerical investigation of bone tumor hyperthermia treatmetn using magnetic scaffolds,” *IEEE Journal of Electromagnetics, RF and Microwaves in Medicine and Biology*, 2018.
- [71] B. Dhandayuthapani, Y. Yoshida, T. Maekawa, and D. S. Kumar, “Polymeric scaffolds in tissue engineering application: a review,” *International journal of polymer science*, vol. 2011, 2011.
- [72] G. Ciardelli, V. Chiono, G. Vozzi, M. Pracella, A. Ahluwalia, N. Barbani, C. Cristallini, and P. Giusti, “Blends of poly-( $\varepsilon$ -caprolactone) and polysaccharides in tissue engineering applications,” *Biomacromolecules*, vol. 6, no. 4, pp. 1961–1976, 2005.
- [73] G. Zadora and Z. Brožek-Mucha, “Sem-edx—a useful tool for forensic examinations,” *Materials chemistry and physics*, vol. 81, no. 2-3, pp. 345–348, 2003.
- [74] C. A. Schneider, W. S. Rasband, and K. W. Eliceiri, “Nih image to imagej: 25 years of image analysis,” *Nature methods*, vol. 9, no. 7, p. 671, 2012.

- [75] S. Tumanski, *Handbook of magnetic measurements*. CRC press, 2016.
- [76] D. Collinson, *Methods in rock magnetism and palaeomagnetism: techniques and instrumentation*. Springer Science & Business Media, 2013.
- [77] R. Nopper, R. Niekravietz, and L. Reindl, “Wireless readout of passive lc sensors,” *IEEE Transactions on Instrumentation and Measurement*, vol. 59, no. 9, pp. 2450–2457, 2010.
- [78] E. Irving, “Methods in palaeomagnetism, editors: Dw collinson, km creer and sk runcorn,(elsevier, amsterdam, 1967),” 1967.
- [79] T. T. Lang, *Electronics of Measuring Systems: Practical Implementation of Analogue and Digital Techniques*, ser. Design And Measurement in Electronic Engineering, 1983.
- [80] A. De Vries and J. Livius, “A sensitive and rapid bridge for the study of magnetic susceptibilities at frequencies from 200 to 10 6 hz,” *Applied Scientific Research*, vol. 17, no. 1, pp. 31–64, 1967.
- [81] R. Girdler, “The measurement and computation of anisotropy of magnetic susceptibility of rocks,” *Geophysical Journal International*, vol. 5, no. 1, pp. 34–44, 1961.
- [82] K. Christie and D. Symons, *Apparatus for measuring magnetic susceptibility and its anisotropy*. Department of Energy, Mines and Resources, 1969.
- [83] M. Cooke and A. De Sa, “A radio frequency method for the measurement of initial magnetic susceptibility,” *Journal of Physics E: Scientific Instruments*, vol. 14, no. 10, p. 1192, 1981.
- [84] K. Park, S. Sonkusale, R. P. Guertin, T. Harrah, and E. B. Goldberg, “A miniaturized ac magnetic susceptometer for detecting biomolecules tagged to magnetic nanoparticles,” in *Bioengineering Conference, 2009 IEEE 35th Annual Northeast*. IEEE, 2009, pp. 1–2.
- [85] N. K. Das, T. Jayakumar, and B. Raj, “Noniterative digital ac bridge balance,” *IEEE Transactions on Instrumentation and Measurement*, vol. 59, no. 11, pp. 3058–3060, 2010.
- [86] N. K. Das, S. Dey, S. Pal, and P. Barat, “Innovative instrumentation to measure magnetic susceptibility,” *IEEE Transactions on Magnetics*, vol. 49, no. 9, pp. 4965–4969, 2013.
- [87] V. Labinac, N. Erceg, and D. Kotnik-Karuza, “Magnetic field of a cylindrical coil,” *American journal of physics*, vol. 74, no. 7, pp. 621–627, 2006.
- [88] F. W. Grover, *Inductance calculations: working formulas and tables*. Courier

- Corporation, 2004.
- [89] A. Massarini, M. Kazimierczuk, and G. Grandi, "Lumped parameter models for single-and multiple-layer inductors," in *Power Electronics Specialists Conference, 1996. PESC'96 Record., 27th Annual IEEE*, vol. 1. IEEE, 1996, pp. 295–301.
  - [90] A. Massarini and M. K. Kazimierczuk, "Self-capacitance of inductors," *IEEE Transactions on power electronics*, vol. 12, no. 4, pp. 671–676, 1997.
  - [91] G. Grandi, M. K. Kazimierczuk, A. Massarini, and U. Reggiani, "Stray capacitances of single-layer solenoid air-core inductors," *IEEE Transactions on Industry Applications*, vol. 35, no. 5, pp. 1162–1168, 1999.
  - [92] C. M. de Miranda and S. F. Pichorim, "Self-resonant frequencies of air-core single-layer solenoid coils calculated by a simple method," *Electrical Engineering*, vol. 97, no. 1, pp. 57–64, 2015.
  - [93] A. Reatti and M. K. Kazimierczuk, "Comparison of various methods for calculating the ac resistance of inductors," *IEEE Transactions on Magnetics*, vol. 38, no. 3, pp. 1512–1518, 2002.
  - [94] M. R. Spiegel and J. Liu, *Schaum's mathematical handbook of formulas and tables*. McGraw-Hill New York, 1999, vol. 1000.
  - [95] G. Grandi, U. Reggiani, M. Kazimierczuk, and A. Massarini, "Optimal design of single-layer solenoid air-core inductors for high frequency applications," in *Circuits and Systems, 1997. Proceedings of the 40th Midwest Symposium on*, vol. 1. IEEE, 1997, pp. 358–361.
  - [96] C. C. Sanchez, M. F. Pantoja, and R. G. Martin, "Design of gradient coil for magnetic resonance imaging applying particle-swarm optimization," *IEEE Transactions on Magnetics*, vol. 47, no. 12, pp. 4761–4768, 2011.
  - [97] R. Turner, "A target field approach to optimal coil design," *Journal of physics D: Applied physics*, vol. 19, no. 8, p. L147, 1986.
  - [98] D. E. Goldberg, *Genetic algorithms*, 2006.
  - [99] S. Ho, G. Xu, W. Fu, Q. Yang, H. Hou, and W. Yan, "Optimization of array magnetic coil design for functional magnetic stimulation based on improved genetic algorithm," *IEEE transactions on magnetics*, vol. 45, no. 10, pp. 4849–4852, 2009.
  - [100] J. H. Holland, "Genetic algorithms," *Scientific american*, vol. 267, no. 1, pp. 66–73, 1992.
  - [101] D. Meeker, "Finite element method magnetics," *FEMM*, vol. 4, p. 32, 2010.
  - [102] S. Trisnanto and Y. Kitamoto, "Field-dependent brownian relaxation dynamics of a superparamagnetic clustered-particle suspension," *Physical Review E*, vol. 90, no. 3,

- p. 032306, 2014.
- [103] A. S. Sedra and K. C. Smith, *Microelectronic circuits*. Holt, Rinehart and Winston, 1982.
  - [104] StemLabs. (2018) RedPitaya STEMLAB user's manual. [Online]. Available: <https://redpitaya.readthedocs.io/en/latest/>
  - [105] N. Tomita, H. Jeong, J. Choi, H. Ishitsuka, S. Mima, T. Nagasaki, S. Oguri, and O. Tajima, "World's cheapest readout electronics for kinetic inductance detector by using redpitaya," *Journal of Low Temperature Physics*, vol. 184, no. 1-2, pp. 443–448, 2016.
  - [106] P. Lemal, C. Geers, B. Rothen-Rutishauser, M. Lattuada, and A. Petri-Fink, "Measuring the heating power of magnetic nanoparticles: an overview of currently used methods," *Materials Today: Proceedings*, vol. 4, pp. S107–S117, 2017.
  - [107] P. Lemal, C. Geers, C. A. Monnier, F. Crippa, L. Daum, D. A. Urban, B. Rothen-Rutishauser, M. Bonmarin, A. Petri-Fink, and T. L. Moore, "Lock-in thermography as a rapid and reproducible thermal characterization method for magnetic nanoparticles," *Journal of Magnetism and Magnetic Materials*, vol. 427, pp. 206–211, 2017a.
  - [108] B. Lahiri, S. Ranoo, and J. Philip, "Infrared thermography based magnetic hyperthermia study in fe<sub>3</sub>o<sub>4</sub> based magnetic fluids," *Infrared Physics & Technology*, vol. 78, pp. 173–184, 2016.
  - [109] A. Cervadoro, C. Giverso, R. Pande, S. Sarangi, L. Preziosi, J. Wosik, A. Brazdeikis, and P. Decuzzi, "Design maps for the hyperthermic treatment of tumors with superparamagnetic nanoparticles," *PLoS One*, vol. 8, no. 2, p. e57332, 2013.
  - [110] S. A. T. D. Peabody, *Orthopaedic Oncology*. Springer International Publishing, 2016.
  - [111] C. Fletcher, "Pathology and genetics of tumors of soft tissue and bone," *World Health Organization Classification of Tumors*, vol. 4, pp. 35–46, 2002.
  - [112] F. Schajowicz, *Histological typing of bone tumours*. Springer Science & Business Media, 2012.
  - [113] A. L. Folpe, "Fibrosarcoma: a review and update," *Histopathology*, vol. 64, no. 1, pp. 12–25, 2014.
  - [114] J. S. Biermann, W. Chow, D. R. Reed, D. Lucas, D. R. Adkins, M. Agulnik, R. S. Benjamin, B. Brigman, G. T. Budd, W. T. Curry *et al.*, "Nccn guidelines insights: bone cancer, version 2.2017," *Journal of the National Comprehensive Cancer Network*, vol. 15, no. 2, pp. 155–167, 2017.
  - [115] E. Skafida, S. Kokkali, M. Nikolaou, and A. Digklia, "Metastatic soft tissue sarcoma:

- current treatment landscape and future perspectives,” *Expert review of anticancer therapy*, vol. 17, no. 6, pp. 537–543, 2017.
- [116] N. Datta, S. G. Ordóñez, U. Gaipl, M. Paulides, H. Crezee, J. Gellermann, D. Marder, E. Puric, and S. Bodis, “Local hyperthermia combined with radiotherapy and-/or chemotherapy: Recent advances and promises for the future,” *Cancer treatment reviews*, vol. 41, no. 9, pp. 742–753, 2015.
- [117] M. Linch, A. B. Miah, K. Thway, I. R. Judson, and C. Benson, “Systemic treatment of soft-tissue sarcoma—gold standard and novel therapies,” *Nature reviews Clinical oncology*, vol. 11, no. 4, p. 187, 2014.
- [118] M. Parhizkar, S. Mahalingam, S. Homer-Vanniasinkam, and M. Edirisinghe, “Latest developments in innovative manufacturing to combine nanotechnology with health-care,” *Nanomedicine*, vol. 13.
- [119] E. FarrokhTakin, G. Ciofani, G. L. Puleo, G. de Vito, C. Filippeschi, B. Mazzolai, V. Piazza, and V. Mattoli, “Barium titanate core–gold shell nanoparticles for hyperthermia treatments,” *International journal of nanomedicine*, vol. 8, p. 2319, 2013.
- [120] A. Bailon-Plaza and M. C. Van Der Meulen, “A mathematical framework to study the effects of growth factor influences on fracture healing,” *Journal of Theoretical Biology*, vol. 212, no. 2, pp. 191–209, 2001.
- [121] P. Moreo, J. M. García-Aznar, and M. Doblaré, “Bone ingrowth on the surface of endosseous implants. part 1: Mathematical model,” *Journal of theoretical biology*, vol. 260, no. 1, pp. 1–12, 2009.
- [122] A. Fanti, M. Spanu, M. B. Lodi, F. Desogus, and G. Mazzarella, “Nonlinear analysis of soil microwave heating: Application to agricultural soils disinfection,” *IEEE Journal on Multiscale and Multiphysics Computational Techniques*, vol. 2, pp. 105–114, 2017.
- [123] D. H. Werner and Z. H. Jiang, *Electromagnetics of body area networks: antennas, propagation, and RF systems*. John Wiley & Sons, 2016.
- [124] A. Y. Matloubieh, R. B. Roemer, and T. C. Cetas, “Numerical simulation of magnetic induction heating of tumors with ferromagnetic seed implants,” *IEEE transactions on biomedical engineering*, no. 2, pp. 227–234, 1984.
- [125] W. Snyder *et al.*, “Report of the task group on reference man,” Pergamon Press; Oxford, Tech. Rep., 1974.
- [126] R. Hergt, S. Dutz, and M. Zeisberger, “Validity limits of the néel relaxation model of magnetic nanoparticles for hyperthermia,” *Nanotechnology*, vol. 21, no. 1, p. 015706, 2009.

- [127] J. Dormann, F. D’Orazio, F. Lucari, E. Tronc, P. Prené, J. Jolivet, D. Fiorani, R. Cherkaoui, and M. Nogues, “Thermal variation of the relaxation time of the magnetic moment of  $\gamma$ -fe 2 o 3 nanoparticles with interparticle interactions of various strengths,” *Physical Review B*, vol. 53, no. 21, p. 14291, 1996.
- [128] M. Mital and H. V. Tafreshi, “A methodology for determining optimal thermal damage in magnetic nanoparticle hyperthermia cancer treatment,” *International journal for numerical methods in biomedical engineering*, vol. 28, no. 2, pp. 205–213, 2012.
- [129] H. Arkin, L. Xu, and K. Holmes, “Recent developments in modeling heat transfer in blood perfused tissues,” *IEEE Transactions on Biomedical Engineering*, vol. 41, no. 2, pp. 97–107, 1994.
- [130] A.-R. Khaled and K. Vafai, “The role of porous media in modeling flow and heat transfer in biological tissues,” *International Journal of Heat and Mass Transfer*, vol. 46, no. 26, pp. 4989–5003, 2003.
- [131] R. Sabater i Serra, J. L. Escobar Ivirico, J. M. Meseguer Dueñas, A. A. Balado, J. L. Gómez Ribelles, and M. Salmerón Sánchez, “Segmental dynamics in poly ( $\varepsilon$ -caprolactone)/poly (l-lactide) copolymer networks,” *Journal of Polymer Science Part B: Polymer Physics*, vol. 47, no. 2, pp. 183–193, 2009.
- [132] B. Kuttich, C. Lederle, and B. Stühn, “Water dependence of the dielectric relaxation in polycaprolactone,” *The Journal of chemical physics*, vol. 139, no. 24, p. 244907, 2013.
- [133] S. Symeonidis, W. G. Whittow, M. Zecca, and C. Panagamuwa, “Bone fracture monitoring using implanted antennas in the radius, tibia and phalange heterogeneous bone phantoms,” *Biomedical Physics & Engineering Express*, vol. 4, no. 4, p. 045006, 2018.
- [134] A. Swarup, S. Stuchly, and A. Surowiec, “Dielectric properties of mouse mca1 fibrosarcoma at different stages of development,” *Bioelectromagnetics*, vol. 12, no. 1, pp. 1–8, 1991.
- [135] C. B. E. N. M. G. D. P. A. K. N. K. P.A. Hasgall, F. Di Gennaro, version 3.0, 2015. [www.itis.ethz.ch/database](http://www.itis.ethz.ch/database).
- [136] F. A. Duck, *Physical properties of tissues: a comprehensive reference book*. Academic press, 2013.
- [137] C. W. Song, “Effect of local hyperthermia on blood flow and microenvironment: a review,” *Cancer research*, vol. 44, no. 10 Supplement, pp. 4721s–4730s, 1984.
- [138] R. K. Jain and K. Ward-Hartley, “Tumor blood flow-characterization, modifications,

- and role in hyperthermia,” *IEEE Transactions on sonics and ultrasonics*, vol. 31, no. 5, pp. 504–525, 1984.
- [139] W. Zhao, J.-Z. Chen, J.-H. Hu, J.-Q. Huang, Y.-N. Jiang, G. Luo, G.-F. Yi, Z.-H. Peng, H. Wang, J. Shen *et al.*, “In vivo effects of radiofrequency ablation on long bones and the repair process in swine models,” *Japanese journal of radiology*, vol. 35, no. 1, pp. 31–39, 2017.
- [140] L. Liang, *Ab-initio calculation of bulk and surface models of A-and B-tricalcium phosphate*. University of Missouri-Kansas City, 2009.
- [141] Z. Ma, Z. Mao, and C. Gao, “Surface modification and property analysis of biomedical polymers used for tissue engineering,” *Colloids and Surfaces B: Biointerfaces*, vol. 60, no. 2, pp. 137–157, 2007.